Doctoral Dissertation

Relating The Origins Of Disk Bar Structure To Star Formation And Stellar Dynamics In Simulations Of Resolved Galaxies

（円盤銀河のバー構造の起源とその銀河内の星形成と星の動径移動に与える影響について）

Elizabeth Jayne Latrobe ILES

Graduate School of Science, Hokkaido University
Department of Cosmosciences

March 2023

Relating the origins of disk bar structure to star formation and stellar dynamics in simulations of resolved galaxies

Elizabeth J.L. Iles
(id. 20205013)

Graduate School of Science
Department of Cosmosciences
Theoretical Astrophysics Group

February 21, 2023

Submitted in fulfillment of the requirements for the Doctor of Philosophy (PhD) in Theoretical Astrophysics at the University of Hokkaido, Japan

Academic Supervisors: *Takashi Okamoto & Alex R. Pettitt*

Statements and Declaration

This thesis contains no material which has been accepted for a degree or diploma by the University or any other institution, except by way of background information and duly acknowledged in the thesis, and to the best of my knowledge and belief no material previously published or written by another person except where due acknowledgement is made in the text of the thesis, nor does the thesis contain any material that infringes copyright.

The publishers of the papers comprising any part of this thesis hold the copyright for that content and access to the material should be sought from the respective journals. The remaining non published content of the thesis may be made available for loan and limited copying and communication in accordance with the appropriate copyright legislation.

The author is the recipient of a Japanese Government MEXT scholarship. The computing resources of CfCA at NAOJ (XC50) were employed as part of this research. The code packages of Gasoline *and* Galic *are also used with appropriate acknowledgement of the developers.*

Abstract

Simulation results initialised from observations of nearby NGC4303 and NGC3627 are used to investigate trends in the star formation and stellar dynamics in the early periods ($\leq 1\,\mathrm{Gyr}$) of bar formation and evolution. Three simulated disk galaxies which evolve into late-type barred-spirals are presented, each representative of either isolated bar evolution, motivated by disk instability (IsoB, TideNC) or, a tidally affected, interaction-driven development (TideB). These disks are then used to assess whether such different mechanisms capable of driving the formation of galactic bars, will also differently affect the impact of the bar on the stellar populations and star-forming ISM in the host-galaxy. It is apparent that the presence of a bar significantly impacts the stellar properties in these barred disks. It is also apparent that galaxies with visibly similar bars formed in differing isolated and tidally-driven conditions can evolve with clearly distinguishable differences, particularly in the spatially dependent star forming history. By constraining attributes within the measurable stellar properties of disk galaxies in this manner, it may be possible to identify characteristics which act as tracers for the specific origins of bar formation and thus, allow us to determine the evolutionary histories of resolved galaxies.

Contents

1 Introduction **1**

2 Theoretical & Computational Background **4**
2.1 Scientific Rationale 4
2.1.1 Galactic Evolution & Barred Galaxies 4
2.1.2 Star Formation 6
2.1.3 Radial Migration & Galactic Dynamics 8
2.2 Resolved Target Galaxies 10
2.2.1 NGC4303 - Isolated Target 11
2.2.2 NGC3627 - Tidally-driven Target 12
2.3 Numerical Simulation Method 13
2.3.1 Simulated Disk Specifications 13
2.3.2 Simulation Parameters 16

3 Classification of Simulated Disk Features **18**
3.1 General Observable Features 18
3.1.1 Gas & Star Particle Distributions 18
3.1.2 Comparison to Target Galaxies 20
3.2 Dynamical Features 22

4 Star Formation in Isolated and Tidally-Driven Bars **26**
4.1 Star Forming History 26
4.2 Star Forming Features 30
4.2.1 Star Formation Rates in the Disk 31
4.2.2 The Kennicutt-Schmidt Relation 33
4.2.3 Comparing Region-Averaged Values 39
4.3 Radial Dependence of SFE 41
4.4 Dependence of SFE within the Bar 44

5 Stellar Motion in Isolated and Tidally-Driven Bars **51**
5.1 Total Variation over the Simulation 51
5.2 Changes Relative to Radial Position 57

5.2.1 Standard Parameters 57
5.2.2 Orbital Parameters 62
5.3 Age & Metallicity Dependence 64
5.3.1 Revisiting Total Change Histograms 65
5.3.2 Evolution of Metallicity 67
5.3.3 Observations of Trends at 1 Gyr 69

6 Conclusions **74**

List of Figures

2.1 Initial condition rotation curves (Iles et al., 2022). 15

3.1 Face-on gas and stellar density distributions for IsoB, TideB and TideNC. 19
3.2 Side-on stellar density distribution for IsoB, TideB & TideNC. 20
3.3 Synthetic observations of IsoB & TideB comparable to NGC 4303 & NGC 3627. 21
3.4 Stellar surface density along major- & minor-axis of the bar in IsoB & TideB (Iles et al., 2022). 22
3.5 Rotation curves for IsoB & TideB at approx. bar formation (Iles et al., 2022). 23
3.6 Radial & tangential velocity in the disk-plane of IsoB & TideB (Iles et al., 2022). 24

4.1 Star formation history of IsoB & TideB until 200 Myr post-bar formation (Iles et al., 2022). 27
4.2 Star formation by morphological region (Bar, Arm & Inter-arm) of IsoB & TideB until 200 Myr post-bar formation (Iles et al., 2022). 29
4.3 $\Sigma_{\rm SFR}$ projected into the disk-plane of IsoB & TideB (Iles et al., 2022). 31
4.4 Kennicutt-Schmidt relation for IsoB & TideB compared to literature relations (Iles et al., 2022). 33
4.5 Kennicutt-Schmidt relation for morphological regions (Bar, Arm & Inter-arm) of IsoB & TideB (Iles et al., 2022). 36
4.6 Azimuthally averaged SFE within bins of 1 kpc radius for IsoB & TideB (Iles et al., 2022). 41
4.7 Time evolution of the SFE(r) gradient from a linear fit to Figure 4.6 (Iles et al., 2022). 43
4.8 Azimuthally averaged SFE within bins along the bar-axis for IsoB & TideB (Iles et al., 2022). 45
4.9 Heat map of SFE along the bar-axis tracing time-dependent features in IsoB & TideB (Iles et al., 2022). 47

4.10 Central region zoom-in of face-on gas density for TideB 100 Myr post-bar formation (Iles et al., 2022). 49

5.1 Initial vs. final values of Δr, ΔL_z & Δz for stars formed in IsoB, TideB & TideNC. 52
5.2 Histogram of total change over 1 Gyr in Δr, ΔL_z & Δz for stars formed in IsoB, TideB & TideNC. 54
5.3 Face-on projection of changes in Δr, ΔL_z & Δz for stars formed in IsoB, TideB & TideNC. 56
5.4 Time evolution of dependence for change Δr on radial position (r_i) for stars formed in IsoB, TideB & TideNC. 58
5.5 Time evolution of dependence for change ΔL_z on radial position (r_i) for stars formed in IsoB, TideB & TideNC. 60
5.6 Time evolution of dependence for change Δz on radial position (r_i) for stars formed in IsoB, TideB & TideNC. 61
5.7 Time evolution of dependence for change Δecc on radial position (r_i) for stars formed in IsoB, TideB & TideNC. 63
5.8 Time evolution of dependence for change Δr_{typ} on radial position (r_i) for stars formed in IsoB, TideB & TideNC. 64
5.9 Histogram of total change over 1 Gyr in Δr with stellar population separated by formation time and radius in IsoB, TideB & TideNC. 65
5.10 Face-on projection of stellar metallicity (Z_{metal}) distributions for IsoB, TideB & TideNC. 67
5.11 Time evolution of dependence for change Δr on radial position (r_i) for stars formed in IsoB, TideB & TideNC, weighted by median stellar metallicity (Z_{metal}). 69
5.12 [O/Fe] vs. [Fe/H] at 1 Gyr, weighted by formation time and radius in IsoB, TideB & TideNC. 70
5.13 Dependence of metallicity [O/Fe] with current radial position (r) based on formation radius r_{form} in IsoB, TideB & TideNC. . 72

List of Tables

2.1 Initial condition mass & distance parameters for IsoB, TideB & TideNC. 13

4.1 Gradient coefficient (α) for power law fit to $\Sigma_{\rm gas}$ vs. $\Sigma_{\rm SFR}$ in IsoB & TideB (Iles et al., 2022). 37

4.2 Mean $\Sigma_{\rm gas}$ & $\Sigma_{\rm SFR}$ values for morphological regions (Bar, Arm & Inter-arm) of IsoB & TideB (Iles et al., 2022). 39

Chapter 1

Introduction

The effects of galactic structure formation and the mechanisms which may provoke galaxies to evolve into the specific and varied morphologies observable throughout the universe remains one of the pressing questions in astronomy today. In particular, this work will focus on the presence and effects of the central bar feature which can be observed in many–although not all–spiral disk-type galaxies, including the Milky Way. It has been shown that a range of formation mechanisms can produce such a bar-like feature in the central region of galaxies and consequently, affect the properties of both the host-galaxy and the bar structure itself (Hohl, 1971; Noguchi, 1987; Raha et al., 1991; Sheth et al., 2002; Sellwood, 2014; Martinez-Valpuesta et al., 2017; Zana et al., 2019). However, a comprehensive understanding of how galactic bar formation directly impacts the interstellar medium (ISM) and correspondingly, star formation and stellar dynamics in a given galaxy, is still elusive. Additionally, while many previous studies endeavour to show that the presence of a bar will significantly impact the general stellar properties in disk galaxies, this is often considered independently of the mechanisms capable of producing such features. This research aims to investigate whether the different formation mechanisms capable of producing a central galactic bar also subsequently affect the impact of the bar on the host-galaxy's stellar populations and star forming ISM in significant and discernibly different ways. These features could then become potential signatures for identifying the origins of any observable barred-system, even post-interaction, while simultaneously developing the wider understanding of galactic bars and their ongoing role in galactic evolution.

In recent years, increasingly detailed, high resolution, large-scale observational surveys have continued to raise the ability of astronomers to measure and assess star formation rates and efficiencies, as well as document the wide range of observed morphological and dynamical features in galaxies—i.e. the COMING–CO multi-line imaging of nearby galaxies (Sorai et al., 2019) and the PHANGS–Physics at High Angular resolution in Nearby GalaxieS (Lee

et al., 2022) surveys referenced herein. However, due to the relative time-scales of galactic evolution, it is simply impossible for an observational survey to capture the long-term evolution of galaxies, regardless of the breadth and depth of modern observational capabilities. Here, high resolution numerical simulations, with the ability to track changes over long time-scales and at varying length-scales, becomes indispensable. The formative work of Toomre & Toomre (1972) and their contemporaries proved N-body simulations to be an indisputably powerful tool for determining the mechanics and kinematics driving the formation of structure in observed galaxies. With the intervening years of scientific and technological advancement, this tool has only become more potent in capability–it is now directly possible to produce simulations replicating the evolution of a galaxy at a resolution comparable to a true number of stars under self-gravitation (Fujii et al., 2018). The mechanisms which may affect bar and arm features, including but not limited to internal properties of individual galaxies, such as mass-fractions and internal forces (Hohl, 1971; Ostriker & Peebles, 1973; Friedli & Martinet, 1993; Baba, 2015; Wu & Jiang, 2015; Sellwood & Gerhard, 2020), and all manner of interactions constraining size-ratios, orbits and internal structures (Noguchi, 1987; Elmegreen et al., 1991; Fiacconi et al., 2012; Dobbs, 2013; Oh et al., 2015; Pettitt & Wadsley, 2018) have been studied extensively in this manner.

In this work, we employ numerical hydrodynamics in the form of Smoothed Particle Hydrodynamics (SPH) simulations for a small sample of barred-disk galaxies which are representative of two possible bar formation mechanisms and are initialised from measurements of observationally resolved galaxies. Resolved galaxies are considered prime targets for studying the effects of galactic bar morphology on the star forming ISM. The specific targets are selected based on the criteria of a well-known barred-spiral morphology and different environmental conditions: NGC 4303 (M61) is selected, noting it has been determined to be an isolated disk galaxy on the outskirts of the Virgo cluster with no HI gas depletion (Yajima et al., 2019); while NGC 3627 provides a counterpart with obvious traces of past interaction determined from an asymmetrical and distorted HI gas component (Haynes et al., 1979). With the former effectively isolated and the latter considered part of an interacting system, these targets facilitate a comparison between a bar formed in isolation originating from random perturbation and a bar triggered by the tidal forces of interaction with a passing companion.

In the following analysis, the stellar properties, star formation and dynamics are each assessed and compared in the early epoch (≤ 1 Gyr) of the simulated disk evolution, where any interaction effects should be most clearly distinguishable. The primary targets for comparison are IsoB, a barred galaxy with an isolated evolutionary history tailored to measurements of NGC 4303,

and the similarly barred TideB, which is externally driven by the tidal forces of a companion in a minor merger-like interaction tailored to NGC 3627. A third disk is also introduced which serves as a comparison (TideNC) where the tidal case TideB is evolved without the influence of the companion. The development and evolution of the first two cases (IsoB and TideB) has been presented in depth by Iles et al. (2022), accompanying a discussion of the star formation features and how these differ between two similar barred disks with differing bar formation mechanisms (see also Chapter 4). These simulations are performed using the GASOLINE2 code (Wadsley et al., 2017) and have a live component to represent the stars, gas, and dark matter with initial conditions generated from the GALIC package (Yurin & Springel, 2014) and the results of previous studies (e.g Pettitt & Wadsley, 2018).

The primary aim is to consider the spatially and temporally varying trends of bar-related star formation, coupled with the kinematic and dynamical behaviour for these newly-formed stellar populations as can be traced within the developing disk structures. This has been completed with a view to identifying any significant trends in the stellar populations of these galaxies, as well as to differentiate between effects arising from the differently triggered bar structure throughout the evolution of these features. However, any evolutionary trends which may be persistent and distinguishable in simulations – wherein the entire lifetimes of galaxies can be observed – are not so simple to determine from the single snapshot observations of real galaxies. It is, therefore, also necessary to consider whether there exists any means of extracting these features from the observations of real galaxies, although this remains a work in progress.

A general outline for the complete presentation of this work is as follows. A brief summary of the necessary theoretical background and computational parameters for constructing the simulated disks is included in Chapter 2, with the general results for the total 1 Gyr of simulation time in each disk presented in Chapter 3. The primary comparison between star forming features in the isolated and tidally-triggered disks IsoB and TideB (Iles et al., 2022) can be found in Chapter 4. Comparatively, the focus of Chapter 5 is on the subsequent stellar motions of these simulation-formed stars in the periods post-formation. Finally, in Chapter 6, the conclusions and avenues for future work are briefly summarised.

Chapter 2

Theoretical & Computational Background

2.1 Scientific Rationale

Naturally, this work is dependent on a foundation built from many decades of previous scientific research. The following review constitutes only a very brief introduction to the relevant literature as serves to contextualise the significance of this study within the domain of astronomy as a larger, inter-connected body of knowledge.

2.1.1 Galactic Evolution & Barred Galaxies

The formation and evolution of galaxies has long been an area of interest to the astronomical community. The variations in galactic components and morphological structures possible to observe in the nearby universe, as well as throughout cosmic time, only continue to promote inquiry in this area. However, due to the long time-scales required for a galaxy to form and evolve relative to our observational capabilities, a true and complete determination of such processes is, in practice, fundamentally unattainable. Thus, we are driven to develop theories and test hypotheses against the array of observationally available data. From the morphological evolutionary sequence pioneered by Hubble (Hubble, 1936) to the nuanced possibilities for a complex web of galactic evolutionary pathways generally accepted today, we remain concerned with how best to determine an evolutionary history for the universally observable galaxy distribution.

Here, we focus specifically on a sub-class of spiral-type galaxy, which can be seen to exhibit a straight bar-like feature in the central region of the disk. These barred-spiral galaxies have been shown to make up a large portion of all observed spiral galaxies, although the exact fraction ($\sim$ 25–75%) depends

heavily on bar classification criteria (Schinnerer et al., 2002; Aguerri et al., 2009; Masters et al., 2011). It is also expected that the Milky Way is host to one such feature, which makes understanding the impact, as well as the origins, of these barred-galaxies seem particularly significant.

According to a long history of previous studies, it is possible for these bar-like features to form in kinematically cold, sufficiently massive, isolated stellar discs (Hohl, 1971; Ostriker & Peebles, 1973). Under this regime, an initial instability drives a fast growth phase where the bar emerges and subsequently buckles out of the disc-plane, before slowing down and growing gradually in a phase of secular evolution (Raha et al., 1991; Sellwood, 2014). However, in the $\Lambda_{\rm CDM}$ cosmology, it is perhaps unavoidable to consider the influence that galaxy-galaxy interaction must have to drive galactic morphology within the hierarchical system of structure formation (Miwa & Noguchi, 1998; Romano-Díaz et al., 2008; Lang et al., 2014; Pettitt & Wadsley, 2018). Historically, it has been shown that both major and minor interaction events can independently induce bar formation in isolated, bar-free galaxies or even slow the formation of a bar in an isolated disk galaxy that was already likely to form a bar; although, this was likely to have negligible effect on the properties of the bar itself (Noguchi, 1987; Salo, 1991). Conversely, subsequent studies have proved that some interaction conditions can instead dampen or completely halt bar formation, rather than induce it (Athanassoula, 2002; Kyziropoulos et al., 2016; Gajda et al., 2017; Moetazedian et al., 2017; Zana et al., 2019). Others assert that bars which are driven to form in interacting systems rather than in isolated disk environments, appear to rotate slower than those formed in isolation (Miwa & Noguchi, 1998; Martinez-Valpuesta et al., 2017; Łokas, 2018). It is also argued that the presence of a bar must have at least some environmental dependence, which would subsequently imply a possible co-dependence for bar formation on interactions (Méndez-Abreu et al., 2012; Skibba et al., 2012; Pettitt & Wadsley, 2018).

While the debate on the most probable origin conditions for these bar features continues, similar efforts are also directed at determining the effects of such features on the properties of the host-galaxies (e.g. Sheth et al., 2002; Fujii et al., 2018; Zana et al., 2019), often irrespective of whichever factors will influence the formation mechanism. For example, star formation rates between the bar and arm features in a given galaxy are consistently observed to differ considerably, often showing significantly lower star forming efficiency within the bar compared to other areas of the disk (Downes et al., 1996; Sheth et al., 2002; Watanabe et al., 2019). This variation is often attributed to the non-circular motions of stars and gas in the bar, usually induced by a non-axisymmetric bar potential that generates strong shock or shear motions along the bar and disrupts the bar-located molecular clouds, thus suppressing star

formation in that region (Roberts et al., 1979; Athanassoula, 1992; Schinnerer et al., 2002; Dobbs et al., 2014; Beuther et al., 2018). A consequence of which is that barred-galaxies become particularly useful to probe the relationship between star formation on small molecular cloud scales (10–100 pc) and galactic dynamics or gas kinematics at ∼kpc scales in both observational and theoretical studies of star formation in galaxies (Kuno et al., 2000; Warren et al., 2010; Watanabe et al., 2011; Hirota et al., 2014).

2.1.2 Star Formation

Spatial variation in the stellar population is a consistently observed and widely accepted attribute of most known galaxies. Past studies have, for example, shown that instances of radially decreasing sSFR in the central regions of galaxies and inverted colour profiles in galactic bulges are common, if not ubiquitous (Balcells & Peletier, 1994; de Jong, 1996; Peletier & de Grijs, 1998; Thomas & Davies, 2006; Munoz-Mateos et al., 2007; González Delgado et al., 2014, 2016; Morelli et al., 2016; Catalán-Torrecilla et al., 2017; Belfiore et al., 2018; Breda et al., 2020). Large-scale integral-field spectroscopic surveys with high-quality spectral data at multiple locations also show clear negative age gradients across most galaxies with older stellar populations in central regions and younger outskirts (Mehlert et al., 2003; Sánchez-Blázquez et al., 2014; González Delgado et al., 2015; Goddard et al., 2016; Ibarra-Medel et al., 2016; Sacchi et al., 2019; Peterken et al., 2020). From these observations, on the large-scale at least, it is generally predicted that the stellar disks of most galaxies are formed via the so-called process of inside-out growth, wherein dense galaxy centres are formed initially as stellar mass continues to build on the periphery causing galaxies to grow in radius while growing in mass (Eggen et al., 1962; Fall & Efstathiou, 1980; van den Bosch, 1998; Kepner, 1999; Trujillo et al., 2007; van der Wel et al., 2008; van Dokkum et al., 2008, 2013; Patel et al., 2013; Papovich et al., 2015; Whitney et al., 2019; Breda et al., 2020). An additional upside-down process, wherein disk thickening also occurs due to gas rich mergers in early epochs, is also considered to account for the bi-modality of many systems with thick (older stars) and thin (younger stars) disk populations (Brook et al., 2004; Bird et al., 2013; Agertz et al., 2021).

The advent of detailed numerical studies of galactic discs has made significant advancements to the global understanding star formation trends in galaxies (Di Matteo et al., 2007; Springel, 2010; Federrath & Klessen, 2012; Hopkins et al., 2013; Okamoto et al., 2015). For example, numerical methods have been, perhaps an indispensable, support towards resolving the impact that morphological features, such as the bar or spiral-arms, may have on star formation

processes at a range of scales from molecular clouds to region averaged star formation rates and efficiencies (Bournaud et al., 2010; Renaud et al., 2013; Cole et al., 2014; Fujimoto et al., 2016; Baba & Kawata, 2020). Through various simulation studies, it has been possible to determine how shear in different disk environments is able to affect cloud formation conditions and cloud-cloud collisions, producing differing likelihoods for the formation of massive stars or star formation efficiency in different morphological features, such as the bar-ends or feathered and spurred offsets to the arms (Dobbs et al., 2006; Emsellem et al., 2014; Renaud et al., 2015; Takahira et al., 2018). Additionally, high resolution galaxy simulations have provided a range of opportunities to challenge the limits of the so-called Kennicutt-Schmidt relation (Schmidt, 1959; Kennicutt et al., 1987) in terms of its coherence for measurements with very high spatial resolutions, as well as within morphologically distinct features such as bars and arms (Fujimoto et al., 2014). Previous studies of star formation in disk galaxies have probed in some depth the differing affects inherent to various observed morphological features, such as galactic bars, on the star forming tendencies of the host-galaxies (Bournaud et al., 2010; Fujimoto et al., 2014; Renaud et al., 2015; Baba & Kawata, 2020). Alternatively, others employ numerical simulations to great effect to instead probe the influences of many possible drivers external to the disk which may govern the formation of such features (Tan, 2000; Di Matteo et al., 2007; Inoue & Fukui, 2013; Pettitt & Wadsley, 2018). Few have attempted to consider categorically whether the different origins of these morphological features may also subsequently impact the effects of such features on the star-forming ISM.

While the presence of a bar has been shown to affect the star forming properties within a given galaxy disk, it is also well known that interactions between galaxies are able to strongly affect the gas dynamics and gas fractions and thus, alter the star forming potential of each involved galaxy. One such interaction driven effect is to observe particularly accelerated star formation triggered by the inflowing gas provided through the interaction forces – inciting starbursts (Mihos & Hernquist, 1994; Barnes & Hernquist, 1996; Hopkins et al., 2008). These driven starburst events are most commonly observed in the central regions of the interacting galaxies; however, there is evidence to suggest that this effect may not only be limited to the central region but also extend well into the disk of the galaxy, or occur uniquely in the disk in some cases (Di Matteo et al., 2007; Bournaud, 2011; Pettitt et al., 2017). Even minor interactions, classed as minor mergers, also appear to significantly impact the star formation statistics of galaxies, particularly at low redshift (Darg et al., 2010; Kaviraj, 2014; Taylor et al., 2017). These increases in star formation in various locations throughout the galactic disks prompted by the tidal forces of an interaction may not necessarily be distinguishable from the similar star

formation attributes which appear to be influenced by the presence of a galactic bar in a comparatively isolated and unperturbed galaxy. Hence, tracers of the mechanisms which drive and impact bar formation, such as tidally-driven bars, may not be entirely separable from those galactic properties which are influenced by the presence of the bar itself.

2.1.3 Radial Migration & Galactic Dynamics

First discovered in the disk of the Milky Way by Gilmore & Reid (1983), many galaxies have since been determined to be characterised by two distinct stellar components–a thick and thin disk—each differing in scale height, age and chemical composition (Fuhrmann, 1998; Dalcanton & Bernstein, 2002; Feltzing et al., 2003; Bensby et al., 2003; Yoachim & Dalcanton, 2006; Adibekyan et al., 2013; Rix & Bovy, 2013; Bensby et al., 2014). This relatively older stellar population in the thick disk can even be considered a fossil-like record of the early phase of galactic evolution (Buck, 2020; Khoperskov et al., 2021). Due to dynamical effects these thick and thin disks, however, appear to intersect within the phase plane making it difficult to separate and distinguish any features which may provide clues to their origins and evolutionary histories (Khoperskov et al., 2021). This is often attributed, at least in part, to processes of radial migration (Sellwood & Binney, 2002), gravitational interactions with the local environment (Weinberg & Blitz, 2006; D'Onghia et al., 2010; Purcell et al., 2011; Gómez et al., 2013, 2017) and the presence and/or evolution of non-axisymmetric spiral arm and bar-like features (Dehnen, 2000; Quillen & Minchev, 2005; Antoja et al., 2009; Minchev et al., 2011). Instead, the primary distinguishing feature between the disks lies in their chemical compositions, specifically it is common to use the ratio between α-elements relative to iron over a range of metallicities ([α/Fe]-[Fe/H]) which is observed to obey a bimodal distribution over the Milky Way disk (Hayden et al., 2015; Agertz et al., 2021) and in the disks of other, similar spiral-type galaxies (Kobayashi, 2016; Vincenzo & Kobayashi, 2020), to distinguish each of the thick- and thin-disk population components.

Many mechanisms appear capable of producing such distinctly dichotomous disk structure, such that there remains no consensus in the academic community regarding which should be the most likely. However, most agree that the determination of a theoretical framework for these complex structural and chemo-dynamical trends in the disks of galaxies must be essential for understanding how the Milky Way and other similar galaxies are formed and evolved (Freeman & Bland-Hawthorn, 2002; Bland-Hawthorn et al., 2019; Buck, 2020; Agertz et al., 2021). Popular theories which are able to produce similar chemically distinct disks are: vertical disk heating by satellite encoun-

ters (Quinn et al., 1993; Villalobos & Helmi, 2008), the two infall scenario (Chiappini et al., 1997; Grisoni et al., 2017; Spitoni et al., 2019), accretion of satellite stars (Abadi et al., 2003), gas-rich or major mergers (Brook et al., 2004; Calura & Menci, 2009; Belokurov et al., 2018; Helmi et al., 2018), a central star burst (Grand et al., 2018), star formation in turbulent gaseous disks at high redshift (Noguchi, 1998; Bournaud & Elmegreen, 2009), or a purely secular formation mechanism via radial migration of kinematically hot stars from the inner to the outer-disk (Schönrich & Binney, 2009a; Loebman et al., 2011; Roškar et al., 2012).

Radial migration is a general term often used to describe the processes capable of displacing stars over large radial distances and restructuring a galaxy over time. Initially identified through angular momentum changes at co-rotation between the pattern speeds of stars and spiral patterns, as well as at Lindblad resonances (Lynden-Bell & Kalnajs, 1972), this radial migration allows for stars to change positions on ∼kpc scales without leaving dynamical traces (e.g. Sellwood & Binney, 2002). These displaced stars then serve to mix the chemically distinct components which would otherwise be the equilibrium star formation conditions for different parts of the disk (Sellwood & Binney, 2002; Roškar et al., 2008; Schönrich & Binney, 2009a; Minchev et al., 2013). The specific mechanism responsible for such migratory behaviour is thought to be the outcome of two distinct effects: blurring (Schönrich & Binney, 2009b) and churning (Sellwood & Binney, 2002). In this case, blurring corresponds to a change in amplitude of the radial oscillations around an average guiding radius (R_g) for the orbit. Any star in the galaxy can be considered to be born from a GMC on a roughly circular orbit from which it is then scattered some time later such that the orbit becomes radially extended but the guiding radius, and thus the angular momentum (L_z) is unaltered. Comparatively, churning is triggered by torques from the non-axisymmetric features of the disk, such as the bar and arms, which can cause angular momentum changes in the stellar orbits but with no associated change to the orbital eccentricity (Sellwood & Binney, 2002; Schönrich & Binney, 2009b).

In general, both processes are responsible for transporting kinematically hot stars from the inner-disk to the outer-disk and thus, producing observed features in the disk of our own galaxy, as well as in similar external galaxies (Schönrich & Binney, 2009a; Loebman et al., 2011; Roškar et al., 2012; Buck, 2020). Radial migration has been previously associated with flat age-metallicity relations (e.g Casagrande et al., 2016), the metallicity-rotation velocity relation (e.g Allende Prieto et al., 2016; Kordopatis et al., 2017; Schönrich & McMillan, 2017), mono-age population flaring in the outer-disk (e.g Minchev et al., 2012, 2015) and as a means to drive the aforementioned [α/Fe]-[Fe/H] bi-modality of stars into spatially distinct thick and thin disk

structures (e.g Minchev et al., 2012; Kubryk et al., 2013; Vera-Ciro et al., 2014; Grand & Kawata, 2016; Kawata et al., 2017; Toyouchi & Chiba, 2016; Mikkola et al., 2020). Yet, for what is a comparatively well-determined process, we are still a long way from a comprehensive determination of radial migration, its causes and effects as pertaining to specific conditions within a given galactic structure at any given evolutionary period and what that means for which stars in the galaxy are likely to undergo migration and which of the two process will drive it.

Many have attempted to quantify these features via analytical methods (e.g. Sellwood & Binney, 2002; Schönrich & Binney, 2009a,b; Schönrich & McMillan, 2017), numerical simulations (e.g. Roškar et al., 2008; Halle et al., 2015; Aumer et al., 2016a,b; Aumer & Binney, 2017; Mikkola et al., 2020) and, of course, various observational surveys (e.g. Minchev et al., 2018; Frankel et al., 2018). These studies have been previously concerned with determining the extent of migration, usually as a function of stellar position and/or velocity relative to a mid-plane (e.g. Schönrich & Binney, 2009a,b; Schönrich & McMillan, 2017; Solway et al., 2012; Vera-Ciro et al., 2014; Vera-Ciro & D'Onghia, 2016), although other metrics have also been considered, such as dynamical temperature (e.g. Daniel & Wyse, 2018) or vertical/radial action (e.g. Mikkola et al., 2020). The relative effects of varying disk structures, such as barred and non-barred spirals, have also been a major focus (e.g. Sil'chenko & Smirnova, 2010; Grand et al., 2012; Di Matteo et al., 2013; Minchev et al., 2013; Kawata et al., 2017; Lin et al., 2017; Halle et al., 2018; Khoperskov et al., 2018), likely due in particularly to the torques from these non-axisymmetric features driving the specific radial migration process of churning. However, it is relatively less common to find studies which consider the different evolution histories of these galaxies, and consequently whether the processes driving the formation of different significant non-axisymmetric disk structures similarly drives radial migration to differ across these disks.

2.2 Resolved Target Galaxies

Observationally derived values for the attributes of specific nearby galaxies were intentionally employed herein to situate the galaxy-scale simulations performed into a context which is both realistic and of direct relevance for future comparisons with observational results. The target galaxies were selected primarily due to the wealth of both modern and historical observational survey data available. Each has long been determined to be of barred-spiral type with relatively face-on inclinations and local distances, which are conducive for taking detailed observational measurements.

2.2.1 NGC4303 - Isolated Target

NGC 4303 is a nearby barred-spiral galaxy, likely associated with the Virgo cluster of galaxies (Binggeli et al., 1985; Ferrarese et al., 1996). Determined to be of Sbc-AB type morphology, this galaxy has an approximate local distance of 16.1–17.6 Mpc with an inclination angle of 25.0 degrees (Schinnerer et al., 2002; Utomo et al., 2018). The observationally derived rotation curve is generally flat with deviation only in the very central region where it peaks sharply (Guhathakurta et al., 1988; Sofue, 1997; Yajima et al., 2019; Lang et al., 2020). Due to the relatively straightforward geometry, where it appears almost completely face-on to the line-of-sight; the active galactic nuclei of LINER/Seyfert 2 type (Ho et al., 1997); and, the possibility of a double bar, NGC 4303 has been the target of a number of observational studies, particularly focused on the central region and constraining its dynamics or morphology (Sofue, 1997; Helfer et al., 2003; Kuno et al., 2007; Momose et al., 2010). Egusa et al. (2009) attempted to determine a pattern speed (Ω_P) from CO–Hα offsets but, due to insufficient measurements, the uncertainty dominates ($\Omega_P \sim 24 \pm 29\,\mathrm{km\,s^{-1}\,kpc^{-1}}$). Other studies, both through observation and simulation, have also sought to derive pattern speeds for the central bar region, although these are generally inconsistent due to variations in the determination for the radius values which should constitute this region with $R_{\mathrm{centre}} = 2.8 \sim 9.2\,\mathrm{kpc}$ (Colina & Wada, 2000; Rautiainen et al., 2005; Egusa et al., 2009).

In terms of star formation features, Utomo et al. (2018) derive the stellar mass as $\sim 7.943 \times 10^{10}\,\mathrm{M_\odot}$ and SFR of $5.248\,\mathrm{M_\odot\,yr^{-1}}$ from CO measurements at 120 pc resolution. NGC 4303 also has an estimated average time for massive star formation from molecular clouds in the spiral arms (t_{SF}) of $10.8 \pm 5.7\,\mathrm{Myr}$ (Egusa et al., 2009) which is consistent with the age of young clusters in Hα determined by Koda & Sofue (2006) to be approximately 10 Myr. The gas mass derived was $5.3 \times 10^9\,\mathrm{M_\odot}$ with average surface density of $36\,\mathrm{M_\odot\,pc^{-2}}$ across $160''$ ($\sim 12\,\mathrm{kpc}$) in the molecular disk (Momose et al., 2010). From this, NGC 4303 is determined to have an overall average SFR surface density of $8.3 \times 10^{-2}\,\mathrm{M_\odot\,yr^{-1}\,pc^{-2}}$ with the bar contributing $7.6 \times 10^{-2}\,\mathrm{M_\odot\,yr^{-1}\,pc^{-2}}$, approximately 10% lower than the overall disk average, and arms $9.8 \times 10^{-2}\,\mathrm{M_\odot\,yr^{-1}\,pc^{-2}}$, approximately 10% higher than the overall disk average (Momose et al., 2010). Subsequent studies confirm this observation that NGC 4303 shows a lower SFE in the bar than in the spiral arms (Muraoka et al., 2019; Yajima et al., 2019). In general, when compared to the distribution of galaxies assessed by Kennicutt (1998), NGC 4303 appears to have higher than average star formation activity (factor of ~ 5) according to observations (Momose et al., 2010; Yajima et al., 2019).

2.2.2 NGC3627 - Tidally-driven Target

NGC 3627 is a barred-spiral galaxy of morphological type SABb according to the Third Reference Catalogue of Bright Galaxies (de Vaucouleurs et al., 1991). Similar to NGC 4303, the isolated target, this galaxy also hosts an active nucleus of the LINER/Seyfert 2 type AGN (Ho et al., 1997). However, NGC 3627 is historically considered to have experienced tidal interaction and been affected by the nearby galaxies NGC 3623 and NGC 3628 at some point in their evolutionary history, due in particular to the slight asymmetry in arm structure observable at optical wavelengths and a distorted HI gas distribution (Haynes et al., 1979). Additionally, significant distortion is also evident in the disk in polarised maps soft X-ray emission (0.2–1 keV), as well as a large asymmetry in hot gas temperature on the bar edges which implies a recent collision with a dwarf companion galaxy (Wezgowiec et al., 2012). The inclination angle of approximately 60 degrees has made NGC 3627 a relatively popular target for CO mapping and the study of molecular gas properties, as well as star formation activity (Reuter et al., 1996; Helfer et al., 2003; Kuno et al., 2007). Hirota et al. (2009) determined a pattern speed of $\Omega_P = 39\,\mathrm{kms^{-1}kpc^{-1}}$ for the galaxy from measurements of ^{12}CO (1-0) data and the method prescribed by Kuno et al. (2000). Law et al. (2018) estimate NGC 3627 to have a total dynamical mass of $4.94 \pm 0.7 \times 10^{10}\,\mathrm{M_\odot}$ at a galactocentric radius of $\sim 6.2\,\mathrm{kpc}$ ($121''$) from CO (2-1) emission measurements.

Additionally, there is also postulated to be a correlation between the kinetic temperature of gas in NGC 3627 and star formation efficiency (Law et al., 2018). Considering the relationship between molecular gas and star formation activity, NGC 3627 shows significant differences in the SFR from region to region but the bar itself has very low observable star formation efficiency (Watanabe et al., 2011). The bar-ends, however, show the most intense star formation of any region with SFE for the three regions Spiral Arm, Bar-End, and the Nuclear Region determined by Watanabe et al. (2019) to be 1.3 ± 0.4, 5.7 ± 1.7 and $1.8 \pm 1.0 \times 10^{-9}\,\mathrm{yr^{-1}}$ respectively. Despite this, the chemical composition in these regions appears to be quite similar, indicating that the characteristic chemistry on the observed scale is generally insensitive to physical conditions and local effects, such as the star formation rate (Watanabe et al., 2019). Many studies of NGC 3627 are concerned by this significant variation between regions, particularly at the bar-ends and have endeavoured to attribute physical effects to such results (e.g. Casasola et al., 2011; Watanabe et al., 2011; Beuther et al., 2018; Law et al., 2018; Watanabe et al., 2019).

2.3 Numerical Simulation Method

To produce the simulations for analysis it was necessary to develop a set of initial conditions which would evolve to form a bar under the specific impetus of the formation mechanisms selected for this evaluation: the first, which relies on an initial instability within the disk to trigger bar formation; and the second, which requires the external impetus of a passing companion to drive structure formation in the disk. From these initial conditions it was then possible for the simulations to be evolved via SPH numerical methods. For repeatability, the particulars of this process are also presented in brief.

2.3.1 Simulated Disk Specifications

From two initial conditions constrained to align with surface density profiles and kinematic data of the target galaxies NGC 4303 and NGC 3627 (see Section 2.2), three simulated disk galaxies which evolve into late-type barred-spirals were produced. These are indicative of either isolated bar evolution, motivated by disk instability (IsoB, TideNC), or a tidally-driven bar evolution, arising from interaction-affected development (TideB). All three discs have gas mass resolutions of approximately $1000\,\mathrm{M}_{\odot}$ (IsoB$\sim 1044\,\mathrm{M}_{\odot}$; TideB, TideNC$\sim 1084\,\mathrm{M}_{\odot}$) and active N-body particle components for each bulge and disk stars, gas and dark matter in the simulation. However, it is noted that the gas component in each of these simulations is singular and does not necessarily differentiate between molecular and atomic gas components. The minimum resolution was set to require a threshold of at least 10^6 disk particles, as this has been prescribed to be a limiting factor in order to properly capture the spiral and bar features in similar N-body galaxy simulations (Fujii et al., 2011). The mass and scale length parameters for each disk can be found listed in the following table (Table 2.1).

Table 2.1: Mass (in units of $10^{10}\,\mathrm{M}_{\odot}$) and scale length (in units of kpc) for the initial condition of each simulated disk galaxy, with the distance parameter for the companion defined by closest approach (in kpc).

	M_{gas}	$M_{*\mathrm{disc}}$	$M_{*\mathrm{bulge}}$	M_{halo}	$M_{\mathrm{companion}}$
IsoB	0.522	2.611	0.402	37.16	-
TideB	0.759	2.441	0.072	42.57	2.401
TideNC	0.759	2.441	0.072	42.57	-
	a_{gas}	$a_{*\mathrm{disc}}$	$a_{*\mathrm{bulge}}$	a_{halo}	$b_{\mathrm{companion}}$
IsoB	3.090	2.060	2.057	20.57	-
TideB	3.705	2.470	0.405	20.26	10
TideB	3.705	2.470	0.405	20.26	-

To develop the isolated initial condition, the GALIC package of Yurin & Springel (2014) was used to generate the majority of disk components. This GALIC output was characterised by a spherical dark halo and stellar bulge following a Hernquist profile with axisymmetric velocity structure and a predefined net rotation value. The stellar disk was generated as a thin disk of thickness 0.2 times the radial scale length with similar axisymmetric velocity structure and defined dispersion ratio between the radial and vertical velocities, as well as a net rotation value. Through an iterative method of testing initial conditions at low resolution, the initial stellar mass ratios were prescribed to be $m_{\rm disc} = 0.065$ and $m_{\rm bulge} = 0.01$ respectively, as a fraction of total mass; and the velocity dispersion ratio set to $\langle v_z \rangle^2 / \langle v_r \rangle^2 = 1.5$ for the stellar disk. These were considered appropriate based on a preliminary visual assessment of the evolved morphological features, such as the presence of a distinguishable bar. Additionally, or the purpose of studying star formation, a gas component is also necessary, however gas is not included in the GALIC initial conditions. To introduce a functional gas disc, a component copied from the existing stellar disk particles produced by GALIC was added, rotated in the disk plane 180 degrees out of alignment and expanded to 1.5 times the stellar radius. The subsequent gas particle mass was also modified to be comparable with the observed gas-mass fraction and derived values for the total gas mass of NGC 4303 (Iles et al., 2022).

Comparatively, to develop the initial condition to be perturbed and consequently produce a bar triggered by a tidal interaction, a modified version of the Rise-S10 simulation of Pettitt & Wadsley (2018) was adopted. Rise-S10 is specifically selected as this disk is clearest case of a bar being tidally induced in the study of Pettitt & Wadsley (2018) on interaction-driven bars. For this purpose, the original initial condition of Rise-S10 has to be appropriately rescaled in both mass and scale lengths in order to be comparable with both the isolated initial condition and observations of NGC 3627. Briefly, this corresponds to scaling by factors 0.5, 0.4 and 2 for distances, stellar mass and gas mass respectively, before the initial condition was constrained to align with surface density profiles similar to the method for the isolated case. The interacting companion, however, was not specifically constrained to any observational counter-part based on NGC 3627 and its neighbours. The mass and length parameters are similarly scaled and the orbit remains as per the original system in Pettitt & Wadsley (2018) to trigger the desired bar formation as expected (Iles et al., 2022). This modified Rise-S10 is the initial condition for the two simulated disks presented in the following analysis: TideB (with the tidally-driven bar) and TideNC (with no companion). The difference between these two cases is that the companion component is directly removed from the initial condition of TideB and so, TideNC is allowed to evolve unaffected.

Based on these initial conditions, the three simulated disks could each be expected develop some bar structure within the central region on the strength of the Efstathiou et al. (1982) metric for a given disk to be stable to bar formation:

$$\epsilon_{\text{bar}} = \frac{V_{\text{max}}}{\sqrt{GM_d/a_d}} \tag{2.1}$$

Where G is the gravitational constant, V_{max} the maximum rotation velocity and a value greater than 1.1 is considered stable. The IsoB initial condition with a value of approximately $\epsilon_{\text{bar}} \sim 0.8$ is considerably more likely to form a bar than the TideNC initial condition which produces a value of $\epsilon_{\text{bar}} \sim 1$ but both fall within the bar forming limit. Based on this parameter, the interaction introduced to drive bar formation in TideB should be expected to–at least–hasten the bar forming process overall, however, it may also fundamentally change the nature of the bar which is eventually produced (Iles et al., 2022).

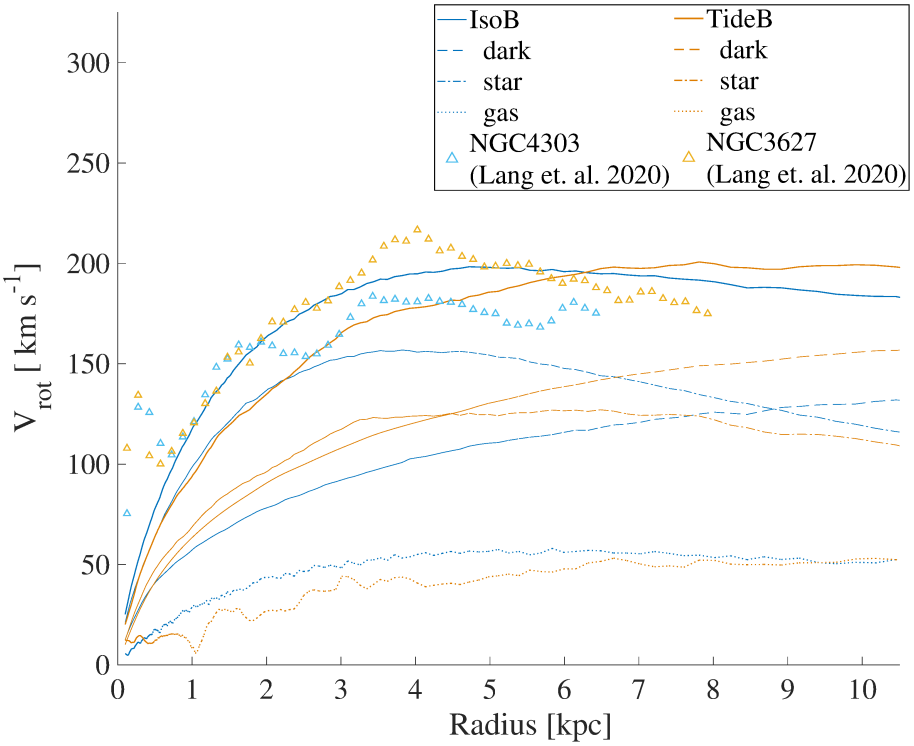

Figure 2.1: Rotation curves for both initial conditions (Iles et al., 2022). IsoB is identified by blue lines and TideB by orange. The different component contributions are denoted by various line styles (solid–total, dashed–dark, dot-dashed–stellar, dotted–gas). An example of observational measurements used to constrain these conditions is also included, represented by triangle points from the PHANGS survey data (Lang et al., 2020).

An additional assessment for the validity of the initial conditions for IsoB and TideB/TideNC was performed based on the general shape and features evident in the galactic rotation curve as compared to observations (Guhathakurta et al., 1988; Sofue, 1997; Yajima et al., 2019; Lang et al., 2020). The rotation curves for each initial condition are presented in Figure 2.1 including a breakdown of the rotation contribution from each component and the most recent observations of Lang et al. (2020). These profiles are generally flat, dominated by the stellar component within the disk radius and dark component in the outer-reaches. The rotation curve of the tidal initial condition is notably less dominated by the stellar component in the central region with a marginally faster rotation speed, compared to the isolated disk initial condition. An acceptable fit was determined to have a generally consistent overall shape and total velocity, as it was expected that the small-scale features, such as the peaks and wiggles which appear in the rotation curves of observed galaxies, will become apparent as the disks evolve, which can indeed be seen in Figure 3.5 in Chapter 3 (Iles et al., 2022).

2.3.2 Simulation Parameters

The specific simulation process was held to be consistent for each of the three disks and was performed using the GASOLINE2 smoothed particle hydrodynamics (SPH) code (Wadsley et al., 2004, 2017).

Each disk was evolved over a period of 1 Gyr using the standard hydrodynamical treatment advocated by Wadsley et al. (2017) with 200 neighbours and a Wendland C4 kernel (Dehnen & Aly, 2012). Gravitational softening lengths were prescribed for each component to take values of 0.1 kpc for the halo, 0.05 kpc for stars and 0.01 kpc for gas. A temperature threshold of 300 K and density threshold of 100 atoms/cc were set to be the primary conditions for star formation with a star formation efficiency of 10% ($C_* = 0.1$), a Chabrier (2003) IMF and convergent flow requirement. These are consistent with previous studies (e.g. Saitoh et al., 2008; Tasker & Bryan, 2008; Pettitt et al., 2017), as well as the standard sub-grid prescriptions of GASOLINE (Katz et al., 1996; Stinson et al., 2006; Wadsley et al., 2004, 2017).

The implementation of UV and photoelectric heating, as well as metal cooling in the form of a tabulated cooling function (Shen et al., 2010), recovers a two-phase thermal profile comparable to the ISM (Wolfire et al., 2003) from an initially isothermal (10^4 K) gas profile. Stellar feedback is implemented from supernova following the super-bubble method of Keller et al. (2014). This feedback mechanism is generated from clusters of young stars instead of individual supernovae and is consequently more efficient in describing gas motion, regulating star formation and producing the expected strong outflows

which are all relevant to support studies of star formation in disk galaxies (Keller et al., 2014).

The 1 Gyr period of integration time is considered the early period of bar formation and accounts for only a small number of complete disk rotations. This is intentionally designed to capture the period of disk evolution where the effects of the tidal perturbation are most prominent in the interacting case, thus highlighting any fundamental differences arising between the isolated and tidally-driven bar formation mechanisms.

Chapter 3

Classification of Simulated Disk Features

3.1 General Observable Features

Direct physical results, such as the gas and stellar density distributions from each of the three simulations, are presented in the following as a visual illustration of the disk structure evolution in the 1 Gyr time period of interest.

3.1.1 Gas & Star Particle Distributions

Initially, it is possible to assess the face-on morphological structures of the gas and stellar populations in the three disks from Figure 3.1, with the disk plane here set to occupy the xy-plane. The colour weighting accounts for the mass density of each component and is held constant in each case. Each column corresponds to evolutionary time periods in steps of 100 Myr of simulation time. To describe each disk in terms of general features, both the IsoB and TideB case form similar bars and primarily two-arm spiral structure, although the timescale for the formation of these structures is slightly different as the interaction of the tidal disk drives a formation time $\sim$ 200 Myr faster than IsoB with the isolated environmental conditions (Iles et al., 2022). At a given evolutionary period when the bar is well developed, the large-scale structural features of these two disks do not appear substantially different. The bar lengths and strength appear visually similar within each disc. The number and prominence of the arms, as well as their pitch angles, are also similar, although there are a number of obvious smaller-scale differences visually discernible within these general morphological attributes.

The IsoB case, which formed a bar through some initial disk instability, seems to evolve from a more flocculent type galaxy into a two-armed structure as the bar grows. Conversely, the TideB case is strongly affected by the

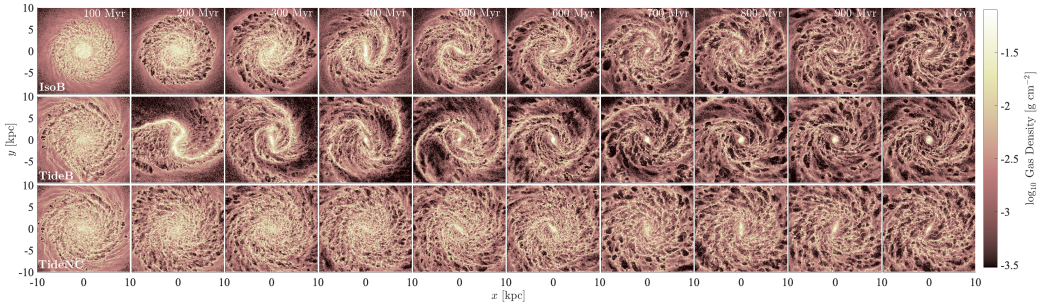

(a) Gas density distribution for all gas particles in the simulation.

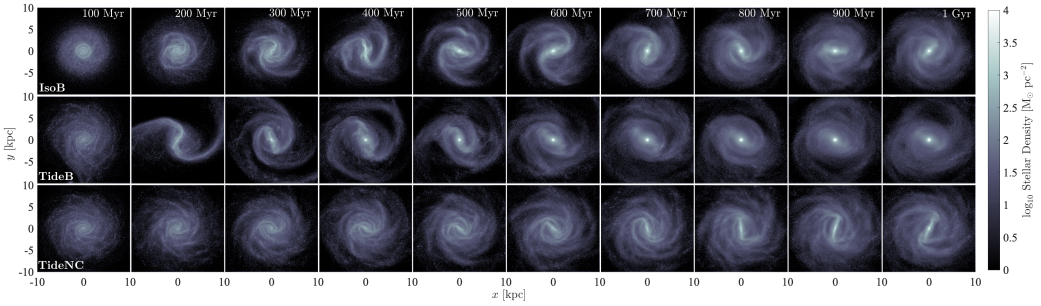

(b) Stellar density distribution for all stars in the simulation.

Figure 3.1: Projections of the face-on gas and stellar density distributions set into the xy-plane for each: IsoB, TideB and TideNC. Columns step in time by 100 Myr to the total simulation time of 1 Gyr.

interaction occurring at approximately 100 Myr (closest approach $\sim$ 94 Myr), producing clear, crisp two-arm features. These features however, are significantly impacted by gravitational effects, both from the inner-disk and the external companion, constantly strengthening and decoupling over the period. As the simulation evolves, the bar forms and the disk stabilises. Due to the decoupling of the arms in the tidally-driven case the bar length intermittently appears to extend. This may also affect an assessment of bar orientation. Additionally, the third case, TideNC, the tidally-driven disk without the influence of the companion interaction, is more stable to isolated bar formation than the primary isolated disk considered (IsoB) but does also appear to form a bar eventually. This disk, however, forms a bar with visibly different morphology to both the IsoB and TideB cases, which is particularly evident in the later panels of Figure 3.1b.

The side-on structure of the stellar population for the simulated disks is also presented in Figure 3.2, although this is not something that can be observed for the target galaxies directly (based on the line-of-sight). The representation in Figure 3.2 is particularly convenient for determining the bar effects on the vertical distribution of the stellar population. In the central regions of this figure, a cross- or X-shape is particularly evident in the barred periods of both

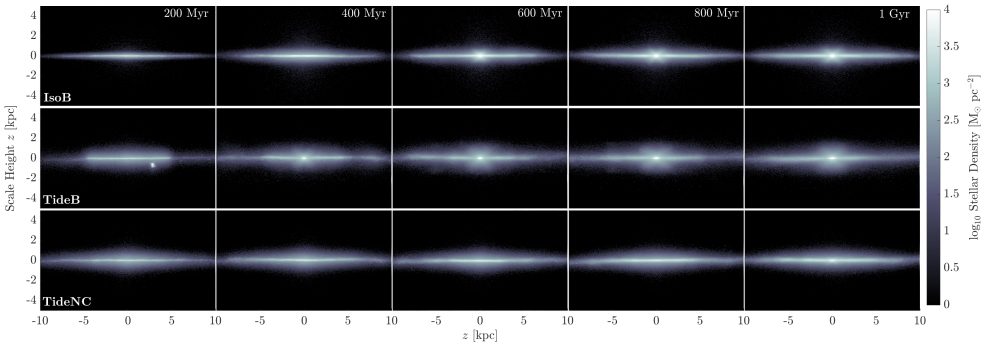

Figure 3.2: Projection of side-on stellar density distribution set into the xz-plane for all stars in the simulation (initial condition + new stars formed) for each case: IsoB, TideB and TideNC. Columns step in time by 100 Myr to the total simulation time of 1 Gyr.

IsoB and TideB. Such morphology is often associated with bar formation and the warping of the bar in and out of the disk-plane as it forms (e.g. Raha et al., 1991; Łokas, 2018; Sellwood & Gerhard, 2020). Interestingly, while the face-on projections of TideNC also appear to show bar formation occurring in the later periods of this disk's evolution, no similar feature is discernible in Figure 3.2. This directly implies a significant difference between the bar formed in TideNC and those of the former two cases (IsoB and TideB). It also affirms the interaction as the primary influence on bar formation in TideB, as intended. Further consideration for how these differing disk vertical structures evolve is provided in Chapter 5, although it remains a point of interest.

3.1.2 Comparison to Target Galaxies

It can be said that the simulated disks produced with the tailored initial conditions from observation are quite successful analogues–at least based on preliminary visual assessment. Selecting snapshots which appear most similar to the observed targets, it is possible to use the simulation output to produce synthetic observation maps and compare the two galaxies. In Figure 3.3 these synthetic observations of the two simulated disks IsoB and TideB (Pettitt, 2022) are presented alongside similar maps of the observed target galaxies produced from the Sloan Digital Sky Survey (SDSS; Ahn et al., 2012). From such a visible comparison, it is apparent that the face-on morphologies and features of these galactic disks appear remarkably similar.

As a further assessment of the nature of the bars formed in the simulations, Figure 3.4 displays the stellar surface density profiles, both along the bar (major axis) and perpendicular (minor axis), for each IsoB and TideB which should be comparable to the observed targets NGC 4303 and NGC 3627. These val-

(a) IsoB simulated disk alongside SDSS image data of observed target NGC 4303 (Ahn et al., 2012)

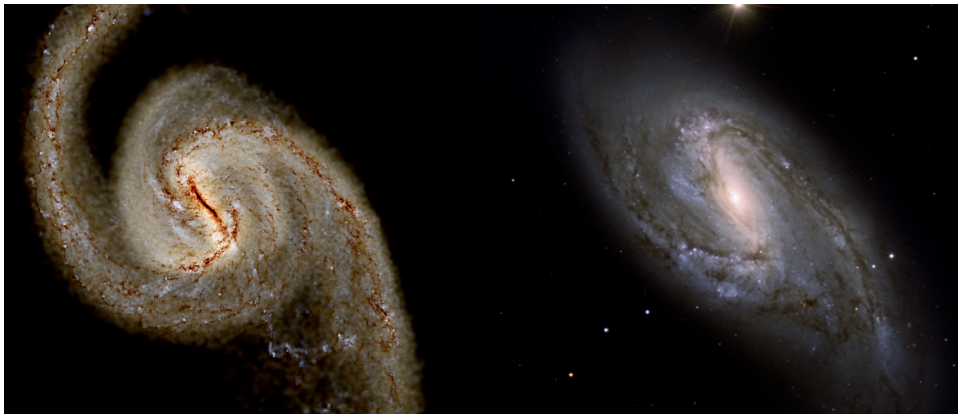

(b) TideB simulated disk alongside SDSS image data of observed target NGC 3627 (Ahn et al., 2012)

Figure 3.3: Synthetic observation maps (Pettitt, 2022) of two simulated galaxies : IsoB, a bar formed in isolation similar to NGC4303 (a) and TideB, tidally-driven by an interaction similar to NGC3637 (b).

ues are taken at two 100 Myr time-steps immediately following visible bar formation including the period where these disks appear most analogous to the observed targets. It is apparent that these disks exhibit similar profiles both parallel and perpendicular to the bar orientation. The stellar surface density within the central region clearly decreases exponentially and in a manner which is noticeably steeper than the surrounding non-barred regions of the disks. Hence, both cases can be categorically described as hosting very similar bars of exponential (late) type, rather than the alternative flat (early) type (Elmegreen & Elmegreen, 1985). This is consistent with observations of NGC 4303 and NGC 3627 with later type Hubble classifications (de Vaucouleurs et al., 1991), as well as the exponential disk profile used to produce the initial simulation conditions. Thus, it may be naively expected that these

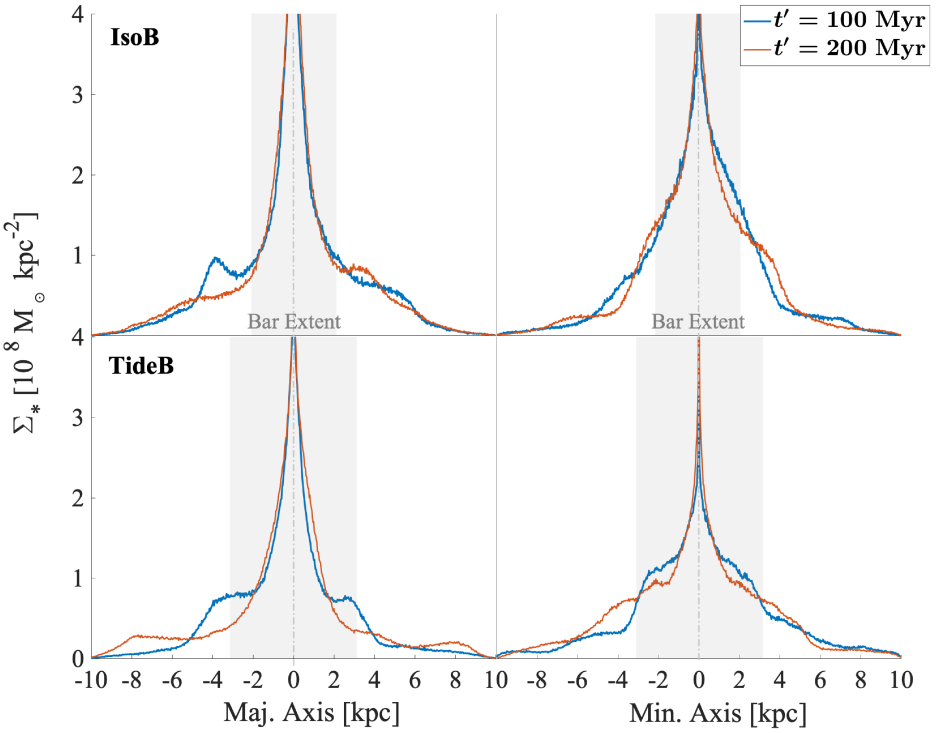

Figure 3.4: Stellar surface density profiles along the major (left) and minor (right) axis of the bar for each case in the time periods $t' = 100, 200$ Myr which are immediately post-bar formation (Iles et al., 2022). The region shaded in grey indicates the approximate bar extent (IsoB: $R_{\rm bar} = 2.10$ kpc; TideB: $R_{\rm bar} = 3.12$ kpc).

two bars in particular should impact the host-galaxy disk structure in a similar manner (Iles et al., 2022).

To account for the difference in bar formation time between the differently triggered disks, in some cases of comparison it is more appropriate to compare the periods relative to bar origin rather than the complete evolutionary time-scale of the disk (e.g. as in Figure 3.4). On these occasions, a shifted time-scale is employed (t') wherein the integration time t is shifted relative to the bar formation time and rounded to the nearest 100 Myr. Under this time scale, the barred period of each simulation will commence at the time $t' = 0$ Myr. This revised time of $t' = 0$ corresponds to the $t = 400$ Myr snapshot of IsoB, the $t = 200$ Myr snapshot for TideB and $t = 700$ Myr snapshot in TideNC.

3.2 Dynamical Features

Non-axisymmetric morphological features, such as bars and arms, have been shown to significantly impact to the disk dynamics and perturb galactic veloc-

ity field (e.g. de Blok et al., 2008). Observations of NGC 4303 and NGC 3627 are no exception as both exhibit clear non-circular motions, which are apparent in both the moment maps and undulations in the rotation curves (e.g. Schinnerer et al., 2002; Law et al., 2018). The observed rotation curves were used to constrain the two initial conditions in order to produce these simulations (see Figure 2.1) but these initial conditions were, by nature, smooth and structure-less. After the evolution of the disk, the observational analogues: IsoB and TideB, can again be compared to the observational data. Figure 3.5 similarly presents the rotation curves for the observed galaxies as a comparison to the early stages of bar evolution in the IsoB and TideB disks.

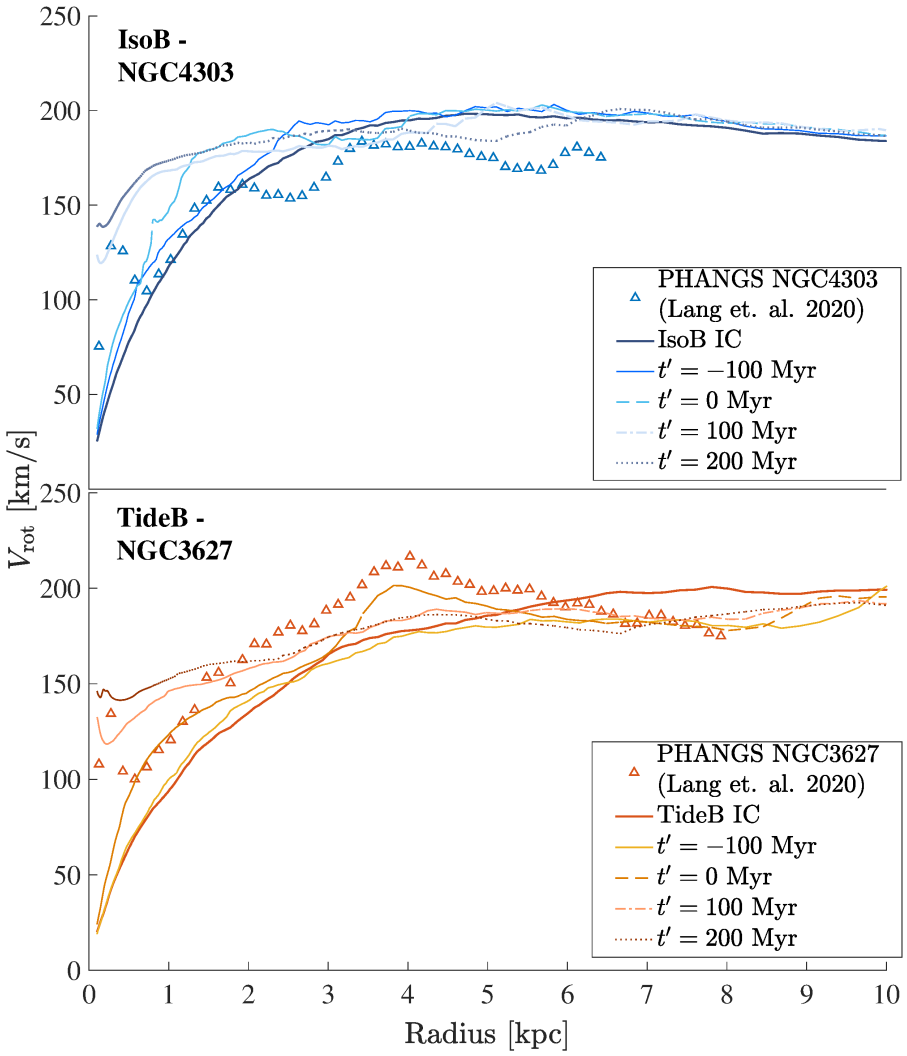

Figure 3.5: Rotation curves for each case at the key intervals $t' = [-100, 0, 100, 200]$ Myr (Iles et al., 2022) as well as the initial condition and observation results from the PHANGS survey data (Lang et al., 2020).

There is clearly a significant variance in the shape of the rotation curve over the time period investigated. Both curves tend to rise up in the inner-disk as the bar grows, with outer undulations decaying on 100 Myr time-scales. Of particular note is the spike around 4 kpc in the TideB case that lines up particularly well with the NGC 3627 profile at $t' = 0$ Myr–the curve closest to the the period when the model is considered best matched to the observed galaxy (Iles et al., 2022).

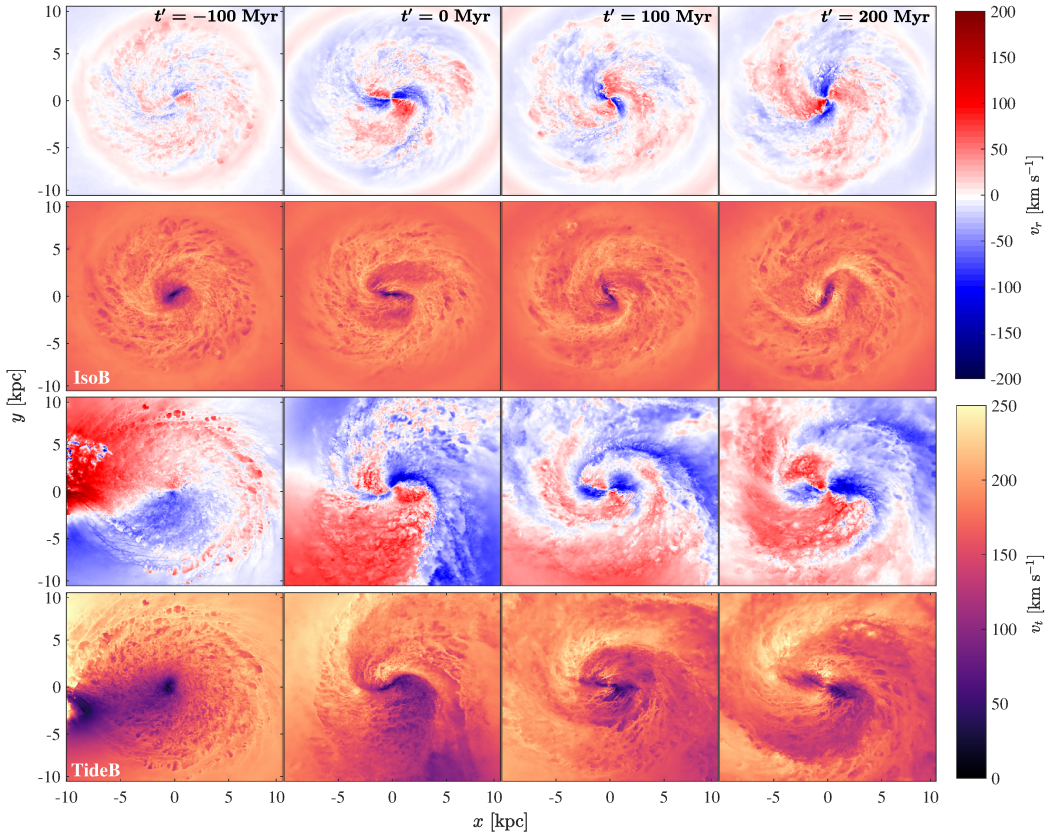

Figure 3.6: The velocity of gas projected into the same xy- (disc-aligned) plane. For each case, radial (top) and tangential (bottom) velocities are shown. The colour scale is set to be consistent over both cases to highlight the difference in magnitude between the results. The columns show the evolution through time at the same periods as Figure 3.1 denoted instead by the t' scale (Iles et al., 2022).

These non-circular velocities can also be visibly associated with structural features in the disk morphology via a face-on representation of the azimuthal and radial streaming motions. In Figure 3.6, these a presented for the gas component in the early evolutionary stages of the two disks (IsoB and TideB). The top two rows display the velocity profiles for IsoB evolving with time, while the lower two rows instead present the interaction driven TideB for comparison.

Between these similarly barred disks, the tidal forces in the interacting case significantly increase the overall degree of non-axisymmetric motion. Only the central regions of the IsoB case seem to show similarly high non-circular velocities which are comparable to the values that fill the entire disk regions of the post-interaction TideB results. Both velocity components in TideB indicate that asymmetries are strongest during closest approach ($t' = -100\,\mathrm{Myr}$). These are especially clear in the outer disc, whereas, IsoB is relatively unperturbed outside the bar region. Such strong outer asymmetries in TideB correspond with a migration of the system centre of mass, which has been corrected for in Figure 3.6. Additionally, while these do decay over time as the companion moves further away, it remains many times larger than any similar features in the isolated disk (Iles et al., 2022).

A clear central quadrupole velocity signature is evident in the central region of the radial velocity plots for both IsoB and TideB in all periods after the bar is formed. This not unexpected as such a feature is commonly considered indicative of the presence of a bar in the inner disc, as material streams radially to follow elliptical orbits aligned with the bar (e.g. Bovy et al. 2019). The bar kinematics appear strikingly similar between the two models, also showing clear similarities in the azimuthal motion, such as lower v_t along the bar-axis, with two 'lobes' of higher v_t perpendicular to the bar-axis in the galactic centre (e.g. Renaud et al., 2015). The extent of the quadrupole-like region acts a good visual approximation of the bar extent. It can be seen that the radial size of the bar remains relatively constant once it forms which is also consistent with the similar assumption drawn from the visible assessment of Figure 3.1 in the previous section (Iles et al., 2022).

One particular point of comparison between the two velocity projections displayed in this way (Figure 3.6) is how the velocity features propagate radially. In IsoB the positive or negative radial motion traces a single feature from the galactic centre to the outer disc, following from the quadrupole to along the arms and outwards. In TideB, however, the feature is not so continuous, with the quadrupole radial velocity features being engulfed by the strong radial motions exhibited by the tidal arms. Such a signature is evidence of the rapid decoupling between the tidal arms and inner bar occuring in TideB. Bar and spiral decoupling is a known phenomena in isolated discs (e.g. Sellwood & Sparke 1988; Baba 2015) but has not been commonly discussed in the context of tidal interactions where arms are driven by external forces. The azimuthal response between the two arms of TideB is also asymmetric, with the northern (southern) arm appearing to rotate somewhat faster (slower) than the disk average. This is likely to promote significant asymmetries in galactic shear experienced by gas in each arm and will also affect the star formation conditions and subsequent stellar motions in this particular disk (Iles et al., 2022).

Chapter 4

Star Formation in Isolated and Tidally-Driven Bars

The following is representative of a comparison between the primary isolated bar IsoB (as analogous to NGC 4303) and the tidally-driven bar TideB (as analogous to NGC 3627) and the effects of these bars on star formation properties and the star forming ISM in the disk of each galaxy. The main focus is on the evolutionary periods directly preceding and post-bar formation with the intention to identify and distinguish the effects of bars with isolated origins from bars which have been tidally-driven into formation. Overall, this chapter is representative of the principal findings presented by Iles et al. (2022).

4.1 Star Forming History

Initially, the star forming history of each galaxy can be represented via a disk-averaged star formation record. This is presented in Figure 4.1 for the two simulated disks IsoB and TideB. The time axis in this figure shows the unaltered integration time for each simulation while a vertical line denotes the time of approximate bar formation ($t' = 0$) for each disk. The solid blue line traces the star formation history for the isolated IsoB case, whereas the orange dotted line maps the history of the tidally-driven case. It is of note that the time of closest approach for the companion in the tidal interaction occurs at approximately 94 Myr (Iles et al., 2022).

Both disks, regardless of the bar formation mechanism, appear to exhibit relatively similar star formation rates on average. Similarities are also apparent in the general shape of the star formation profile as it evolves. For example, there is evidence of an extended rise in star formation at around the time the bar forms in both cases. The relative shape of this increase is also similar, in terms of height and duration: IsoB shows an increase of $\sim \Delta\mathrm{SFR} =$

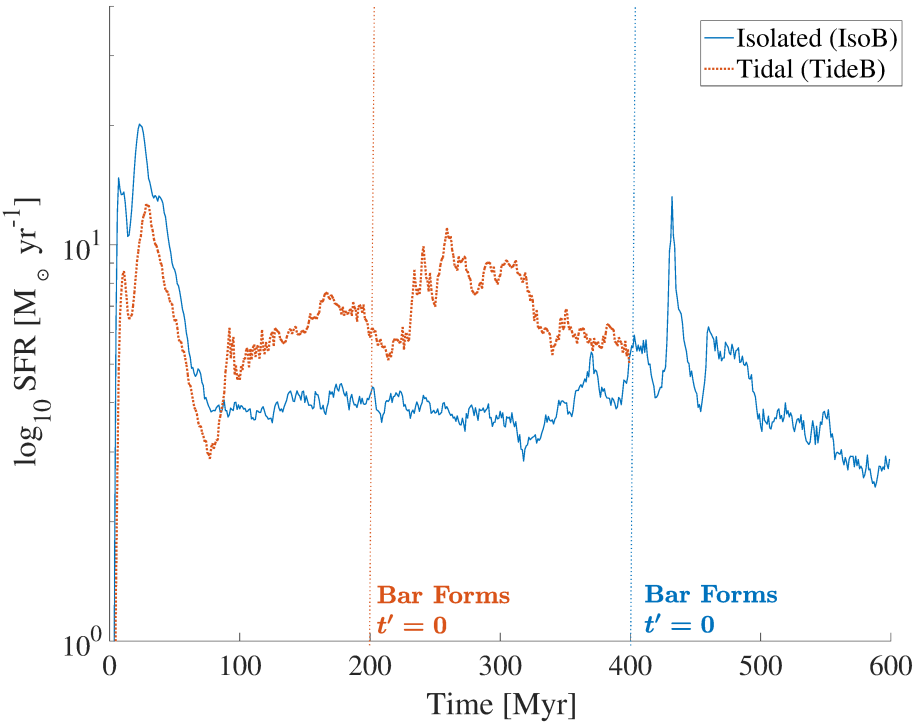

Figure 4.1: Star formation history for the two cases for the evolutionary period until $t' = 200\,\mathrm{Myr}$. The axis is set at original simulation time so, for each case, a vertical line denotes $t' = 0\,\mathrm{Myr}$. The solid blue line represents IsoB. The orange dotted line represents TideB. The large peak at $t < 100\,\mathrm{Myr}$ is an artefact of the simulation process. Vertical dotted lines approximately indicate bar formation times (Iles et al., 2022).

$3.08\,\mathrm{M}_\odot\,\mathrm{yr}^{-1}$ over approximately $\Delta t = 145\,\mathrm{Myr}$; while, TideB increases with $\sim \Delta\mathrm{SFR} = 3.79\,\mathrm{M}_\odot\,\mathrm{yr}^{-1}$ over a period of approximately $\Delta t = 127\,\mathrm{Myr}$. However, in the epoch preceding bar formation IsoB appears to maintain a relatively constant level of star formation (after the initial boost on start-up), while TideB clearly experiences an additional–earlier–extended rise and fall of star formation intensity similar to the boost upon bar formation evident in both the IsoB and TideB star forming histories (Iles et al., 2022).

The magnitude of the bar-triggered boost in SFR is similar for both the isolated and perturbed disks with values of 79% and 66% respectively. The earlier burst is significantly milder with only 31% increase from the previous baseline. This additional boost occurs just after the closest approach of the companion and, although smaller in amplitude than the bar effect, appears to persist for a similar duration. This earlier boost is therefore likely attributable to a starburst triggered by the interaction, producing such a double-peak shape in the trend of the star formation history in the tidally-driven TideB. In this

early epoch, the bar has not yet formed, while the density and SFR projections both show the two arm features dominate the disk. Hence, a logical assumption would be that this first starburst is expected to be predominantly limited to star formation in the strong tidally induced arms, rather than within the central region which later becomes the bar (Iles et al., 2022).

To study the morphological dependence of these star formation features in more depth, three key morphological regions were defined: the bar, arm and inter-arm components. Using Fourier decomposition, the relevant traits of the bar and arm components were analytically determined. Then, the inter-arm region could be defined as that which is neither bar nor arm within a certain radius of interest ($\sim 10\,\mathrm{kpc}$) determined to contain the majority of significant disk features in both disks. The extent of the bar region was determined from the amplitude of the Fourier $|A_2|$ mode. Identifying the radial extent of features in this mode allowed for the bar component to be defined with a simple radial criterion to form a central circular region encasing the full bar length for the purpose of this analysis. Furthermore, as the bar extent was found to be relatively constant, decreasing only a small fraction throughout the duration, a single value was adopted for the bar extent (IsoB: $R_{\mathrm{bar}} = 2.10\,\mathrm{kpc}$; TideB: $R_{\mathrm{bar}} = 3.12\,\mathrm{kpc}$). The arm component was subsequently classified by fitting a log spiral of the form $r = a\exp\{b\theta\}$ with a standard width of $\pm 1\,\mathrm{kpc}$ to the peaks of the polar angle θ in the disk-plane for the population at radii outside of the R_{bar} value (Iles et al., 2022).

Using these prescribed regions, it was also possible to decompose the total averaged star forming history of each disk into the constituent parts making up the different disk morphological structures. In Figure 4.2, a similar star forming history for each IsoB and TideB is plotted. However, this is instead a measure of the fractional contribution to star formation from each region relative to the total number of stars produced over the disk. As the regions are only defined and analysed on every step of 10 Myr, the history is only resolved at these points with each accounting for all stars formed in the 10 Myr period preceding it. In this figure, the blue line with crosses at each calculation point denotes the contribution from the defined bar region; the filled-in red circles indicate the contribution from within the arm regions; and finally, the open circles in magenta show the inter-arm contribution. The axis is set in the altered time relative to bar formation (t') with a similar vertical line at $t' = 0$ to indicate the approximate time of bar formation (Iles et al., 2022).

Star formation in the bar regions of both disks can be seen to increase steadily as the bar is formed, while the inter-arm region contributes the least star formation for the majority of each simulation. Comparatively though, this inter-arm contribution remains consistently at $\sim 10\%$ of the total stellar mass formed in the isolated IsoB, whereas the fraction is even lower in TideB, with

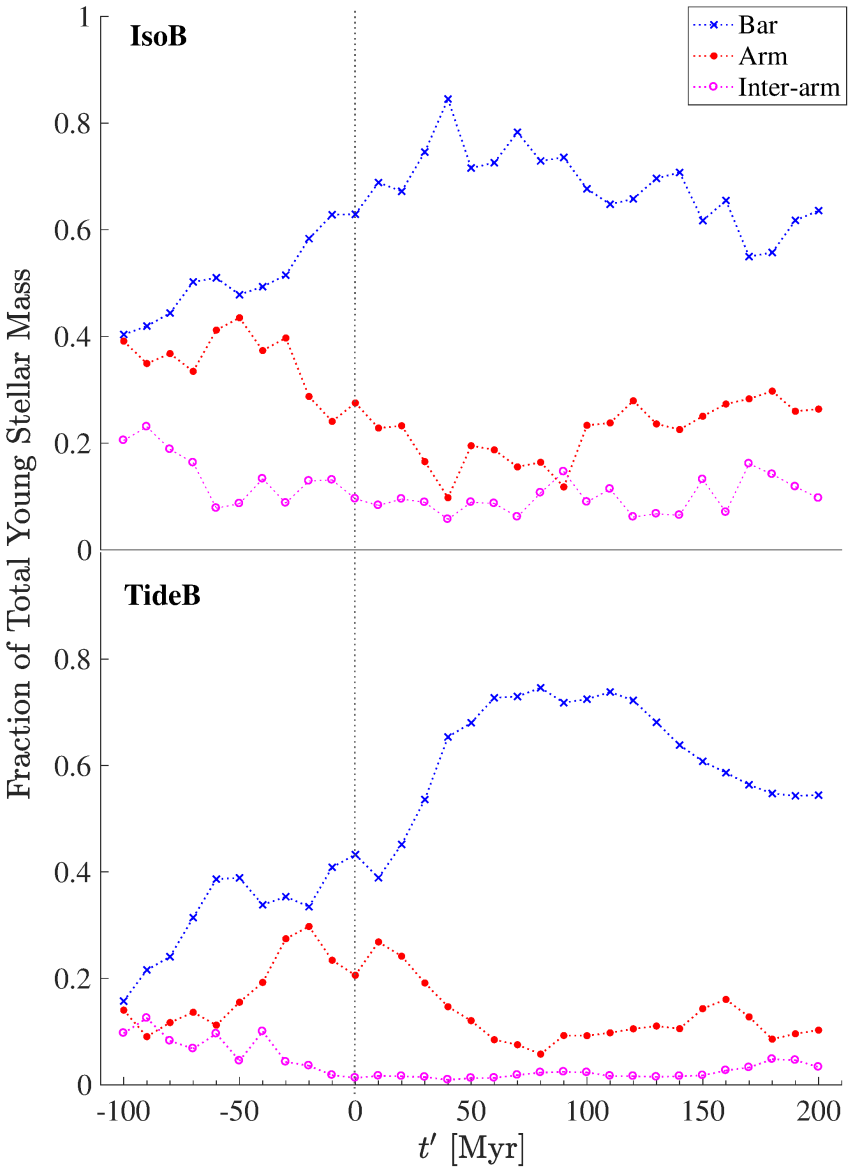

Figure 4.2: Fraction of stellar mass produced by each region (bar, arm, inter-arm) over the period of $-100 < t' < 200$ Myr in both IsoB and TideB. Each region is only defined on steps of 10 Myr, where the bar is denoted by a blue line with crosses at every 10 Myr point; the arms by a red line with filled-in circles; and the inter-arm with magenta line and open circles. The axis is set in the t' scheme with a dotted vertical line at $t' = 0$ to indicate the approximate time of bar formation (Iles et al., 2022).

$\sim 5\%$ or less of the stars forming in the inter-arm regions after the bar has fully developed. The predominant difference between the two disks, however, is evidenced by the star forming histories of the two differing arm components, particularly in the period before bar formation with $t' \leq 0$ Myr (Iles et al.,

2022).

The fraction of stars forming in IsoB initially appears to be similar in the bar and arm components during the early period of disk evolution ($t' \leq -50\,\mathrm{Myr}$), before becoming increasingly centrally dominated as the bar forms at $\sim t' = 0\,\mathrm{Myr}$. Contrastingly, the highest period of intensity for star formation in the TideB arms notably occurs over the exact period the bar is brought into existence ($-50 \leq t' \leq 50\,\mathrm{Myr}$). This corresponds to the period in Figure 4.1 where the smaller peak of star formation can be seen after closest approach and before the bar has completely formed. Compared to the IsoB case, which has a steady baseline level of star formation before bar formation, the interaction in TideB is expected to have prompted this burst of star formation. From this figure, it is possible to confirm this burst is indeed star formation predominantly located in the arms. Another feature, which is perhaps significantly different between the star forming histories of each disk, is also visible for periods $\sim t' > 50\,\mathrm{Myr}$. A potential periodicity appears in the bar component of IsoB which is not reflected in TideB at this time where there is a generally smoother profile. These features are essentially indistinguishable when considering the star formation history of the total contribution but are straightforwardly apparent when considering the contribution to star formation from each morphologically dependent region (Iles et al., 2022).

4.2 Star Forming Features

To more directly classify the star forming properties of these simulated galaxies, as well as to effectively compare with observational results for NGC 4303 and NGC 3627, it becomes necessary to consider such features as the star formation rates (SFR) and efficiencies (SFE). Here, SFR is defined as a measure of the number of new stars formed in a given time period (Δt_{SF}):

$$\mathrm{SFR}(t_i) = \frac{1}{\Delta t_{\mathrm{SF}}} \sum_{t_i}^{t_i - \Delta t_{\mathrm{SF}}} M_* \tag{4.1}$$

This is calculated at the current time (t_i) by a summation of all new stellar mass (M_*) produced during the star forming period (Δt_{SF}). This rate is then converted to a surface star formation rate (Σ_{SFR}) in order to be more comparable to the quantities measured in observations by binning over a $0.1 \times 0.1\,\mathrm{kpc}$ grid. The look-back time for star formation is the age range $\Delta t_{\mathrm{SF}} = 10\,\mathrm{Myr}$ which is comparable to the star forming time-scale determined observationally for NGC 4303 (Koda & Sofue, 2006; Egusa et al., 2009).

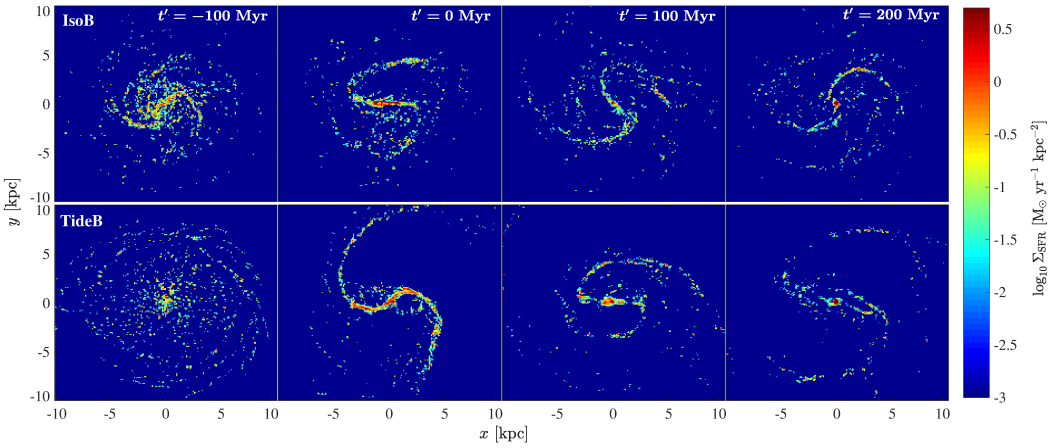

Figure 4.3: A projection of surface star formation rate (Σ_{SFR}) into the same xy- (disc-aligned) plane for the isolated (top) and tidally-driven (bottom) bar models. Σ_{SFR} is calculated by counting young stars particles with ages $< 10\,\mathrm{Myr}$ and then binning over a $0.1 \times 0.1\,\mathrm{kpc}$ grid (Iles et al., 2022).

4.2.1 Star Formation Rates in the Disk

A similar face-on projection in the xy-plane of this Σ_{SFR} is presented in Figure 4.3 for the two disks IsoB and TideB over the early bar formation periods considered in this chapter. The colour weighting for this figure is similarly consistent for both disks and all time periods, while the columns advance in steps of 100 Myr about $t' = 0\,\mathrm{Myr}$ (Iles et al., 2022).

From this figure, it is possible to visibly assess the location of current (or very recent) star formation, as well as the intensity of such formation. For example, the centre-most regions of each disk post-bar formation ($t' \geq 0\,\mathrm{Myr}$) are dominated by an almost circular, bulge-centred region with the highest star formation rate. This circular region also similarly expands as the bar evolves, a likely by-product of gas inflow to this central circumnuclear disk. However, the expansion rate is not similar. It can be directly observed that the radial extent of this region is approximately the same size for both disks at $t' = 100\,\mathrm{Myr}$ and yet, by the following $t' = 200\,\mathrm{Myr}$ snapshot, the circular region in the central region of TideB has become significantly larger than that of IsoB. This implies that by 200 Myr after the bar is formed TideB has developed a less concentrated but no less intense region of star formation in the central nuclear disk. This kind of central star formation can be commonly seen in barred systems, where it is fueled by the inflow of gas from the torques present in the bar region (Athanassoula, 1992; Wang et al., 2012; Cole et al., 2014; Baba & Kawata, 2020). Interactions are also known to be drivers of enhanced star formation in this manner (e.g. Patton et al. 2013; Pan et al. 2019), with the

interaction event itself driving inflows that help fuel central star formation (Torrey et al., 2012; Pettitt et al., 2016). As such, the combined effect of the bar evolution and the interaction provides an increase in fueling of the central regions in TideB and thus, the larger central star forming feature (Iles et al., 2022).

The bar is also a clear feature in these SFE maps, with pockets of intense star formation flaring along the bar and in clumps along the spiral arms. It is in fact, noteworthy that most of the star formation in TideB appears predominantly constrained to the structures, occurring almost exclusively within the bar and arm features in all barred time periods ($t' > 0$). In contrast, each of the IsoB maps in Figure 4.3 contain wide areas of strong star formation occurring all-throughout the disk. This star formation is neither associated with the central bar or any obvious arm feature indicating IsoB clearly shows greater inter-arm star formation, while TideB must concentrate gas more strongly into the arms and core, limiting star formation outside of these areas. This affirms the differences observed in the star forming history for the regionally averaged components of Figure 4.2 in the previous section, where the fraction of inter-arm star formation in IsoB was generally more than double that of TideB (Iles et al., 2022).

Additionally, it is possible to use Figure 4.3 to perform a preliminary assessment of the time dependency of SFR features in the evolution the two differently driven bars. The shape of the SFR projection in the bar region of each disk changes dramatically even over this relatively short duration ($\Delta t \sim 200\,\mathrm{Myr}$). The distinctly different star forming structures within the bars of IsoB and TideB, both form and evolve with varied attributes. For example, in the $t' = 200\,\mathrm{Myr}$ snapshot of the IsoB case, very clear arms comprised of star forming regions appear somewhat disconnected from the dense–almost triangular–central region within the bar. Comparatively, in the same period post-bar formation, the central region in TideB is also clumpy but this is mostly connected to the arms along a straight axis of star formation that spans the full bar length. This central axis is also accompanied by a thinner, curved envelope of similarly intense star formation which appears to encase the complete bar-axis from both above and below, seemingly connecting each arm to the other. Additionally, the bar in TideB at $t' = 100\,\mathrm{Myr}$ shows a wide, long clump along the bar-axis in the centre which tapers off toward the middle of the bar, before once again intensifying into a thicker bar at the end just before the arms connect. This is dissimilar to any of the other snapshots for either disk. These star forming structures vary broadly, even between evolutionary periods in a single simulated disk which make it difficult to produce any sweeping, general statements to describe definitive features. However, this difficulty itself supports the range of observations that indicate star formation

within even similarly barred galaxies appears to be consistently inconsistent (Iles et al., 2022).

4.2.2 The Kennicutt-Schmidt Relation

In order to compare the star formation properties of these simulated disks more analytically, as well to consider these results in relation to the gas availability, the so-called Kennicutt-Schmidt diagrams plotting a relationship between $\Sigma_{\rm SFR}$ and surface gas mass density ($\Sigma_{\rm gas}$) are a widely recognised analytic tool (Schmidt, 1959; Kennicutt, 1998). Figure 4.4 is a representation of this relation for the first 200 Myr of clearly barred periods ($t' = 100, 200$ Myr) for each of the two disks (IsoB and TideB). These are also compared with relations derived from observational studies in the literature.

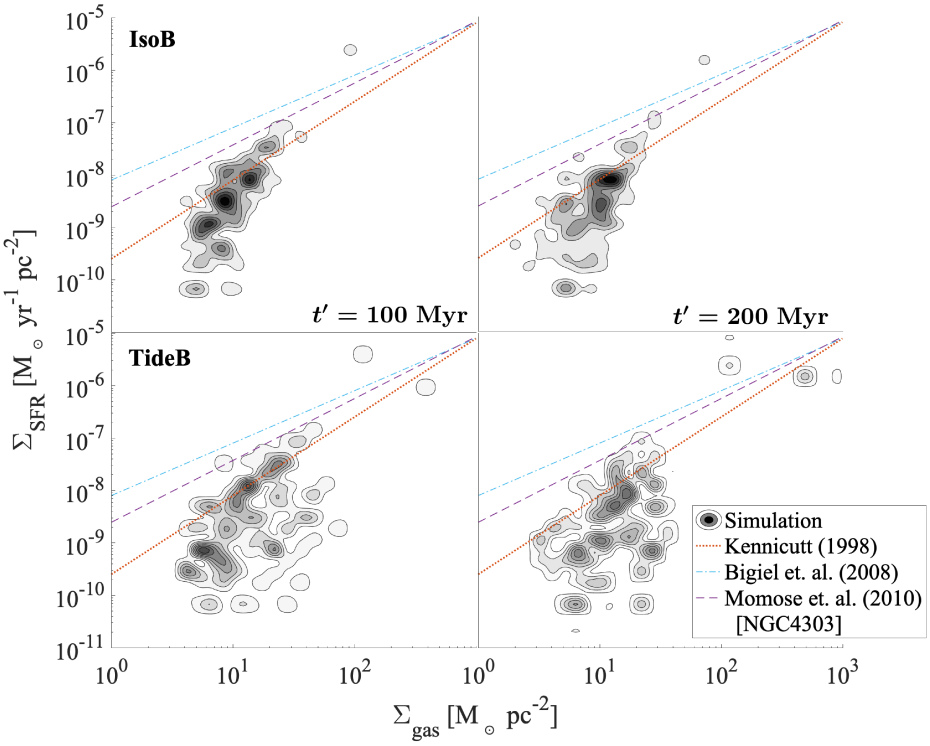

Figure 4.4: The Kennicutt-Schmidt relation between surface star formation rate ($\Sigma_{\rm SFR}$) and surface gas mass density ($\Sigma_{\rm gas}$) for both IsoB and TideB in periods immediately post-bar formation ($t' = 100, 200$ Myr). Surface densities are determined as in Figure 4.3 and smoothed with a spline interpolation. The literature relations: Kennicutt (1998) orange dotted line; Bigiel et al. (2008) cyan dot-dashed line; and Momose et al. (2010) purple dashed line–are shown for comparison (Iles et al., 2022).

The parameters represented in this figure are calculated to match the reso-

lution used in the previous section, ($\Sigma_{\rm SFR}$ derived by binning over a $0.1 \times 0.1\,$kpc grid), however, this can be considered a relatively high resolution compared to many historical observational studies. The simulated disk components are represented by contours with additional coloured lines to form an overlay of the following literature relations: Kennicutt (1998) in orange dotted; Bigiel et al. (2008) in cyan dot-dashed and Momose et al. (2010) in purple dashed. However, it is necessary to acknowledge that there may also be disk component variations between each of these previous studies, as well as with the simulated disk results, considering Kennicutt (1998) use disk averaged values for many galaxies; Momose et al. (2010) use only values from across NGC 4303; and Bigiel et al. (2008) constrain their measurements to be 'resolved' star formation in a sample of many galaxies in order to determine this relation (Iles et al., 2022).

Regardless of variations in the literature datasets, the shape of the distribution in Figure 4.4 is clearly different between the simulated disks with varying bar origins alone. IsoB gives rise to a narrow, arrowhead-like shape which seems to align relatively well in orientation with the literature results. Comparatively, the TideB shape is much broader along the $\Sigma_{\rm gas}$ axis making more circular distribution with less clear alignment. In TideB, there also appear many more components with high $\Sigma_{\rm gas}$ and low $\Sigma_{\rm SFR}$ in general. This indicates that TideB seems to have significantly more regions over the disk which are relatively inefficient at forming stars, but can maintain higher gas density. Both profiles exhibit clear evidence of evolution with time, in terms of the shape and location of this distribution within the $\Sigma_{\rm gas} - \Sigma_{\rm SFR}$ parameter space, and also in relation to the literature results. This is particularly evident in the area of Figure 4.4 which corresponds to low efficiency, high gas density features (around $\Sigma_{\rm gas} > 10\,{\rm M_\odot pc^{-2}}$ and $\Sigma_{\rm SFR} < 10^{-9}\,{\rm M_\odot pc^{-2} yr^{-1}}$) which seem to become more pronounced, spreading to higher gas densities for a given $\Sigma_{\rm SFR}$ value, as both disks evolve (Iles et al., 2022).

However, while the TideB distribution in Figure 4.4 shows many more such high $\Sigma_{\rm gas}$ and low $\Sigma_{\rm SFR}$ results than IsoB, the significant difference between the two cases in this region is conspicuously absent when these results are are deconstructed into components of the three morphological regions of bar, arm and inter-arm which is presented in Figure 4.5. This implies that many of these points were not classified as either bar, arm or inter-arm through the classification scheme, indicating the presence of some other component in TideB. As these contours trace star formation within the $10 \times 10\,$kpc field-of-view, these points must lie outside the $R > 10\,$kpc radial limit used in the region classification to define the extent of the optical disc. Such results must then be more likely attributed to star formation which is occurring in the high density gas which is being stripped to the very outer-edges of the disk or even

into the trailing tidal tail by the companion. This is further evidence that the largest changes occurring in TideB over time may still be mostly accredited to the direct result of the interaction affecting the outer-reaches of the galactic disk and beyond (Iles et al., 2022).

Additionally, it is worth noting that the definition of the disk limit may thus consequently have a significant impact on the shape of the KS relation for tidally-driven galaxies of all morphological types. In response to such a concern, slightly changing the prescribed outer radius for both disks has also been tested to find that the overall shape of the IsoB distribution is mostly unaffected while the TideB distribution is clearly sensitive to the change, as expected. This work has been predominantly concerned with the morphological features well-within the disk (i.e. bar, arms, inter-arms) which do not require deep consideration of the outer-disk so, such variance has not been taken further than this brief addendum. However, it is acknowledged that studies of stellar populations in the outer discs of galaxies or tidal features in interacting systems may find the existence of such sensitivity in results particularly relevant (Iles et al., 2022).

In comparison, Figure 4.5 also shows the Kennicutt-Schmidt relation for the two different bars of IsoB and TideB but with the single simulation component deconstructed into the previously defined morphological regions of bar, arm and inter-arm. For the purpose of producing this relation, the definition of morphological features is based on the (x, y) positions for the stellar component as determined previously. This does not take into account such features as arm offsets and assumes that the regions comprising of structure in both the gas and stellar components are spatially consistent. These are presented through scattered points, identifiable with the same symbols as in Figure 4.2 (bar–blue crosses; arms–filled red circles; inter-arm–magenta open circles). The Kennicutt (1998) relation is included again for reference as in Figure 4.4 represented here by a grey solid line. This allows for the determination of how each region contributes to the overall distribution, as well as for an assessment of how the star formation efficiency may differ from region to region. For example, in observations of NGC 4303, Momose et al. (2010) found the overall star formation efficiency to be higher than the average trend for all galaxies derived by Kennicutt (1998), particularly in the arm regions. That is not necessarily the case here, although a fraction of the arm results do appear to exhibit values higher than the Kennicutt (1998) relation (Iles et al., 2022).

The principal result in this figure that, in both disks, the bar very clearly reveals the steepest slope, consistently followed by the slope of the arm, and then the inter-arm regions. This is visually clearer for some panels than others, with the early IsoB data appearing to show similar slopes for the arm and bar. However, through direct calculation of these gradients, the consistency

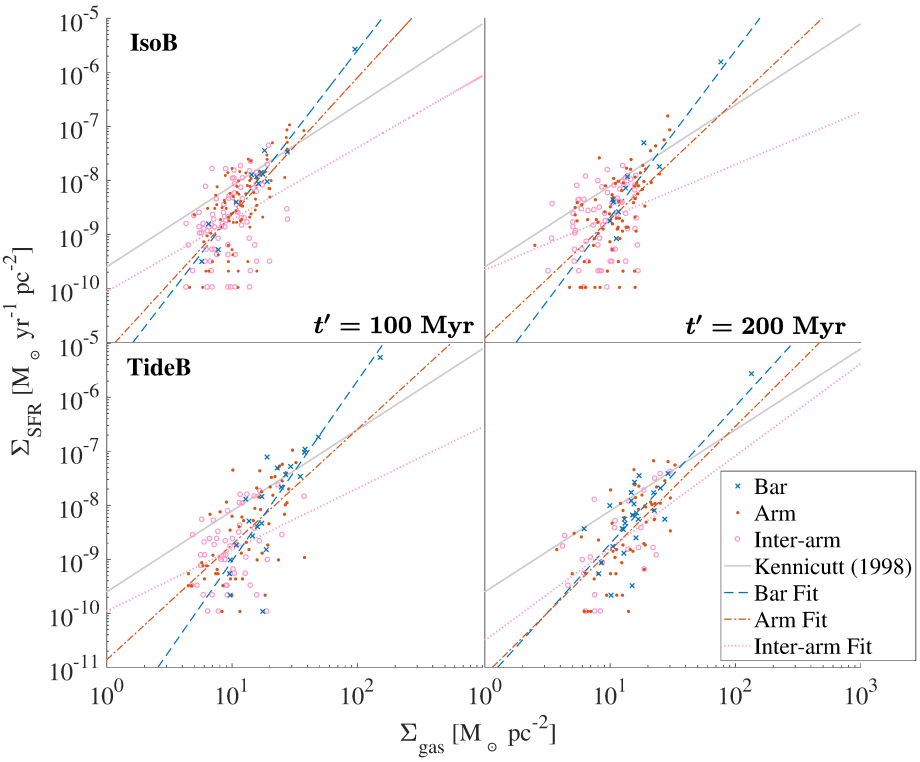

Figure 4.5: Kennicutt-Schmide relation by region with scattered data points showing the bar (blue crosses), arm (red filled circles) and inter-arm (magenta open circles) components. The line of Kennicutt (1998) is included for reference in grey, as well as power law fits for each region: bar – blue solid; arm – red dashed; and, inter-arm – magenta dot-dashed (Iles et al., 2022)

of the trend is obvious. The α coefficient for a power law fit of the form: $\log \Sigma_s = \alpha \log \Sigma_g + \beta$ for each region is displayed in Table 4.1, as well as a similar fit for the total distribution over the disk ($R < 10\,\mathrm{kpc}$). Considering these coefficients as an analogue for the linear gradient in the log-log space of Figure 4.5, it can be directly confirmed that the bar region in both disks has unmistakably produced a significantly steeper relation than the arms, inter-arm or even total distribution on average (Iles et al., 2022).

The outlying point with highest Σ_{SFR} and Σ_{gas} in Figure 4.5 also appears to be always a member of the bar component. In fact, this is the result from the centre-most region, which is often defined in some studies as a fourth morphological feature (a central nucleus) and, in this capacity, considered separately from the properties of the bar. For the following analysis, care has been taken to test both including and excluding this point in assessing the bar response. The results included in Table 4.1 are for fits including the nucleus within the barred region and excluding star formation at and beyond the defined disk

Table 4.1: Gradient coefficients for a power law fit to the previous $\Sigma_{\rm gas}$ vs. $\Sigma_{\rm SFR}$ data for the disk region of interest ($R < 10\,\mathrm{kpc}$). This fit follows the form $\log \Sigma_s = \alpha \log \Sigma_g + \beta$, the α coefficient is listed.

Model $- t'$	**All**	**Bar**	**Arm**	**Inter-arm**
IsoB-100 Myr	2.7 ± 0.4	3.0 ± 0.5	2.5 ± 0.6	1.3 ± 0.8
IsoB-200 Myr	2.3 ± 0.4	3.1 ± 0.7	2.2 ± 0.7	1.0 ± 0.8
TideB-100 Myr	2.5 ± 0.4	3.0 ± 0.9	2.4 ± 0.7	1.6 ± 0.9
TideB-200 Myr	2.4 ± 0.5	3.2 ± 0.8	2.4 ± 0.7	1.7 ± 1.1

limit of 10 kpc. However, the addition of the nucleus has been determined to make negligible change to the result of the bar slope, as without this extremely high value this still remains significantly steeper than all other results. The addition of tidal remnants in the total average (without the radial constraint $R < 10\,\mathrm{kpc}$), however, saturates the overall fit to be more consistent with the flatter inter-arm component rather than the arms. This is expected as the amount of star formation in the arms spatially dominates the total star formation within the mid-disk, particularly in TideB, whereas, the conditions in the outer-edges of the disk are more consistent with the inter-arm space (see, for example, Figure 4.3). Hence, when these outer regions are included, the influence of the arms on the total average must be decreased (Iles et al., 2022).

In comparing these results with related observational studies that consider the disk morphology with the SFR, it is possible to see that the range of results is relatively similar. In the case of the isolated target, Momose et al. (2010) also find a similar arrowhead shape for the Kennicutt-Schmidt diagram of values observed from NGC4303, however it is possible to see from Figure 4.4 that the alignment of the distribution is steeper overall than the relation observed by Momose et al. (2010) with the IsoB result showing consistently lower values for star formation in the low gas region of the plot, causing a steeper alignment of the arrow shape overall. Additionally, when considering the morphological components, observational results appear to indicate a preference for a significant portion of the arm component to have distinctly higher SFE than the other regions; with arm values independently occupying the top arrow-edge and exhibiting a wider spread of values to higher SFR for a given gas value than any other component. The bar population is similarly shown to have lower SFR than either the arm or inter-arm component for higher gas surface densities. Such obvious spatially-separable features are not necessarily evident in the results for IsoB. Firstly, the arm and inter-arm appear distinctly indistinguishable and, secondly, while the arm and inter-arm regions show higher SFR than the bar for similar gas density, these components simultaneously also exhibit lower values for the same gas density (Iles et al., 2022).

In the IsoB results, the bar component also forms a thin distribution al-

most bisecting the larger spread of the other regions. Comparatively, the bar response in TideB is more dispersed throughout the distribution, particularly in the second 100 Myr post-bar formation ($t' = 200$ Myr). This is in line with the results of Watanabe et al. (2011) where the region of the KS plot occupied by bar results is also predominantly interspersed with the other regions. However, it is important to note that Watanabe et al. (2011) do not specifically define a separate arm and inter-arm region in their sample, leaving these populations somewhat ambiguously defined as 'Other (mostly arms)'. There is also a difference in the definition of the bar as Watanabe et al. (2011) define both a bar region plus a separate classification for the bar-ends, differentiating these from the bar as a whole. This is a further distinction to the structural features in the central region of barred-disks that neither Momose et al. (2010) nor this work have elected to employ. It is very likely that the difference between these classification schemes may have introduced a certain level of ambiguity into the possible comparison between studies of regionally dependent trends in star formation (Iles et al., 2022).

In addition, Onodera et al. (2010) have shown that resolution in observational studies can have a non-trivial affect on the shape and orientation of the Kennicutt-Schmidt relation even within a single target galaxy. By nature, simulation studies can achieve a significantly higher resolution than most observational results. Even within simulations, Fujimoto et al. (2014) for example, have shown that this relation is sensitive to the star formation models used to prescribe the physics of the simulation. The differences are particularly evident when considering the relation of regionally dependent components with a standard star formation recipe as prescribed by mass and free-fall time constraints, GMC turbulence as per Krumholz & McKee (2005) and cloud-cloud collision as per Tan (2000). Each of these has been found to produce a different orientation of the same bar, arm and inter-arm regions in $\Sigma_{\rm gas}$–$\Sigma_{\rm SFR}$ parameter space (Fujimoto et al., 2014). The results presented herein are likely not immune to such constraints. The IsoB results displayed in Figure 4.5 appear similar to the standard response in Fujimoto et al. (2014)–unsurprising considering the star formation recipe used in this simulation–whereas, the observational results of Momose et al. (2010) appear to be more similar to the cloud-cloud collision result from the same study. It is perhaps unavoidable that some discrepancies must arise between these simulated results and the observational results of the target galaxies due to either or both the inherent resolution and star formation conditions, as well as the region classification method which is commonly inconsistent between previous studies in the literature (Iles et al., 2022).

4.2.3 Comparing Region-Averaged Values

To attempt to circumvent any inconsistencies arising from the resolution of the Kennicutt-Schmidt diagram, the mean values for $\Sigma_{\rm SFR}$ and $\Sigma_{\rm gas}$ for each region have also been calculated and subjected to analysis and comparison with observational results for NGC 4303 and NGC 3627. The corresponding values also evidently decrease from bar to arm to inter-arm in a manner which is consistent with the distinct flattening of the slope for the $\Sigma_{\rm gas}$–$\Sigma_{\rm SFR}$ relation (as in Figure 4.5, Table 4.1). This is true in all time periods for both disks. The gas means also reflect decreasing values per region in order of bar – arm – inter-arm but the magnitude of the difference between each region is less in the gas surface density than the star formation. These mean values for each of the defined regions are shown in Table 4.2 for each IsoB and TideB (Iles et al., 2022).

In this classification, the high $\Sigma_{\rm SFR}$, high $\Sigma_{\rm gas}$ outlying point attributed to the central nucleus remains included within the bar component. If this component is removed and the averages are instead calculated as four regions, it can be seen that this nucleus saturates the response of the bar. Hence, Table 4.2 presents the original bar component with nucleus as Bar and the bar without the centre-most region as Bar (/cen.). Then, the Centre component is exactly this point which has been removed from the original bar component. Of the four regions, the nucleus is naturally the highest by two orders of magnitude, however, the bar without centre still produces a value considerably higher than the corresponding arm region which is in turn greater than the mean inter-arm values. This is also consistent with the related analysis of simulated disks by Fujimoto et al. (2014) who similarly find in the disk decomposed by region that the average of bar values are generally higher than the average arm region and then the inter-arm region with varying degrees of separation depending on the star formation model implemented (Iles et al., 2022).

Table 4.2: Mean values of gas and star formation surface density in morphologically distinct regions in each model (Iles et al., 2022).

Region	$\bar{\Sigma}_{\rm gas}$ [$M_\odot pc^{-2}$]		$\bar{\Sigma}_{\rm SFR}$ [$10^{-2} M_\odot yr^{-1} pc^{-2}$]	
	IsoB	**TideB**	**IsoB**	**TideB**
Arm	12.9 ± 0.6	15.3 ± 0.2	1.01 ± 0.1	1.14 ± 0.3
Bar	20.1 ± 1.1	23.6 ± 5.4	16.2 ± 5.8	19.6 ± 12
Centre	86.1 ± 14	143 ± 13	212 ± 79	410 ± 193
Bar (/cen.)	15.0 ± 0.1	18.4 ± 4.3	1.13 ± 0.1	2.17 ± 1.7
Inter-arm	10.0 ± 0.5	12.0 ± 1.4	0.42 ± 0.1	0.56 ± 0.3

Comparing these results to observationally determined values for the average SFR surface density, as calculated by Yajima et al. (2019) for NGC 4303

and Watanabe et al. (2011) for NGC 3627, indicates that $\Sigma_{\rm SFR}$ for the main features of bar (not including the central nucleus) and the arms are at least of a similar order. The simulation values are all slightly lower than the observational counterparts for each region. Comparing the relative values between the two main morphological regions, Yajima et al. (2019) find that the arms in NGC 4303 have a higher $\Sigma_{\rm SFR}$ than the bar by $\sim$2%. For NGC 3627, Watanabe et al. (2011) indicate that the bar should have $\sim$4% higher $\Sigma_{\rm SFR}$ than the other region (classified as 'mostly arms' which should also include an inter-arm component). This is a very small difference between the two regions in observations of both targets. However, both these studies define and calculated $\Sigma_{\rm SFR}$ while separating the bar-ends to a 3rd significant region which has significantly higher value than either the arms or bar. In this work, as the the bar-ends were not specifically separated and it is uncertain which component (bar or arms) that the results for the classification of this 3rd region has been drawn from, it is difficult to confidently compare with these observational results (Iles et al., 2022).

Assuming the bar and bar-ends together make a complete bar component, averaging the bar and bar end results from observations (Watanabe et al., 2011; Yajima et al., 2019) instead indicates the bar+bar end component of NGC 4303 should have a $\Sigma_{\rm SFR} \sim 27\%$ more than the arms, whereas this is $\sim$71% for NGC 3627 with the bar+bar end component being higher than the arms in both cases. This resolves the difference between the IsoB simulation showing lower star formation in the bar rather than the higher star formation rates in the arms than the bar of NGC 4303 (Momose et al., 2010; Yajima et al., 2019). The simulation results also show a significantly greater difference between the bar and arm components in TideB than IsoB, similar to the corresponding targets, although the calculated values are also lower than observations in this respect. IsoB has the Bar (/cen.) greater the arm by 11%, while TideB has a difference of 47% between these two regions. However, as mentioned previously, the spatial definition of regions is often inconsistent between studies (both observational and theoretical) and this inconsistency can give rise to significant differences in the trends observed. So, it is considered pertinent to develop some means to quantify how star formation properties may differ spatially throughout the bar and disk of these galaxies in a manner which is independent of a specific classification for each morphological region (Iles et al., 2022).

4.3 Radial Dependence of SFE

In an effort to further identify and classify any sub-kpc star formation features and trends evident in these two differently formed barred-disks, the analysis of star formation properties across the existing disk structures is adapted to follow a directional approach. Here, existing variations in star formation efficiency are considered for any radial dependence as each IsoB and TideB independently evolve. The star formation efficiency is specifically used as a metric in order to account for the interrelation between gas availability and star formation activity, with SFE $= \Sigma_{\rm SFR}/\Sigma_{\rm gas}$ [Myr^{-1}] by definition.

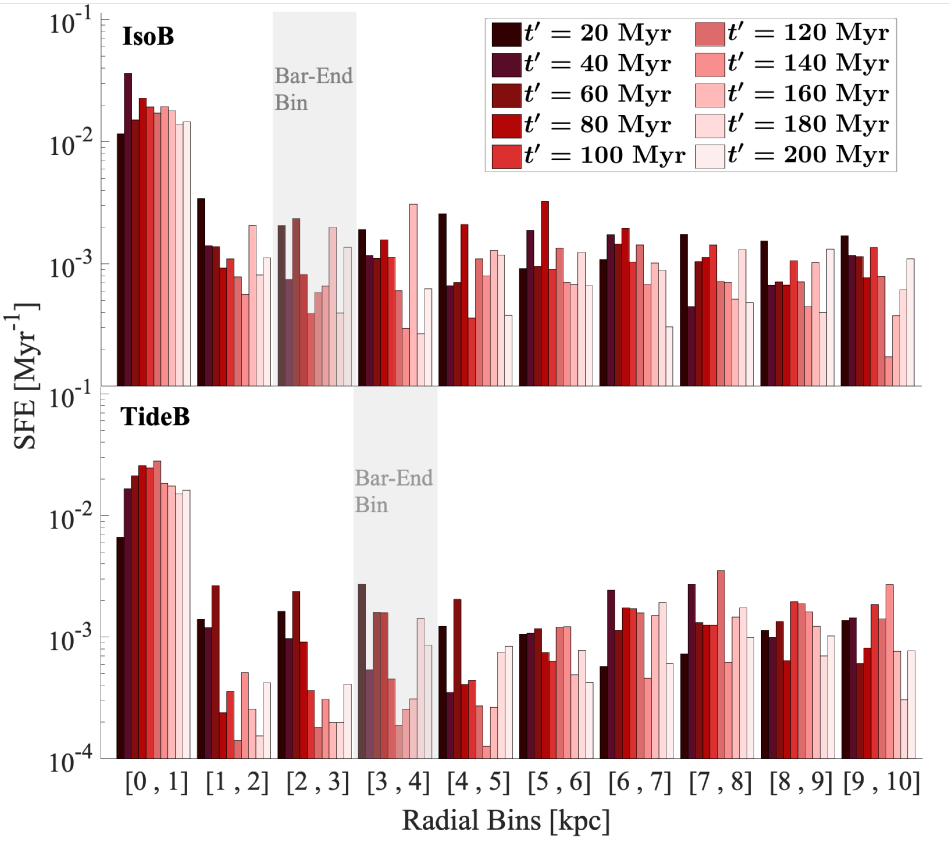

Figure 4.6: Azimuthally averaged SFE with radius for IsoB and TideB. The SFE across the disk is binned radially in steps of 1 kpc for the period immediately post-bar formation ($0 < t' < 200$). For each radial bin, the time evolution of SFE is tracked by colour saturation with each bar corresponding to the result at every 20 Myr. Dark to light indicates forward time progression. The bin in which the bar extent would be located is shaded in grey (Iles et al., 2022).

The radial dependence of SFE across both the IsoB and TideB disks is presented in Figure 4.6. In this figure, the radial bins are defined with a width of $\Delta R = 1$ kpc where the SFR and gas mass are averaged over each radial

annuli in order to calculate an SFE value for each bin. These are determined for every 10 Myr of the 200 Myr immediately post-bar formation ($t' = 0 - 200$ Myr) in each disk. A consistent star formation look-back time of $\Delta t_{\rm SF} = 10$ Myr is maintained with the star formation analysis in previous sections. The colour saturation indicates time evolution: colours evolving from dark to light corresponds to an increasing value of t'. The background to the radial bin which should contain the bar-extent is also shaded in grey for ease of recognition (Iles et al., 2022).

The centre-most bin in this figure can be seen to produce the highest value of SFE for all times in both disks, as may be expected from the existence of the high star forming central nucleus identified in in previous sections (see for example: Figures 4.3, 4.4 & 4.5). Other than this feature, there does not appear to be any immediately obvious or consistent trend within a given bin, as the SFE varies with time for either disk. These values neither continuously grow, decline, nor oscillate in any discernible pattern. However, if considering the broader response as SFE changes with radius across all bins, a trend is perhaps observable. Outside of the central bin, the average level of SFE in the disk of IsoB appears to be remain mostly constant, whereas TideB appears to follow a more increasing or sinusoidal shape with radius; showing lower SFE towards the centre ($\sim R_{\rm bar} \pm 2$ kpc) and higher SFE towards the outer-edge. This may be evidence that the interaction has caused the inner regions to suffer a depletion of gas compared to the relatively more stable conditions in the outer-disk. However, these broad trends are not necessarily true at all times, as the inner deficit is clearly not prevalent initially at $\sim t' < 80$ Myr (Iles et al., 2022).

The gradient of a linear fit to the SFE bin height is, therefore, employed to further constrain these possible trends in the evolution of the radial dependence of SFE. To determine this gradient, a linear least-squares fit was applied for all histogram bins excluding the centre-most bin with $R < 1$ kpc in Figure 4.6. The first coefficient of this fit is plotted in Figure 4.7 for each step of 10 Myr to illustrate the evolution of any possible trends. In this way, a positive result would indicate that the SFE increases overall with radius and, conversely, a negative result is evidence of a decreasing SFE with radius. In this figure, the blue squares correspond to the calculated IsoB gradients, whereas TideB is denoted by orange triangles (Iles et al., 2022).

It is plainly evident that there is significant variation in the radial dependence of SFE in the period immediately post-bar formation for both disks. During the first 50-100 Myr after bar formation, the trend for each case appears similar: a steep negative gradient steadily begins to flatten and oscillate around zero, indicating the average SFE across the disk is generally constant at that time. However, while the gradient of SFE in IsoB appears to remain

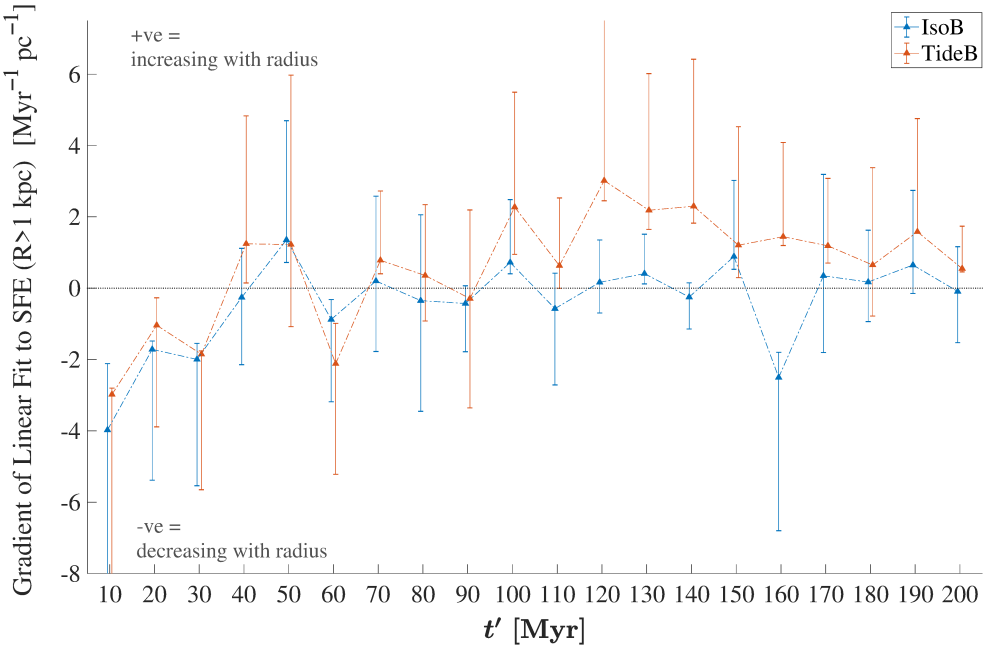

Figure 4.7: The time evolution of the SFE(R) gradient as determined by linear fit to the bins from Figure 4.6 plotted with t' time. For these fits, the prevalent central bin containing contributions from the intensely star forming nucleus region is excluded. The calculated gradient is marked by a blue square for IsoB and an orange triangle for TideB. A positive value indicates the overall SFE increases with radius while a negative value indicates a decreasing SFE with radius (Iles et al., 2022).

within $\pm 1\,\mathrm{Myr}^{-1}\mathrm{kpc}^{-1}$ of zero (i.e. flat), the TideB gradient continues to climb in value, transitioning through zero to develop a clearly positive gradient for the duration of the second 100 Myr post-bar formation and thus, a decreasing depletion time increasing with radius. In the last 50 Myr of the period considered, the TideB gradient does reduce somewhat to values which are possibly comparable to the steepest positive extent of the IsoB gradients, however, it is unclear whether the two cases will eventually equalise. There is also one period of in the latter epoch of IsoB which is noticeably inconsistent with all other values for this disk. At $t' = 160$ Myr in IsoB, the gradient is almost the steepest negative result plotted for either disk. It is unclear from the current analysis what kind of event may have caused such a strongly declining profile of SFE in just this brief 10 Myr time period. However, subsequent analysis of the bar region specifically also indicates that there is an uncommonly high value of SFE across the full length of the bar for this particular time period (see Figure 4.9 in Section 4.4 for $t' = 160$ Myr). Although, this evidence can only be considered an illustration of the direct mathematical cause for this strongly

declining gradient in Figure 4.7 and, as yet, does not provide an account for the physical origin of the event (Iles et al., 2022).

The general results presented in Figure 4.6 and Figure 4.7, however, are found to be broadly consistent with the observed SFE trends in galaxies. In this respect, the TideB response is somewhat significant. Leroy et al. (2008) measure the radial changes of SFE in the THINGS dataset (Walter et al., 2008) and observe that most galaxies appear to exhibit an SFE response that tends to either maintain a constant value or decay with increasing radius. There are some systems however, such as NGC 5194 (M51) and NGC 3627 (the observational target for TideB), which conversely appear to display localised regions with radially increasing SFE in the disk (Leroy et al., 2008). This result has also been confirmed by Muraoka et al. (2019) with the COMING observational survey dataset (Sorai et al., 2019). While NGC 3627 appears to exhibit a generally constant SFE across the radii measured, a slightly increasing trend is clearly able to be observed at outer radii. M51 was not included in Muraoka et al. (2019) but the isolated target (NGC 4303) was. Comparatively, NGC 4303 shows a more consistently flat profile with smaller scale radial fluctuations in SFE across the disk (Muraoka et al., 2019). This observed SFE behaviour for NGC 4303 is indeed similar to the IsoB result reflected in Figure 4.7–primarily constant with only slight variation in both directions over time (Iles et al., 2022).

M51 is widely accepted to be an interacting galaxy (Leroy et al., 2008; Buta, 2019; Colbert et al., 2004; Karachentsev et al., 2013); NGC 3627 was specifically chosen as a target for this work due to the likely rich interaction history; and, TideB is by design driven by an interaction. This may suggest that the characteristic of a positive SFE gradient toward outer radii is indicative of an ongoing, or at least recent, interaction. If this is the case, it would mean that an increasing SFE with radius may be used as a possible metric to identify tidally-driven galaxies from the star forming features of the stellar disk. The relatively constant or negative gradients–which dominate the IsoB result and earlier periods of TideB–can then also be considered compatible with more commonly observed trends, as instances where this may be observed for either IsoB or TideB over the duration of the simulation would indeed make it appear most common (Iles et al., 2022).

4.4 Dependence of SFE within the Bar

Whether star formation should also vary along the primary axis within the bar itself has also been a long contested topic in the literature (e.g. Roberts et al., 1979). Many studies have asserted that the SFE in barred-galaxies

appears to be consistently lower in the bar than in the associated spiral-arm features of the disk (Momose et al., 2010; Hirota et al., 2014; Yajima et al., 2019). Comparatively, others have further indicated that SFE may even vary completely across the full length of the bar (Downes et al., 1996; Sheth et al., 2002; Muraoka et al., 2019). Additionally, studies of the target NGC 3627 state that in this galaxy, there appears to be unexpectedly higher SFE at the bar-ends and very centre (circumnuclear region) than elsewhere in either the bar or disk features (Watanabe et al., 2011; Law et al., 2018). Hence, in addition to the radial dependence of SFE across the disk presented in the previous section, a similar directional analysis has been applied to the bar radii specifically in order to provide more detail in this area.

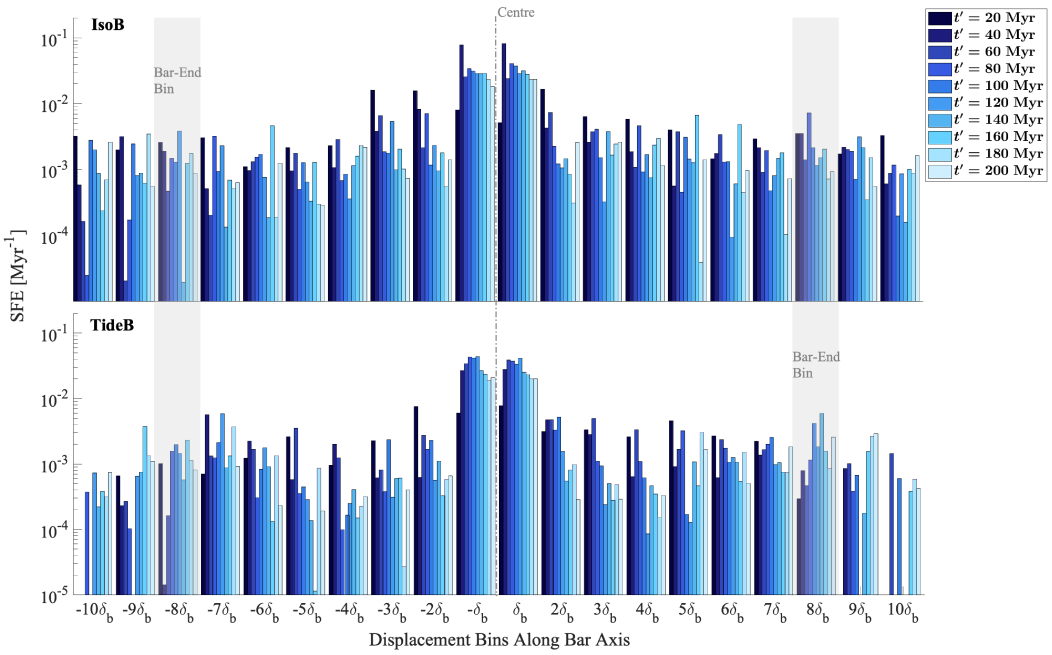

Figure 4.8: Azimuthally averaged SFE along the bar-axis for IsoB and TideB for the period immediately post-bar formation ($0 < t' < 200$). The bar-axis is defined by a co-rotating co-ordinate system to always align with the x-axis and the bar width is set to $y \pm 1$ kpc. As bar-length differs for each disk, a consistent number of bins is used creating a fractional bar element (δ_b). These are numbered outwards from the centre. The time evolution of SFE is mapped via colour saturation with evolution from dark to light and bars at every 20 Myr. Again, the bin containing the bar extent is shaded in grey (Iles et al., 2022).

A similar histogram of SFE variation with radius is displayed in Figure 4.8, however, this figure serves to specifically highlight any trends prevailing within the bar limits or where the edges join to the spiral arm structure via a binning along the bar-axis, in particular. For this analysis, the bar region is

considered to be a solid body rotating about the major axis, as bar slow-down tends to occur on much longer time-scales than this period of interest (Miwa & Noguchi, 1998; Debattista & Sellwood, 2000; Kormendy, 2013). The bar orientation is detected by identifying density peaks in the stellar population within the previously determined bar radius. This orientation vector can then be used to transform the positions of all simulation stars and gas into a co-rotating co-ordinate system where the bar is always aligned the $x-$axis in the xy-plane. To account for variation in total bar length between disks (and time periods), the bar is subdivided into bins with widths encompassing a set fraction of the bar-extent rather than a constant value in kpc. These are, by definition, dimensionless fractional bar elements (δ_b) and are numbered outwards from the centre-most bin to the radial limit of bar plus an additional two extra bins to ensure the possible bar-end regions of previous studies are fully encompassed. The SFE for each bin is then calculated for a rectangular polygon cut-out running parallel to this axis with a y-axis height of 2 kpc determined to span the bar minor axis (Iles et al., 2022).

As in Figure 4.6, the star formation time is $\Delta t_{\rm SF} = 10\,{\rm Myr}$ and the time evolution is mapped by saturation coloured bars which represent the SFE conditions in the bar at every second step of 10 Myr (i.e. for time periods every 20 Myr) evolving from dark to light. The background for the bin which should contain the value calculated for the bar-extent is similarly shaded in grey. In this figure, the primary focus is directed at two key features: symmetry about $x = 0$ to consider whether star formation is symmetrical along the bar; and, significant peaks or troughs in SFE at key regions (i.e. at the bar-ends) to assess whether there is any identifiable trend in the SFE(x) profile along the bar-axis. Interestingly, the SFE profile along the bar does not seem particularly symmetrical in either disk for any of the time periods represented by Figure 4.8. However, there is also neither a tendency towards consistently asymmetric responses or values skewed to one particular direction. Similar to the radial dependence over the full disk (see Figure 4.6), there also appears to be no standard trend for this SFE along the bar changing and evolving with time (Iles et al., 2022).

In the case of IsoB, at earlier times the SFE seems to decrease steeply toward the bar-ends ($t' < 100\,{\rm Myr}$). In the period after $t' = 100\,{\rm Myr}$, the SFE values for each bin appear variable along the bar-axis on the small-scale but are generally constant on average. Comparatively, the SFE in the earliest periods of bar formation in TideB appears to be predominantly decreasing steeply towards the bar-ends. After $t' \sim 60\,{\rm Myr}$, however, this changes and the SFE appears to lessen in the middle areas of the bar ($2\delta_{\rm b} \lesssim |x| \lesssim 5\delta_{\rm b}$) before rising towards the bar edges. This is consistent with the previous section where a significant change in the SFE gradient with radius in TideB could be observed

at almost exactly this time period as in Figures 4.6 & 4.7 with lower SFE in the inner region compared to the outer radii (Iles et al., 2022).

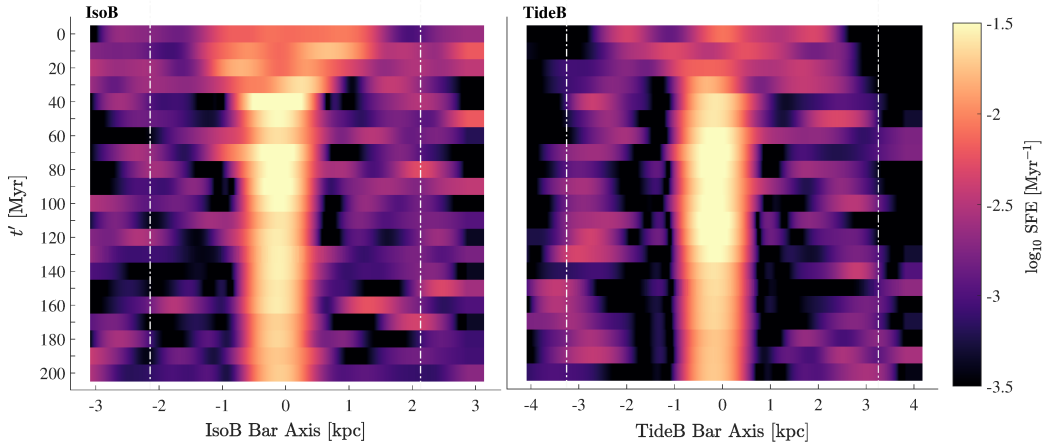

Figure 4.9: The time evolution of SFE along the bar-axis from Figure 4.8 is re-oriented as a heat-map for SFE smoothed by a spline interpolant. Each resolved t' corresponds to a strip of intensities along the x-axis representing the SFE values in each bar element. Time evolution is downward along the y-axis. The colour weighting is such that brightest areas correspond to high efficiency and dark values to low efficiency. The bright central band corresponds to the nuclear disc, and the white dot-dashed lines illustrate the previously defined bar length (Iles et al., 2022).

To further quantify this variation of SFE along the bar, Figure 4.8 can be re-oriented as a heat-map representing the development of SFE along the bar-axis. This is presented in Figure 4.9. In this figure, the SFE values for each time are smoothed by fitting a spline interpolant and then plotted along a strip of bar-axis values in kpc for each case. The time evolution is defined to be downward along the y-axis of this figure and the result is calculated for each step of 10 Myr. Visually, both disks exhibit an obvious trend of peak SFE in the centre-most region, as expected. While the presence of this peak is ubiquitous in the evolution of both disks, it does appear brightest in the early period of the bar before beginning to decline in intensity slowly but steadily as both bars continue to evolve. Alongside this bright peak of a central feature, IsoB does not appear to conform to any other consistent trends over the evolution of this bar region. However, TideB quickly appears to evolve into a pattern of strong SFE at the bar-ends (delineated by white vertical dashed lines) and low SFE at approximately half the bar radius framing the strongest central peak. Such a pattern is replicated at some time periods during the IsoB disk evolution, but this appears more of a serendipitous occurrence as a part of the almost random variations which appear to fluctuate along the length of the

bar in this disk (Iles et al., 2022).

Studies of the interacting target (NGC 3627) consistently appear to find that observations indicate this galaxy has higher SFE at the bar-ends and centre compared to other parts of the bar (Watanabe et al., 2011; Law et al., 2018). This is exactly the pattern of SFE which is reproduced in the TideB bar for most periods of the simulation. In comparison, studies of the isolated target (NGC 4303) more commonly report more average values for SFE along the bar (Momose et al., 2010), although Yajima et al. (2019) also specifically investigate the bar-ends to also find higher results in this region than either the bar or arm components they identified. From Figure 4.9 it can be seen that the SFE patterns across the bar of IsoB (related to NGC 4303) are much more likely to appear as featureless on average, although it is certainly possible to observe higher SFE at the bar-ends than the surrounding areas if observing at a given time period of the evolution. In this case, it seems that both the resolution and the specific epoch of the disk's evolution which is observed may cause the star forming features recorded across the length of the bar to vary significantly for a bar formed in isolation, such as IsoB and likely NGC 4303. Comparatively, as there is such a consistent trend developed and maintained, it is possible to assume that similar observations for tidally-driven barred-disks should more directly be able to resolve these features, as in NGC 3627 (Iles et al., 2022).

Additionally, such a distinct pattern in the SFE implies there must be some active physical effect which is particularly dominating in TideB but may also occur to a lesser extent in IsoB in order to produce such a feature in the bars of each disk. Variation in the SFE within the bar regions of galaxies has previously been attributed to possible non-circular motions generating strong shocks or shear motions along the bar disrupting many bar-located molecular clouds (Schinnerer et al., 2002; Dobbs et al., 2014). It is certainly true that the non-axisymmetric motions are significantly higher in the TideB disk (see Figure 3.6), however, these stronger motions are also evident across the entire disk and not just concentrated about the central bar region. Law et al. (2018) suppose a possible correlation between the kinetic temperature and SFE in NGC 3627 (TideB target), which may also be relevant in this case. Conversely, Beuther et al. (2018) assert that the surface densities of NGC 3627 are too high for shear to be sufficient to effectively dampen star formation activity at the bar-ends, and that differing pattern speeds between the bar and arms should be the most favourable condition to promote the observed regions of intense star formation in the structure of this galaxy (Iles et al., 2022).

The arms in TideB are frequently observed to decouple from the bar-ends and reconnect over time, significantly more-so than the arms in the IsoB disk. Figure 4.10 is a magnified view of the TideB gas in the central region before

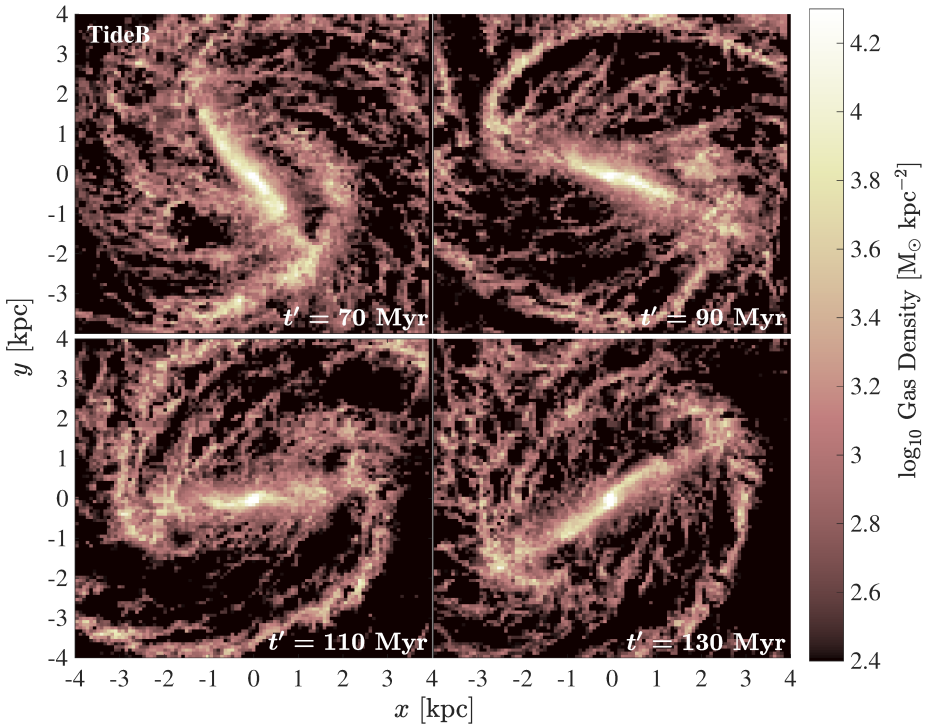

Figure 4.10: A projection of face-on gas density in the central region of TideB, zoom-in to highlight the bar-spiral overlap regions. Two time steps equally spaced either side of $t' = 100\,\mathrm{Myr}$ (Iles et al., 2022).

and after $t' = 100\,\mathrm{Myr}$. This serves as an illustration of the decoupling process occurring during the 200 Myr period of interest post-bar formation. In this figure, arch-like arm features bracket the bar-ends, highlighting their decoupling from each end before rejoining; a time-dependent process which appears to occur frequently over orbital time-scales. Calculating the pattern speed for both the bar and arms, it is possible to determine that there is a difference in rotation speed at radii about the bar end. The bar pattern speed was determined by tracking the angular displacement of the defined bar-axis at the given radius R_{bar} over the duration of interest $t' > 0$ which is in line with standard methods for resolving transient features (Grand et al., 2013; Pettitt et al., 2017). Throughout the relatively short period of interest the bar pattern speed in the TideB disk does not significantly vary with a value of $\Omega_{\mathrm{bar}} = 25.9\,\mathrm{km\,s^{-1}\,kpc^{-1}}$. If the arm pattern speed is considered to be dynamic, transient and tidally-driven, it is reasonable to assume an arm pattern speed of $\Omega_{\mathrm{sp}} = \Omega(\mathrm{disc}) - \kappa/2$ in line with Pettitt et al. (2016). At the bar-end R_{bar}, this radially dependent pattern speed is found to be $\Omega_{\mathrm{sp}} = 41.9\,\mathrm{km\,s^{-1}\,kpc^{-1}}$ which is significantly greater than the bar speed and thus, further evidence of the decoupling between these two morphological features (Iles et al., 2022).

The continued influence of the companion, is alternatively another possible driver for this pattern of peaked SFE at the bar-ends becoming a lasting feature of the tidally-driven disk. It is possible for the sustained torques from the interaction to impact the development of gas-flow and subsequent star formation within the disk structure. Under this kind of driven bar formation, the interaction generates a large inflow toward the centre of the galaxy, causing increased star formation in the entire central region, prompting the initial starburst. However, over time the available matter in these areas may become insufficient to support the same amount of star formation after the initial inflow amount is converted. Casasola et al. (2011) postulate that the bar-end of NGC 3627 may be aligned with co-rotation and that the absence of an inner Lindblad resonance (ILR) means the torques are negative between the bar and the nucleus in this disk. In such a state, NGC 3627 can be considered a so-called 'smoking gun' of inner gas inflow, wherein the dynamical resonances and kinematically decoupled inner bar serve to directly supply gas to the central region and AGN (Casasola et al., 2011). Although Casasola et al. (2011) note that this process should be unsustainable after the bar has had time to slow under secular evolution, the bar pattern speed of TideB does not significantly slow over the relatively short duration of this analysis period, so discernible traces should still be evident. However, calculating the co-rotation radius for the TideB disk gives a radius $R_{\mathrm{CR}} = 4.97\,\mathrm{kpc}$ which is not especially close to the determined bar extent ($R_{\mathrm{bar}} = 3.12\,\mathrm{kpc}$). Therefore, dynamical resonances directly supplying the inner region with gas in this way appears unlikely. Additionally, such an explanation does not necessarily account for why there should remain only preferentially strong star formation at the bar-ends in the central region (Iles et al., 2022).

For now, the direct physical mechanism driving this feature to form preferentially in tidally-driven bars rather than systems of isolated bar evolution remains unclear. However, such differences in the regionally dependent SFE profile of these bars should make a fitting metric to determine the formation history of any given barred-galaxy. However, while the difference between persistent evolutionary trends and a transient feature may be directly distinguishable in simulated results such as these, it is not so straightforward to achieve with the observations of real galaxies. If this is to be possible, it is necessary for the ambiguity of such briefly occurring SFE features in the isolated disks to be resolved. A feat which is perhaps achievable by tracing and constraining the development of stars formed in these regions post-formation.

Chapter 5

Stellar Motion in Isolated and Tidally-Driven Bars

The following comprises a brief description of an explorative foray into the dynamical evolution of stars formed in the three disks: IsoB, TideB and TideNC. This analysis aims to identify trends in the stellar population mixing with positions, momenta and stellar orbital information over the complete 1 Gyr integration time. This should also facilitate a preliminary assessment of whether such features are sufficiently sensitive to differing bar origins to affect lasting change to the observable attributes of similar resolved galaxies.

5.1 Total Variation over the Simulation

Radial migration is traditionally quantified by the changes in either or both radial position (r) and orbital angular momentum in the disk plane (L_z), which also allows for a distinction between the two processes of blurring and churning thought to drive such changes (e.g. Sellwood & Binney, 2002; Halle et al., 2015). Additionally, it has been argued that a consideration of vertical motion perpendicular to the disk plane is not without influence in studies of stellar population mixing, particularly in relation to the formation of distinct thick and thin disk structures (e.g. Navarro et al., 2018; Mikkola et al., 2020). Whether these simulations are sufficiently able to produce and resolve such structure is unknown as this was not the intention when the initial conditions were derived. Regardless, a third dynamical variable, the position (z) above or below the disk plane is also considered in the following analysis for completeness. These attributes are primarily considered for all stars formed during the evolution of the IsoB, TideB and TideNC disks. While the oldest stars, those set by the initial condition, also naturally influence the dynamics of the system and are in turn influenced by the system, these have been omitted for

convenience (unless otherwise specified). This is simply a practical decision as the motivation for such analysis stems from relating disk structural features with effects on the associated star formation and stellar motion.

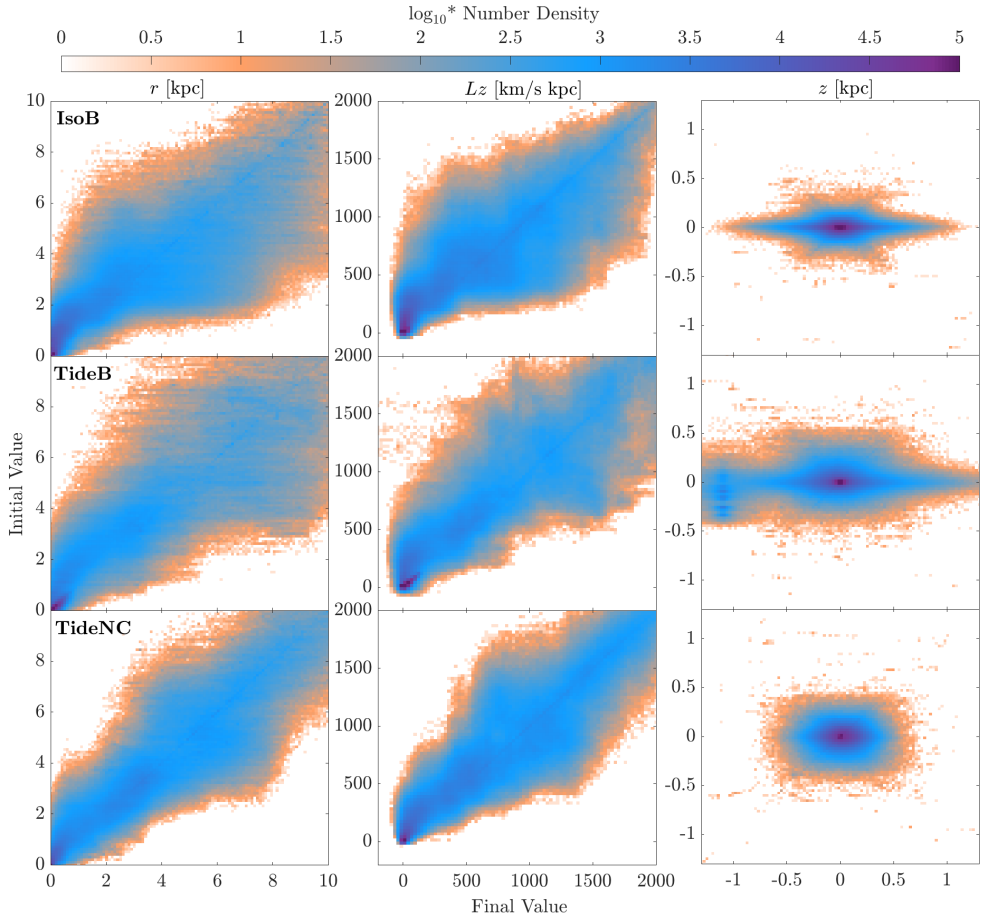

Figure 5.1: A representation of how initial (at star formation time) values relate to final (1 Gyr) values for attributes Δr, ΔL_z and Δz of stars formed in the simulation for each case: IsoB, TideB and TideNC. Each initial value is divided into equally sized bins and this component separated into similar bins representing the corresponding final values. The colour is weighted logarithmically by stellar number density.

As a general assessment of how these dynamical features change over the course of the lifetimes for stars formed in each of the three disks, initial and final values for radial position, scale-height and angular momentum are shown in Figure 5.1. In the following analysis, 'initial' is considered to be the value at the time of the star formation, while 'final' is the corresponding value for the same star at the 'present' time, that is, at the end of the simulated period (1 Gyr). In this figure, stellar particles are binned based on the initial values, then the corresponding final values for each of the particles in each bin are also subsequently binned into bins of the same size. In this way, it is possible

to observe the maximum likelihood for how each attribute may change over the simulation duration. A straight diagonal-line from bottom left to top right would indicate there is no overall change, as in this case initial = final. Spreading above this line would, therefore, indicate a decrease in value over the simulation, while spreading below this line is evidence of an increasing value. The colour weighting indicates the darker the colour the more likely it is for particles to behave in such a way.

Each of the three disks appear to exhibit different behaviours relative to the three attributes. At first glance, the most obvious similarity in all cases is that most stars which begin life at zero values, remain at zero. The TideNC disk is noticeably most different from the two more strongly barred-disks, in that the r and L_z values occupy a tighter envelope and therefore, signify a more consistent trend for all three attributes to remain mostly unchanged, with only slight deviations from the initial values to the final values. This is represented by the smooth and narrow diagonal-line feature mapping approximately to the line of initial = final in r and L_z and the more circular shape in the z distribution. In contrast, IsoB and TideB show some evidence of this diagonal-line feature, but it is significantly smeared or blurred to values both above and below the line of initial = final. This is indicative of a greater probability for large changes over the 1 Gyr duration in both disks. However, the shape of the envelope which delineates this spreading of values is evidently different between the two. For example, radial position for the IsoB disk appears broadest between 2-6 kpc whereas TideB is increasingly spread towards the outer radii ($r \geq 4$ kpc). This is likely a result of the tidal forces from the interaction impacting more significantly on the outer-edges of the TideB disk.

In L_z of TideB, there is also a large and consistent deviation from the central line for $L_z \sim 0 - 250$ km/s kpc, the likes of which does not appear in IsoB. The cause of this difference is also likely to be an effect of the tidal forces, however, it is not immediately possible to attribute this to a direct case of cause and effect. The z attribute in both IsoB and TideB indicates that stars formed in these disks must experience significant vertical dispersion which is not apparent in TideNC. Recalling Figure 3.2 in Chapter 3, this is likely related to the formation of the X-like feature in the galaxy cross-section which forms with the bars in IsoB and TideB but is not evident in the development of TideNC.

These changes between initial and final values can be directly prescribed as a single change parameter for each attribute (i.e. Δr, ΔL_z and Δz). The variations in these changes can be compared between the disks more precisely if represented in the form of a histogram. This histogram displaying the likelihood of stars to experience these changes in Δr, ΔL_z and Δz over the 1 Gyr simulation period is presented in Figure 5.2. In this figure, the IsoB compo-

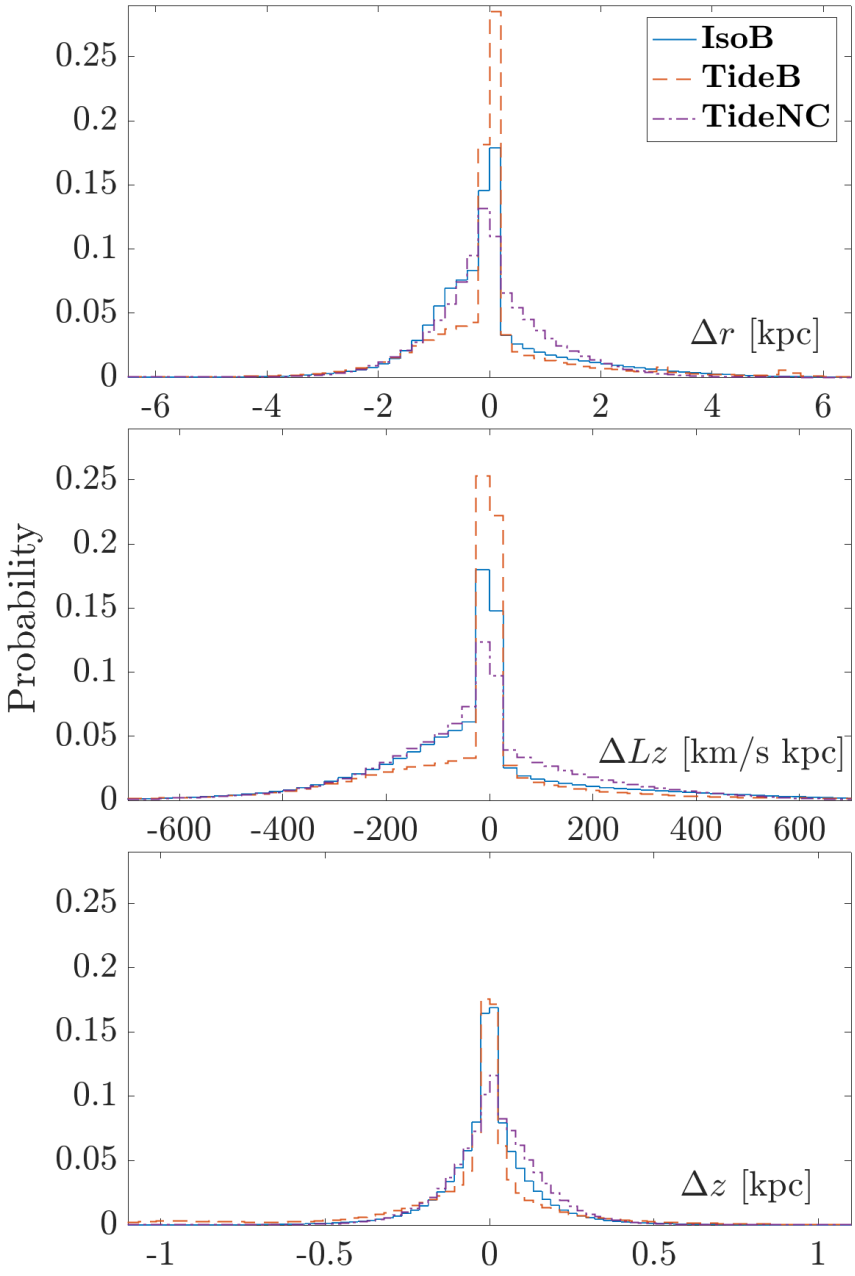

Figure 5.2: A histogram representing the total change over the simulation time (1 Gyr) in attributes Δr, ΔL_z and Δz of stars formed in the simulation for each case: IsoB (solid blue line), TideB (dashed orange line) and TideNC (dot-dashed purple line).

nent fills a solid blue line; TideB is represented by the dashed orange line; and, TideNC is instead outlined by a dot-dashed purple line. It is evident that the IsoB and TideB disks are distinguishably different from the relatively more structure-less TideNC over the 1 Gyr period, as in Figure 5.1. The total change for TideNC of each Δr, ΔL_z and Δz appears significantly more

symmetric and gaussian-like in the distribution which is centred on zero, conforming with Figure 5.1, wherein it appeared most likely for there to be no change in value for each attribute with only a small, consistent probability of spreading either side. However, while IsoB and TideB also show the most probable result is no change (i.e. peaks at approximately zero), the shape of the distribution is clearly not symmetric in either case. Similarly, both also appear to indicate a preference for stars to undergo negative changes in Δr and ΔL_z. That is, there appears to be a higher percentage of stars which experience inward radial migration and decreasing angular momentum. In both these disks, the probability of a given negative change seems to be approximately double the probability of the corresponding positive value. However, TideB is more consistently concentrated around zero than IsoB. So, although the trend of negatively skewed change is consistent, change overall is not as likely to occur. Comparatively, the change in scale-height is much more gaussian-like for both IsoB and TideB, however, these each produce a more strongly peaked profile than TideNC: the FWHM decreasing in order of TideNC, IsoB, then finally TideB. This is observed despite more stars exhibiting larger total changes of Δz in TideB than in either of the other disks.

As a first order assessment of the dependence for these changes on the non-axisymmetric structures in the disk as the simulations evolve, these changes are projected into the xy-disk plane. Similarly to figures in the preceding chapters (i.e. gas and stellar density - Figure 3.1, velocity - Figure 3.6, SFR - Figure 4.3), Figure 5.3 is a representation of the evolution of the median particle position and momentum changes: Δr, ΔL_z and Δz for particles within a $100 \times 100\,\mathrm{pc}$ grid square at the final time of each window. Additionally, these values are only calculated for stellar particles which have already formed by the initial time of each window, such that the change which occurs is measured over a consistent Δt which, in this case, is set to 200 Myr. Obvious disk structures are reproduced in these projections over the disk plane, particularly in the Δr and ΔL_z projections. Radii where the arms dominate exhibit clearly defined arm structures which also appear to experience the largest changes in both positive and negative directions. Arcs bracketing the bar, presumably from the arms decoupling, are also particularly evident in both Δr and ΔL_z. The regions with the largest changes in z appear to occur on the inner-edges of arms in the mid-outer parts of the disk.

Interestingly, TideB shows a number of asymmetric features in the inner/bar region between 400-800 Myr with small particularly bright or dark patches that are not necessarily associable with any visually significant morphological signatures. Contrastingly, except for the last epoch of TideNC, these projections almost appear featureless. This is likely to be representative of the significantly lower magnitude of the changes (if any) which occur for

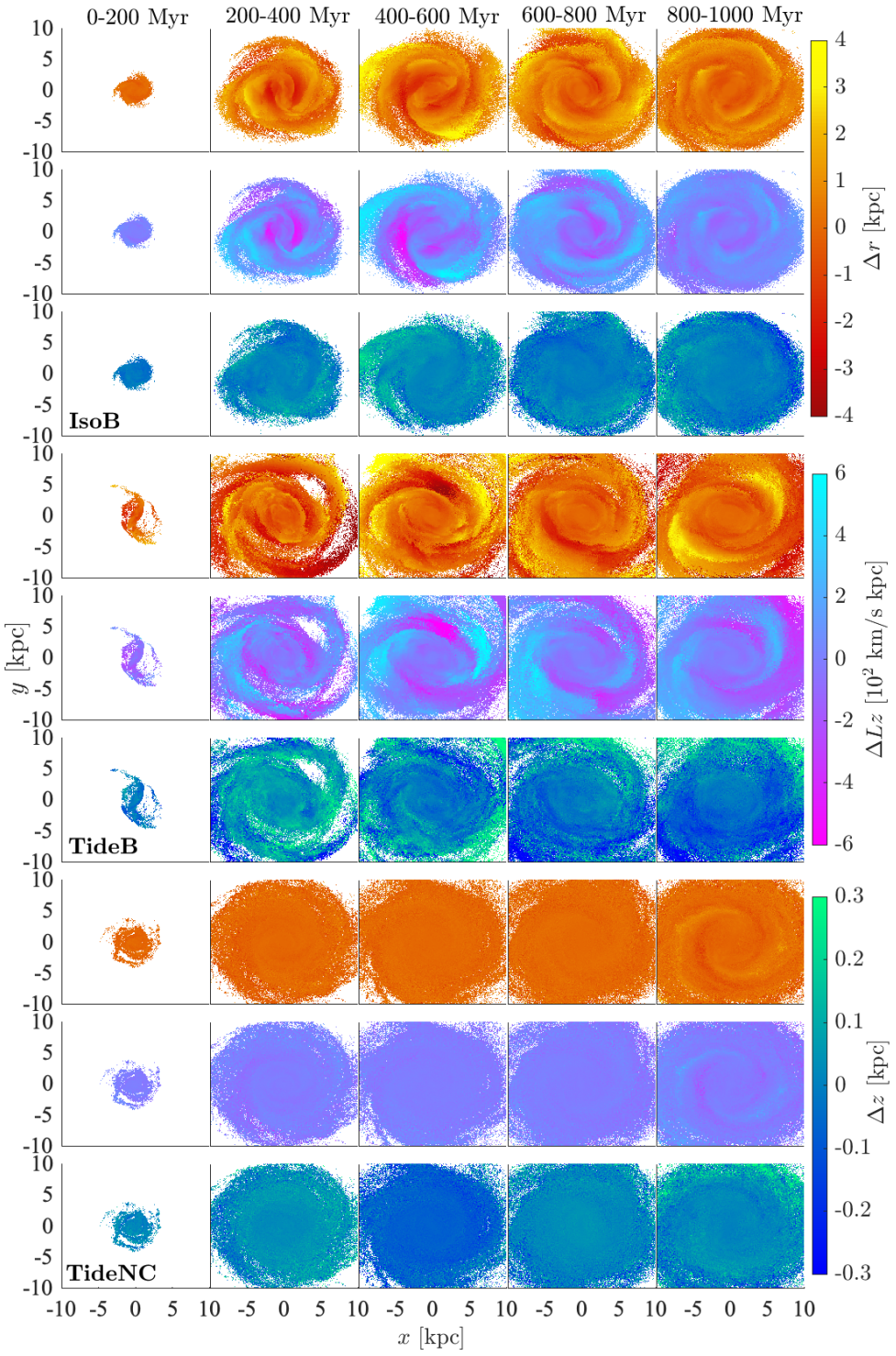

Figure 5.3: Projection of face-on changes in attributes Δr, ΔL_z and Δz set into the xy-plane for newly formed stars in the simulation for each case IsoB, TideB and TideNC. Median values in each grid square (100×100 pc) are used for colour weighting. Columns correspond to 200 Myr periods of evolution while including only stars existing for the entire period.

stars in this particular disk. Additionally, it appears that regions with large changes in r similarly seem to exhibit large changes in L_z with a corresponding consistency in the direction of these changes (i.e. large positive $\Delta r \Leftrightarrow$ large positive ΔL_z; large negative $\Delta r \Leftrightarrow$ large negative ΔL_z). There does not appear to be a similar correlation between either Δr or ΔL_z with features in Δz. However, by visual inspection, the correlation between Δr and ΔL_z does not appear to be an exact replication in terms of either the intensity of the changes or the precise, finer structural features. These small inconsistencies also seem slightly more apparent in the TideB case, possibly implying that blurring is more prevalent in a tidally affected disk than a disk where structure is driven by internal perturbation or that the interaction could be responsible for driving more disconnected responses in angular momentum and radial motion.

5.2 Changes Relative to Radial Position

As non-axisymmetric structure has been shown to affect stellar motions and create various torques across the disk, it follows that the differing disk conditions prevalent as this disk structure develops, may in turn differently affect the stellar populations existing in the galaxy at that time. In the following section, the impact on stars formed in the simulation is considered based on their initial radial positions at various periods of disk evolution. The initial values in this case, similar to Figure 5.3, are considered to be the value for each attribute as at the commencement time of each 200 Myr period. In this way, it is possible to constrain the migratory behaviour of stars from different sections of the disk. For all figures in this section, the colour weighting has been determined to be the number density of stellar particles with given initial radii which experience the change in value of a certain amount, weighted by the total number of particles existing in that period, thus producing a fractional probability density distribution for each response.

5.2.1 Standard Parameters

Figure 5.4 is a representation of the change in radial position (Δr) for simulation-formed stars in each of the three disks. Broadly, the shape of this distribution appears to vary between the overall evolution of these disks. The responses of IsoB and TideB, however, do exhibit some more similar traits which are either present to a significantly lesser extent in TideNC or not evident at all. For example, in the region of $r_i \lesssim 2\,\text{kpc}$ a large majority of stars in most epochs of IsoB and TideB appear to favour a predominantly inward trend ($\Delta r < 0$). This is most prevalent in both cases between 200-600 Myr where this inward radial motion is correspondingly increasing in inward magnitude from zero to

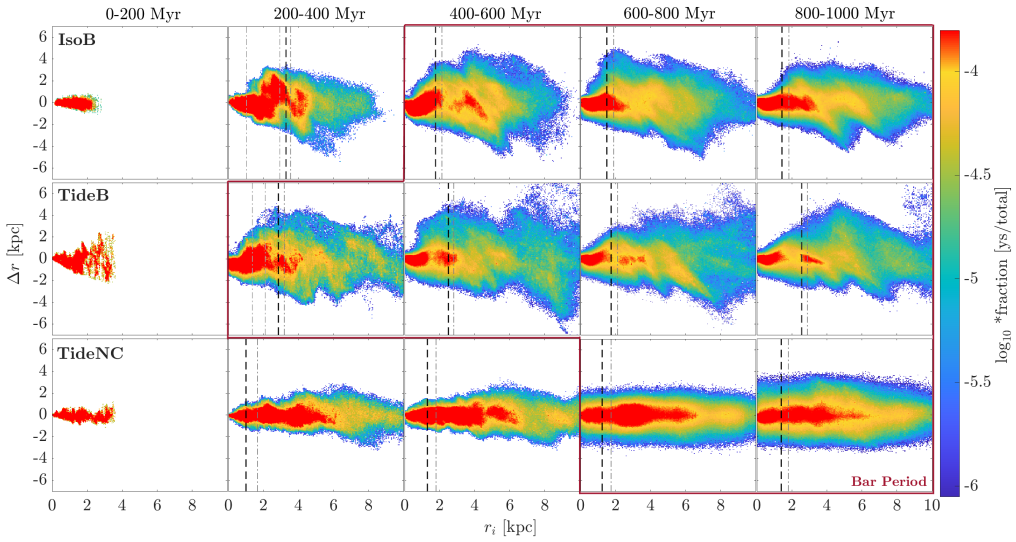

Figure 5.4: Dependence of attribute Δr with radial position at a given period of evolution of stars formed in the simulation for each case: IsoB, TideB and TideNC. Columns correspond to 200 Myr periods of evolution and include contribution from only stars present for the entire period to observe changes over the epoch completely. The colour is weighted logarithmically by stellar number density as a fraction of the total density.

~ 2 kpc. Significant diagonal spreading, like smudging sections of the envelope, is also consistently apparent in the responses of all three disks but the magnitude of these smudges is considerably lesser in the case of TideNC. IsoB has one obvious main feature like this centred on around 4 kpc, which is evident in all epochs to a varying extent, and perhaps a smaller notable case at about 6 kpc, which becomes more evident in later periods (after the bar is formed). TideB also exhibits this diagonal spreading in all epochs to a varying extent but the number of major resolvable features appears to be greater than the IsoB response. The two largest, most consistent smudges in TideB occur at ~ 3 kpc and ~ 6 or 7 kpc which is similar to the IsoB in the sense of disk orientation (one in the inner-mid disk, one in the outer-mid disk). These are in some cases related to resonance positions within the disk, however, as can be seen from the dashed lines in Figure 5.4, the most significant features do not seem to be closely associated with these resonances.

Within the barred periods of IsoB and TideB, although the overall shape seems similar, the density distribution of particles within this shape is obviously different. Within the bar extent, for example, IsoB maintains a large fraction of particles (red coloured: $\geq \log 10(-4)$) with approximately zero or small inward migration, spanning the entire bar length and this trend continues well out into the mid-disk in later periods. Comparatively, the barred periods

of TideB also show that most particles within the bar extent are concentrated at zero or small inward migration on average, however, this concentration is nowhere near as consistent. There is a separation at $r_i \sim 0.6 \times R_{\rm bar}$ where it appears much less likely for stars in TideB to exhibit zero change in radial position when compared to stars at the surrounding r_i, moving either inward or outward from there. Additionally, large contributions of coherent motion (red coloured: $\geq \log 10(-4)$) are rarely observed much further than the bar extent, even in later periods of TideB.

It is also possible to comment on the evolutionary histories of these disks based on the responses in Figure 5.4. The IsoB and TideNC disks, both evolving in isolated environments, appear quite similar in the 0-200 Myr period. Comparatively, this is the period in TideB which contains the closest approach from the companion (~ 100 Myr) and the ensuing response in Δr, particularly for r_i in the outer half of the disk radii, is obvious. Many stars can be seen to exhibit changes of more than double the response in either of the other cases. In subsequent time periods, the outer-disk in TideB continues to be more perturbed than in either IsoB or TideNC but the overall shape of the envelope is considerably more contained on average.

Change in angular momentum (ΔL_z) is similarly compared with an initial radial position in Figure 5.5. It can be seen that many features which are apparent in the Δr distribution (see Figure 5.4) are also observed in ΔL_z, such as the changing shape of the envelope and diagonal smudging, particularly in IsoB but also in TideB to a lesser extent. A number of the diagonal features identified in Δr, for both IsoB and TideB, are evident at the same r_i for the ΔL_z in this figure. For example, those centred around 4 and 6 kpc in the IsoB case are also particularly prevalent in the 400-600 Myr window in ΔL_z. However, in later periods of the IsoB case, only the inner (~ 4 kpc) smudge remains so apparent. Similar behaviour is reflected in the TideB case, although here the outer ($\sim 6 - 7$ kpc) smudge is the only prevalent feature which remains. These changes observed in both radial position and angular momentum indicate that the stars situated within these specific r_i locations are more likely to be largely motivated by torques from the non-axisymmetric features of the disk, driving migration by the process of churning (Sellwood & Binney, 2002).

Additionally, while the inner-most regions of both IsoB and TideB previously showed a similarly large tendency toward negative Δr values with increasing radius for $r_i \lesssim 2$ kpc, this is not reproduced as strongly – if at all – in TideB for ΔL_z whereas, each epoch of the IsoB case is comparatively quite similar to the Δr response. In TideB for these periods, stars are significantly more likely to show no change in angular momentum rather than the strong negatively skewed response of IsoB. However, the odd break at around

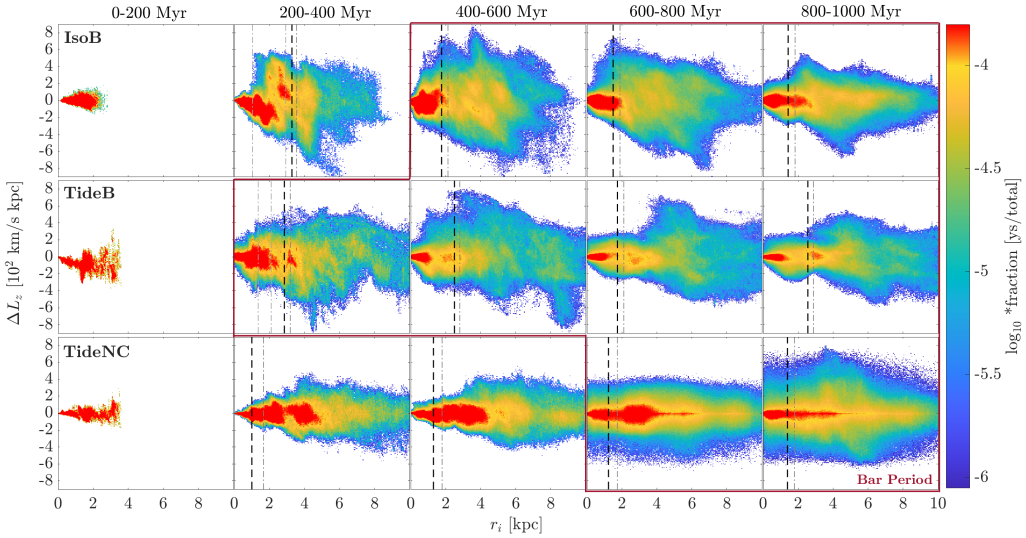

Figure 5.5: Dependence of attribute ΔL_z with radial position at a given period of evolution of stars formed in the simulation for each case: IsoB, TideB and TideNC. Columns correspond to 200 Myr periods of evolution and include contribution from only stars present for the entire period to observe changes over the epoch completely. The colour is weighted logarithmically by stellar number density.

$r_i \sim 2\,\mathrm{kpc}$ ($0.6 \times R_{\mathrm{bar}}$), where it is noticeably less likely to observe a zero change in radial position than stars located at surrounding radii, is even more apparent in the ΔL_z distribution. Again, this is not replicated in the IsoB or TideNC case. The location of this feature is also not consistently co-located with any of the smudge-like features, so it is currently unclear what is causing stars to preferentially leave this location.

Finally, Figure 5.6 allows for the assessment of any dependence between initial radial position, the corresponding disk structure and the changes to disk vertical position Δz. It is very clear from this figure, that the formation of the bar in IsoB and TideB must significantly drive vertical motion both above and below the disk plane. This is likely in accordance with the literature on bar formation wherein bars have been shown to warp in and out of the plane during the early stages of formation before settling into secular evolution (e.g. Friedli & Martinet, 1993; Łokas et al., 2014; Sellwood & Gerhard, 2020), which is exactly the period of focus for this analysis. Indeed, large changes in z are shown for precisely the barred periods of IsoB and TideB. A similar arrow-head shape can be observed, forming within the bar region with the arrow-point at (0,0) kpc and the maximum spread just inside the bar extent. The maximum extent in Δz of this flaring within the bar is almost double in TideB compared to IsoB (e.g. $\sim 1.2\,\mathrm{kpc}$ compared to $\sim 0.6\,\mathrm{kpc}$ in the $400 - 600\,\mathrm{Myr}$ epoch).

Additionally, despite the general arrow-head shape, the region where $\Delta z =$

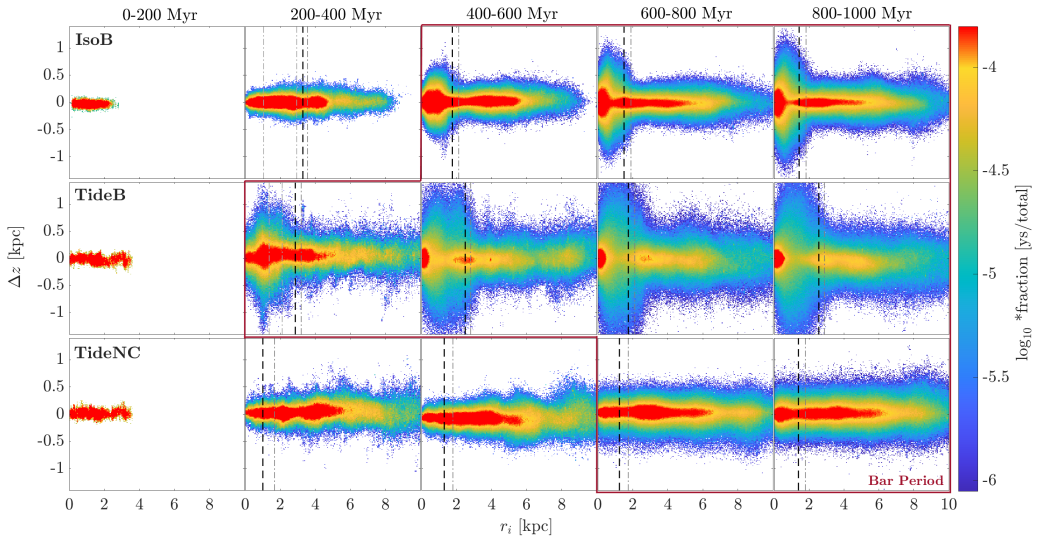

Figure 5.6: Dependence of attribute Δz with radial position at a given period of evolution of stars formed in the simulation for each case: IsoB, TideB and TideNC. Columns correspond to 200 Myr periods of evolution and include contribution from only stars present for the entire period to observe changes over the epoch completely. The colour is weighted logarithmically by stellar number density.

0 is consistently most prevalent in IsoB with most particles (red coloured: $\geq \log 10(-4)$) occupying this value, even for radii past the bar at $r_i \lesssim 6-7$ kpc. For a given $r_i \lesssim 7$ kpc in TideB, it would also be true that $\Delta z = 0$ is the most probable outcome, however the dominance this response is variable for different initial radii. Only in the centre-most region ($r_i \lesssim 1$ kpc) does this feature in TideB reach a similar fraction of stellar particles (red coloured: $\geq \log 10(-4)$) as comprises the feature in the IsoB response. Initial radii near the bar extent ($2.5 \lesssim r_i \lesssim 4$ kpc) may exhibit pockets of this maximum density at some epochs but the intervening region ($1 \lesssim r_i \lesssim 2.5$ kpc) is consistently on the order of $\sim 10 - 20\%$ less. This could be because there are in fact less stars within the radii in those regions overall or that the spread of Δz values is not only broader but more prevalent. It is true that this radial region does almost match with the peak of the changing Δz on the arrowhead shape.

It is noteworthy that, while the face-on stellar population in Figure 3.1b also clearly exhibits bar-like morphology in the central region in the later periods of TideNC, there is no indication of similar vertical spreading in the TideNC response at any epoch. This is, however, consistent with the lack of vertical (cross- or X-like) features in the side-on projection of TideNC. Some small wiggles can be seen in the envelope at various disk radii in earlier time windows but at the final epoch (800 Myr to 1 Gyr), the envelope is generally flat ($\Delta z = \pm 0.5$ kpc) and only a very small bulge is visible at $r_i \lesssim 1$ kpc

with $\Delta z \lesssim \pm 0.3\,\mathrm{kpc}$. However, unlike any of the other windows in this figure, only this last period of TideNC shows such a consistent and box-like envelope which is somewhat significant in and of itself. This should imply that the change in vertical position experienced by all stellar particles in this disk is consistent regardless of the radial position and possibly, despite all apparent non-axisymmetric disk structures.

5.2.2 Orbital Parameters

Similar analysis can be repeated to assess more specifically the effects on the orbits of individual stars within the disks for stars located at given initial radii. In this case, stellar orbits are defined for each star particle from an r_{min} and r_{max} value which determined within a given period as an approximation for the semi-major and semi-minor axis describing the orbital path. Here, the period to constrain each orbit is set to 100 Myr as this should contain at least one complete rotation for most disk particles, based on the disk pattern speeds. From these values, it is possible to derive an orbital eccentricity stellar motion–for a standard ellipse: $e = \sqrt{1 - b^2/a^2}$ where a and b correspond to the semi-major and semi-minor axes respectively. By assuming these elliptical orbits precess about the galactic centre on average, a typical radius for each stellar orbit can similarly be defined from r_{min} and r_{max} such that $r_{\mathrm{typ}} = (r_{\mathrm{min}} + r_{\mathrm{max}})/2$. The changes in these values can also be compared, as in the previous sections by the differences of Δecc and Δr_{typ} produced via the r_{min} and r_{max} values corresponding the 100 Myr periods preceding each initial and final time for the change period Δt.

Figure 5.7 is a representation of the changes in orbital eccentricity over time for stars located at various initial radii across the disks of each IsoB, TideB and TideNC. Similar to the general parameters of Δr, ΔL_z and Δz, the evolution of each of these three disks appears to affect the eccentricity of stellar orbits quite differently, although there are indeed similarities. Naturally, the interaction occurring in the earliest period of TideB appears to strongly affect the eccentricity of orbits in this period, preferentially driving large positive changes (i.e. orbits become more eccentric over time). However, in the periods following closest approach, the interaction effects on the eccentricity do not appear to be so significant, even for stars located in the outer-edges of the disk. The spread of changes in Δecc for $r_i \geq 4\,\mathrm{kpc}$ does not show any larger values, nor any significant preference for change in TideB than in either of the isolated IsoB or TideNC disks. In fact, the profile in this region may even be slightly slimmer, indicating that less significant changes occur in this region in TideB than in either IsoB or TideNC. Contrastingly, the eccentricity of stellar orbits appears to be significantly more affected within the central region of

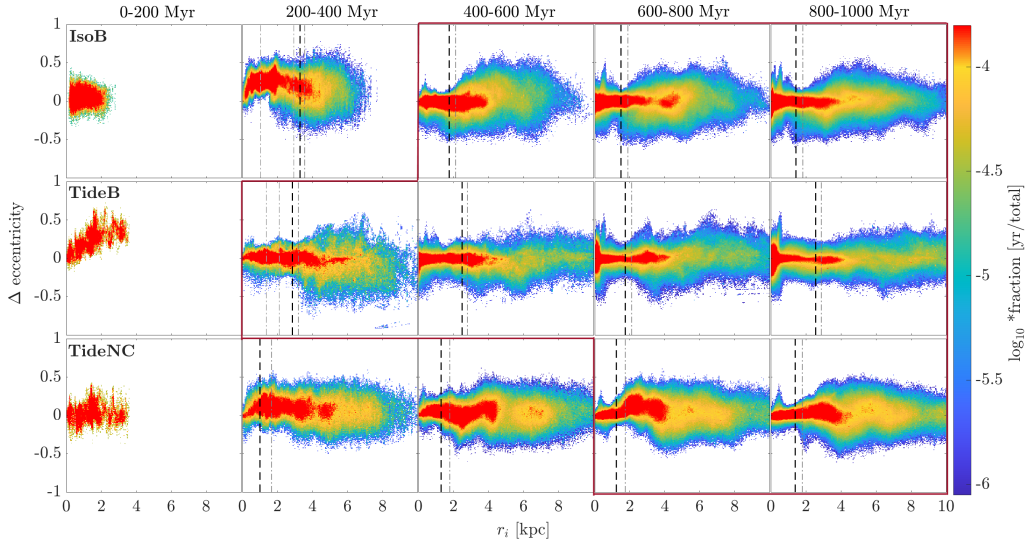

Figure 5.7: Dependence of attribute Δecc with radial position at a given period of evolution of stars formed in the simulation for each case: IsoB, TideB and TideNC. Columns correspond to 200 Myr periods of evolution and include contribution from only stars present for the entire period to observe changes over the epoch completely. The colour is weighted logarithmically by fractional stellar probability density.

TideB ($r_i \leq 1$ kpc), particularly between 600-1000 Myr. Similar features also appear in the inner regions between 400-600 Myr of TideB, between the same 600-1000 Myr period in IsoB and perhaps between 800-1000 Myr for TideNC. Additionally, all three disks obviously exhibit a bent-like shape for the envelope at r_i around the bar extent in the 200 Myr periods before the bar is considered to have formed (IsoB: 200-400 Myr; TideB: 0-200 Myr; TideNC: 600-800 Myr). This is even true of the TideNC disk which has previously not appeared to exhibit any similar features which have been associated with the bars in IsoB and TideB, particularly in the $z-$direction. This may indicate that the forces driving these changes in orbital eccentricity should be oriented within the disk-plane and that these changes should not be associated with vertical stellar motions in and out of the plane.

Similarly, changes to the typical radius for these stellar orbits based on initial radial position of stars in a given period of disk evolution can be read from Figure 5.8. This figure should appear comparable to the plots of Δr and ΔL_z (Figure 5.4 & 5.5) in the previous section. This figure serves as a direct representation of the radial change in the typical range of motion for simulation formed stars, irrespective of apparent changes in radius which may occur due to the elliptical shape of stellar orbits. The diagonal smudge-like features are also recovered and even appear to be accentuated in this figure, especially those

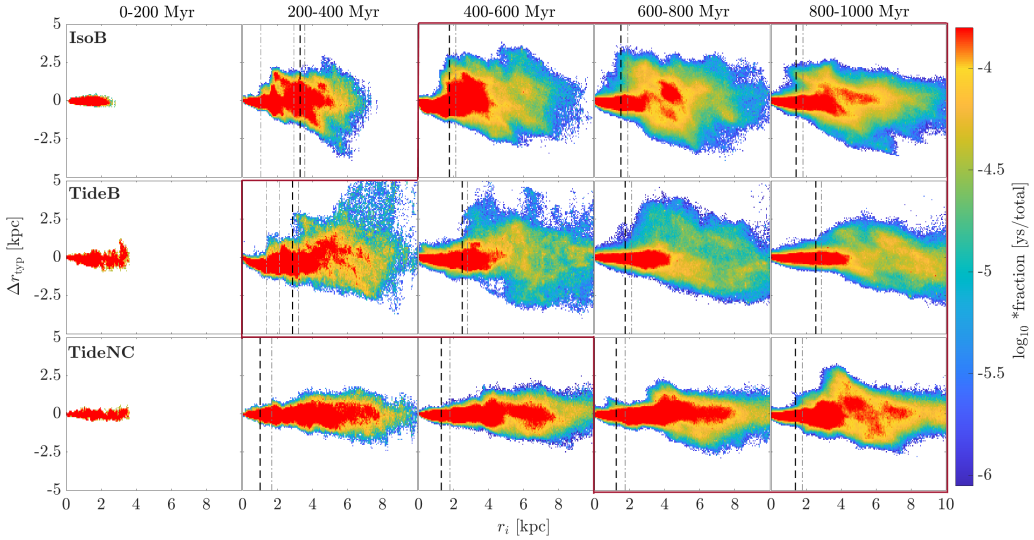

Figure 5.8: Dependence of attribute Δr_{typ} with radial position at a given period of evolution of stars formed in the simulation for each case: IsoB, TideB and TideNC. Columns correspond to 200 Myr periods of evolution and include contribution from only stars present for the entire period to observe changes over the epoch completely. The colour is weighted logarithmically by fractional stellar probability density.

in the mid- and outer-disk while the bar region appears comparatively quiet. However, it is noted that the scale of the Δr_{typ} axis is also less than Figure 5.4 so, it follows that the magnitude of change in these typical radii is, in fact, less than the changes observed in the total radial position of these stars and yet, the same primary features can be recovered. The most significant differences which are resolved in this figure, are instead in the TideNC response. The changes in typical radius for TideNC are significantly more similar to the IsoB (and to a lesser extent TideB) than any of the general attributes shown previously (e.g. Δr, ΔL_z, Δz). This disk also appears to produce a single main diagonal feature in the mid-disk, approximately centred on $r_i = 5\,\text{kpc}$, and is notably similar in profile to the other isolated disk IsoB at similar times relative to the bar formation in the face-on stellar profiles of each disk (see Figure 3.1b). This is perhaps indicative of the difference in the orbits between TideNC and the other two disks obscuring a more general analysis of properties which do not account for large periodic variations in stellar motions.

5.3 Age & Metallicity Dependence

From the analysis presented in the previous section, it is clear that the evolution of disk structure evidently impacts the dynamics of the existing stellar

populations in different ways. To continue tracing how this may impact the observable population mixing in the present-day disks of galaxies, stellar age and metallicity are important metrics.

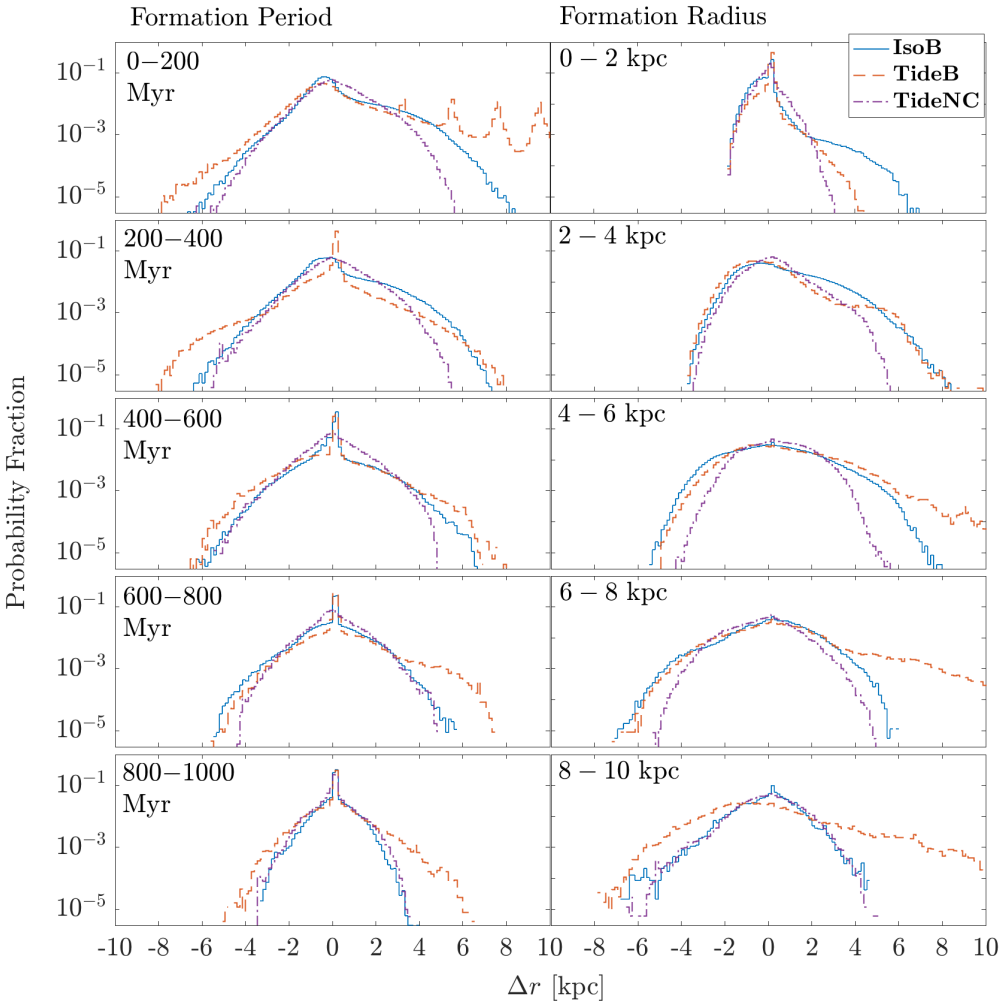

Figure 5.9: A histogram representing the total change over the simulation time (1 Gyr) in Δr for stars formed in the simulation for each: IsoB (solid blue line), TideB (dashed orange line) and TideNC (dot-dashed purple line). The stellar population is separated into five bins based on formation time in generations of 200 Myr (left) and formation radius in radial annuli of width 2 kpc (right).

5.3.1 Revisiting Total Change Histograms

Stellar age is one of the most straightforward observational parameters for distinguishing the stellar populations of galaxies. It is also a parameter able to be acquired directly from the simulation results. Figure 5.9 is a more detailed

deconstruction of the previous histogram for the total changes experienced by stars in Figure 5.2 from Section 5.1.

In the left panel of this figure, the total change in the radial position (Δr) of stars formed in the simulation is presented again, however, this is now separated into populations based on the stellar ages of particles – noting the $y-$axis scale is logarithmic to enhance the details in this figure. This displays how the probability of a star moving from its formation radius to the current observed radius varies for the different populations of stars. Over time the width of this feature appears to narrow for all three disks—that is, the youngest population of stars exhibit smaller changes in radius overall compared to older stars. This is not altogether unexpected as these younger stars have indeed had less total time to move from their formation positions. Additionally, the TideB stars experience the largest changes in radial position of all three disks, particularly those stars formed in periods around the closest-approach (i.e. the 0-200 population). However, these larger changes in radius are evident in all populations of TideB stars. The IsoB stars formed in the earlier periods of this disk (0-600 Myr) also appear to experience comparatively greater changes in position overall than stars formed at a similar time in TideNC, although less than in TideB. This trend, however, is not replicated for the youngest stars, as can be seen from the 800-100 Myr panel of this figure. These stars appear to experience almost exactly identical changes in radial position in both IsoB and TideNC, the disks with isolated evolutionary scenarios.

In contrast, the histograms presented in the right-hand side of this figure are separated based on the radial positions where these stars were formed, irrespective of when the star formation took place. As could well be expected, there is an exceedingly high number of stars formed in the outer regions ($r_{\rm form} \geq 6\,{\rm kpc}$) of the TideB disk which experience the maximum values of outward migration. This is very likely the consequence of the companion stripping gas and stars away from the disk. This trend toward higher positive values for Δr in TideB is also evident to a lesser extent for stars formed between 4-6 kpc, while stars at 2-4 kpc clearly experience similar changes overall to the IsoB disk with similar bar morphology. For stars formed within the centre-most region, however, TideB is significantly less likely to produce the same extent of radial change as IsoB. Stars formed in all three cases are more likely to experience small inward or zero changes overall but the probability distributions for IsoB and TideB are significantly more asymmetric than TideNC. Stars formed in the central and mid-regions of these two disks ($r_{\rm form} \leq 6\,{\rm kpc}$) are skewed with a long probability tail extending to larger positive values, indicating outward migration. This continues to be true for the outer-radii of TideB as mentioned previously; however, IsoB is instead slightly skewed to the opposite direction for formation radii of $r_{\rm form} \geq 6\,{\rm kpc}$, with an asymmetrically more extended distribution to

negative Δr values. Interestingly, the last panels of both columns are similar in that the IsoB and TideNC probability distributions appear to align only in this window. For the separation based on formation radius, this means that the behaviour of stars formed in the outer-edges of the disk ($r_{\text{form}} \geq 8\,\text{kpc}$) is similar for both isolated disks IsoB and TideNC without the tidal interference of the companion.

5.3.2 Evolution of Metallicity

Intrinsically related to stellar age, especially in this kind of numerical simulation, is the stellar metallicity. Observations of stellar metallicity are important for resolving many significant features particularly relating to the evolutionary histories of galaxies (e.g. Molla et al., 1997; Haywood et al., 2013; Magrini et al., 2009; Hayden et al., 2020; Lacerna et al., 2020). While the stellar metallicity in these simulated results relies heavily on a relatively large number of physical assumptions and should be assessed with caution, it is deemed sufficient for at least a comparative assessment of the conditions within these three disks. Most notably, the simulation metallicity parameter Z_{metal} is initialised from a solar seed value of 0.013 in metallicity, which is slightly un-physical and should be accounted for.

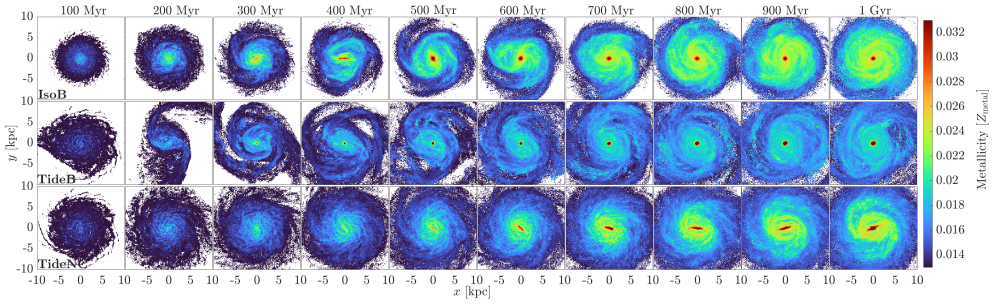

Figure 5.10: Projections for the face-on stellar metallicity distributions in terms of simulation metallicity parameter Z_{metal} set into the xy-plane for each case: IsoB, TideB and TideNC. Columns step in time by 100 Myr to the total simulation time of 1 Gyr.

The evolution of metallicity within the stellar disks of the three simulated results for IsoB, TideB and TideNC is presented in Figure 5.10. The face-on projections in this figure are similar to previous projections of gas and stellar density (Figure 3.1), velocity components (Figure 3.6), SFR (Figure 4.3) and the changes to Δr, ΔL_z and Δz for stars formed during the simulations (Figure 5.3). This allows for a preliminary visual assessment of how stellar metallicity is likely to evolve under these differing disk conditions and in the presence of the various non-axisymmetric structures over the 1 Gyr integration time.

Interestingly, IsoB and TideB are again similar, in that the most metal-rich stars appear preferentially located within the central, circular region defined as the nucleus for most, if not all, periods following the formation of the bar structure. Comparatively, the relatively indistinct bar feature within the TideNC disk is strongly highlighted in these projections. A thin, straight central region with very high metallicity is clearly evident in the latter 500 Myr evolution of this disk, while a circular central feature is consistently lacking except for, perhaps, some development in the centre of the final period at 1 Gyr. In all three disks, there appears to be higher metallicity components tracing the stellar arm features than the surrounding inter-arm disk regions, however the relative magnitude of this metallicity compared to the central region is notably lesser in the TideB disk. Both isolated disks, IsoB and TideNC, seem to exhibit similar metallicity components tracing the arm features and filling the mid- to outer-areas of the disks. These components in TideB are comparatively lower, less by approximately half the Z_{metal} fraction, but still similarly trace the structural features in this region of the disk.

In an effort to consider how radial migration may contribute to these different conditions of metallicity within the three disks, the previous figure depicting the relative dependence of a star particle's change in radial position based on its location at a given time (Figure 5.4) is weighted by the median value for metallicity Z_{metal} in each area of $r_i - \Delta r$ space, instead of probability density. The value for metallicity in this figure is also more accurately considered a measure of metallicity relative to solar metallicity ($Z_{\odot}$), in an attempt to remove the dependence of the simulated results on the initial solar seed. It is evident that the central regions with higher metallicity in IsoB and TideB, in the previous face-on metallicity distribution, are comprised of stars which are not only developed in-situ, but also must be funnelled into this region from the surrounding stellar populations. In IsoB particularly, the regions with large values of inward migration in Figure 5.4 map to similar regions with the highest values of metallicity in Figure 5.11. These high metallicity stars within the bar must therefore preferentially experience large inward migratory tendencies. However, in IsoB large changes throughout the disk are also ongoing for stars with moderately high metallicity. Comparatively, once the bar forms in TideB, there are not so many high metallicity stars located in the disk and the positional change appears generally irrespective of metallicity, outside a very small component of high metallicity stars in the central 1 kpc which continue to flow inward, particularly in the latter two periods ($t \geq 600$ Myr).

The earliest periods of TideNC also appear similar, with no obvious correlation between how stars are moving radially and the metallicity values recorded. However, the first possibly barred period of this disk (600-800 Myr) is notably different. There is a clear metallicity gradient across the disk with highest

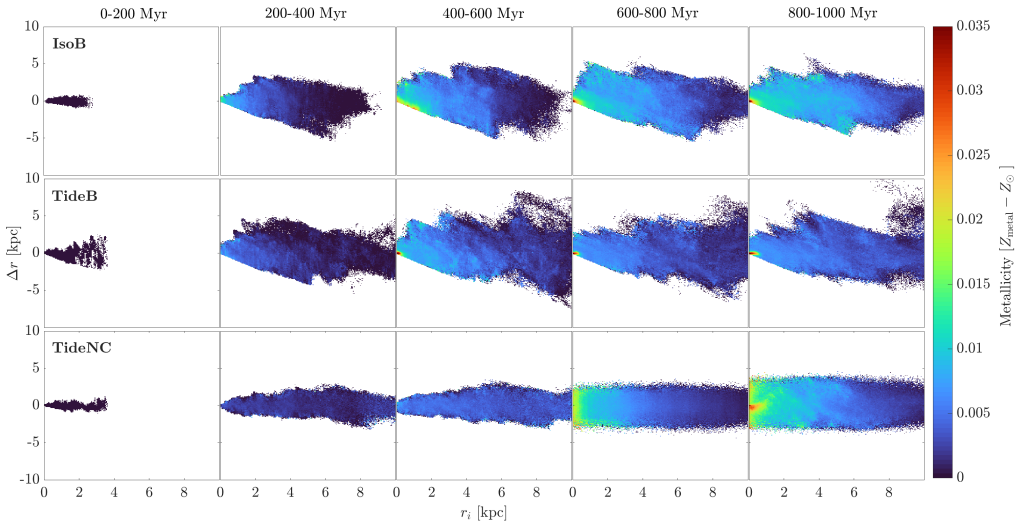

Figure 5.11: Dependence of attribute Δr with radial position at a given period of evolution of stars formed in the simulation for each case: IsoB, TideB and TideNC, as in Figure 5.4. Columns correspond to 200 Myr periods of evolution and include contribution from only stars present for the entire period to observe changes over the epoch completely. The colour is weighted by the median value for metallicity Z_{metal} in each area of $r_i - \Delta r$ space relative to solar metallicity $Z_{\odot}$.

metallicities in the centre decreasing towards larger initial radii. However, this is almost entirely independent of change in radial position Δr with only a little variation within the central ~ 3 kpc. This consistent gradiatent is obviously perturbed by the final period (800-1000 Myr). Within the consistent envelope of Δr values at this time, the features relative to metallicity stand out strongly. The moderately high metallicity (green: 0.01-0.025) stars in the regions ($r_i \leq 6$ kpc) are moving in various patterns, although neither inward nor outward overall. The highest metallicity stars (red: ≥ 0.025) are concentrated within the central 1 kpc and are notably show almost no preference for migration, concentrated around $\Delta r = 0$ kpc. However, there might be a slight inward inclination of these particles as the feature does not appear exactly centred around zero but some small negative change in radius. Such behaviour may explain why the distinct circular feature apparent in IsoB and TideB is not necessarily apparent in TideNC.

5.3.3 Observations of Trends at 1 Gyr

The purpose of tracing metallicity in these simulations is to eventually find a possible intersection with real observations of galaxies. To this end, it is important to consider, not only the time-dependent trends and evolution of

the stellar population over time, but also the single-snapshot trends akin to observational measurements. Here, the final snapshot at 1 Gyr is treated as the current-time galaxy for each possible bar formation mechanism in IsoB, TideB and TideNC. An initial attempt is undertaken to determine how the evolution of these disks has differently affected the possible results to be measured at this time. The fraction of elements in terms of iron (Fe) and oxygen (O) to the abundance of hydrogen (H) can be resolved from the simulation output. These are used as a means to imitate the possible observational measurements and are deconstructed based on the contributions from stars of a certain stellar age and/or formation radius.

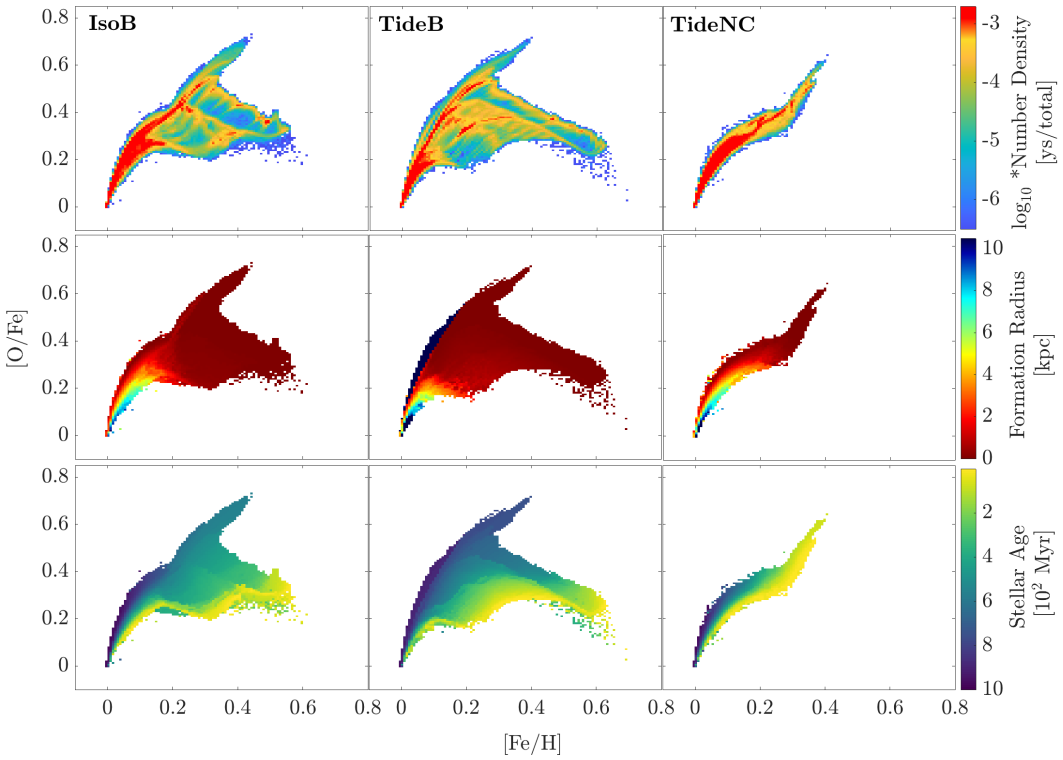

Figure 5.12: The fractional elements ([O/Fe] and [Fe/H]) at the final time period of 1 Gyr evolution for stars formed in each of the three disks: IsoB, TideB, TideNC. The top panel is weighted the radial position for each star at the time of formation with blue values corresponding to formation in the outer-disk, green in the mid-disk and red in the inner regions. The bottom panel is the corresponding age of each stellar particle with the youngest stars represented by the lightest colour (yellow) and the oldest stars by the darkest colour (navy blue).

The relative fraction of elements [O/Fe] – [Fe/H] is presented in Figure 5.12 for the final 1 Gyr snapshot of each disk. These are independently weighted by the fractional number density of particles (as in previous Figures 5.4, 5.5,

5.6 etc.), radial position of stars at the time of formation and the age of each stellar particle. The overall shape exhibited is clearly different for each disk, although once again the similarly barred disks of IsoB and TideB are more similar in general features, while still differing in detail, compared to the TideNC result. These disks include a distinct component of stars with higher fractions of (≥ 0.3) [Fe/H] which is characterised by the long, additional horizontal population of stars in each panel. This component is predominantly younger and is consistently formed within the centre-most region ($\lesssim 1\,\mathrm{kpc}$). The distinct lack of this feature in TideNC is likely to be significant, if not in a physical sense, at least as a clear point of difference between the three disks. Additionally, the minimum age of this horizontal component is clearly older in the TideB case than in IsoB and the difference between the ages of these stars is $\sim 200\,\mathrm{Myr}$ – the difference in time it took for each disk to first form a bar. Upon closer inspection, based on the age of the stars at the branch point, the maximum age of this feature corresponds to the formation period determined for each bar almost exactly. This implies that it may be the formation of the bar which has caused the conditions in the central region to be able to produce these higher [Fe/H] values, a condition which has clearly not occurred in the formation of the bar in TideNC.

Comparatively, there is much less distinction between the formation radius of stars in the metallicity distribution represented by this figure. In the lower quadrant of the distribution ([O/Fe] ≤ 0.4, [Fe/H] ≤ 0.3), there is an obvious colour gradient spanning central to outer radii from top-left to bottom-right of the distribution in each of the three disks. The region occupied by this colour gradient in two disks with isolated evolutionary histories (IsoB and TideNC) appears most similar, with IsoB slightly shallower than TideNC. In TideB, this component is significantly shallower, only extending up to ~ 0.2 in [O/Fe] but still appears to extend to the same fractions of [Fe/H] as the other two disks. Additionally, TideB has a component of stars formed in the outer-disk ($r_{\mathrm{form}} \geq 9\,\mathrm{kpc}$) which occupies the left-facing edge of the metallicity distribution. This is not seen in either of the isolated disks. This component is clearly comprised of the most early formed stars and is expected to be directly related to the disruption in the outer-disk of TideB as the companion passed at closest-approach ($\sim 100\,\mathrm{Myr}$). This edge is also more linear in the TideB result, tracing a smoother curve to higher fractions of [O/Fe] for low values of [Fe/H], also possibly related to the interaction-driven starbursts triggered by that event.

The radial dependence for the fraction of elements [O/Fe] for each of the three disks is compared more directly in Figure 5.13, in terms of the current position r in the 1 Gyr period. Additionally, to assess whether there is some variation in this dependence for stars which have formed in different regions

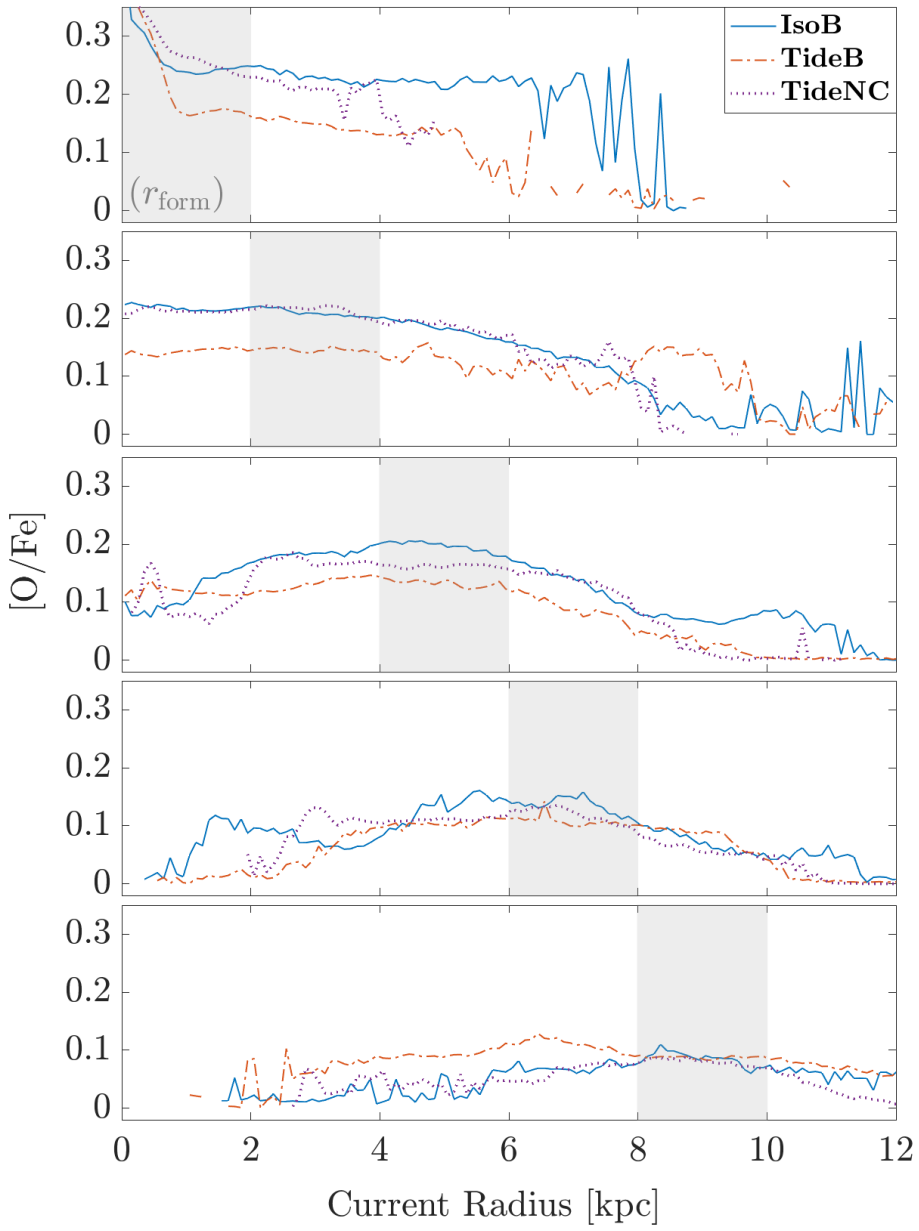

Figure 5.13: Metallicity distribution ([O/H]) with radial position (r) in the final 1 Gyr period of simulation evolution, in five windows based on radial position at formation ($r_{\rm form}$) for stars formed in the simulation. Metallicity distributions for IsoB (solid blue line), TideB (dot-dashed orange line) and TideNC (dotted purple line) are compared. In each panel, the radii which correspond to the formation radius of a given component is shaded in grey.

of the disk, each contribution is separated into five bins of formation radii spanning $[0-2]$, $[2-4]$, $[4-6]$, $[6-8]$ and $[8-10]$ kpc respectively. There is

no consideration for a dependence on stellar age; contributions from all stars formed by 1 Gyr are included in the calculations for this figure. In each panel, the radii which correspond to the formation location for these stars are shaded in grey. Any components with values resolved at current radii outside of the grey shaded region, can be considered to have moved with these metallicities away from the original location.

It is immediately apparent that the radial dependence and metallicity for stars formed in the two isolated disks of IsoB and TideNC are very similar. This is particularly evident in the $r_{\rm form} = [2-4]$ and $[8-10]$ kpc components, as could well be expected from the analysis in the previous sections (see, for example, Figure 5.10 & 5.11). Similarly, the TideB metallicity is consistently lower overall for most values of current radius except for the component formed and remaining in the central 1 kpc of the disk, the component formed between 2-4 kpc which has been pulled to outer-radii ($r \geq 8$ kpc) and the components formed in the outer-disk ($r_{\rm form} \geq 8$ kpc) which have migrated inward. The IsoB and TideB disks have most differences in metallicity values for stars formed within 4 kpc, however, the shape of the metallicity distribution with current radius for these components is seemingly most consistent (excluding the far outer-edges where the interaction effects may still dominate).

These results serve to illustrate directly that stars formed in different regions of the disk contribute different metallicity components to the total distribution across the disk of the galaxy. However, while there are small fluctuations arising from the differing bar and structure formation mechanisms assessed, the general shape of this radial dependence appears to differ little from each component of formation radii, except to raise or lower the overall magnitude of the [O/Fe] fraction in the metallicity distribution.

Chapter 6

Conclusions

The evolution of bar structure was studied in three simulated disk galaxies to characterise the effects of such structure, along with the mechanisms which may drive its formation, on the star forming potential and stellar dynamics of barred-type galaxies. Produced via hydrodynamical N-body simulations and tailored with observational parameters from the well-studied, nearby barred-spiral galaxies NGC 4303 (IsoB) and NGC 3627 (TideB, TideNC), the results from these disks provide insights into the attributes of galactic bars and their ongoing role in galactic evolution. Significant trends in the stellar populations and star formation tendencies were identified and considered to determine whether bar origin influences such features in a way which is distinct and observationally discernible. For the two bar formation mechanisms assessed – disk instability during an isolated evolutionary history (IsoB, TideNC) and tidally-driven disk interference arising from interaction with a passing companion (TideB)–there is indeed evidence that these properties are differently affected in response to each scenario.

The two primary disks for comparing the effects of bar origin on stellar properties (IsoB & TideB) each produce similar exponential, late-type bar morphology over the integration time of 1 Gyr and appear generally analogous to the specified target galaxies. TideNC without the influence of the companion affecting TideB, remains relatively featureless by comparison, before finally forming a visually dissimilar bar, especially in bar vertical stellar structure, in later periods. However, all three disks can be considered to have produced barred galaxies with a generally sweeping two-arm structure in the gas and stellar components and are capable of forming stars.

The rotation curves of the two observational analogues confirm that the IsoB and TideB disk are both sufficiently able to evolve similar non-axisymmetric features in the circular velocity to observations of NGC 4303 and NGC 3627. These also occur for the time periods where the face-on structure of these galaxies is most visibly consistent with the target galaxy observations. The

radial and tangential velocity profiles of these two disks appear relatively similar in terms of the shape of features across the disk, although the degree of non-axisymmetric motion in TideB is notably larger in all evolutionary epochs considered.

Comparing the evolution of star formation in these two disks, it is immediately evident that the formation of the bar triggers a significant burst of centrally located star formation: 79% increase for IsoB and 66% for TideB which can be considered similar. Additionally, TideB also undergoes a period of intense star formation, predominantly located in the spiral arms and driven by the interaction at approximately the period of closest-approach ($\sim 100\,\mathrm{Myr}$) which accounts for a 31% burst of star formation. The SFR also varies visibly with non-axisymmetric disk structure, both spatially and evolving with the disks over time. IsoB and TideB clearly exhibit distinguishable star forming structures of SFR when projected into the disk-plane. These structures each evolve differently with the varied formation mechanisms, despite the similar values of SFR in each disk on average.

The observationally derived Kennicutt-Schmidt relation between gas availability by way of Σ_{gas} and surface star formation rate of Σ_{SFR}, provides a metric for comparing the bar origins of these two disks, as well as a comparison with observations of NGC 4303, NGC 3627 and the broader star forming trends in observable galaxies on the whole. In this relation, TideB most notably displays a much higher distribution of inefficiently star forming, high density regions of gas which appear to be mostly confined to the outer-disk and are likely to be a contribution from tidal debris that is not yet completely stripped from the disk limits. While the shape of the contours tracing this relation for IsoB and TideB appear different, both disks appear to conform generally to the relations identified from the literature.

Additionally, clear trends are identified in the morphological dependence of this relation. Regardless of the difference in formation mechanism, the bar component in both disks follows a significantly steeper profile than any other component or the disk average. There appears to be very little visually distinguishable difference between the arm and inter-arm components. However, by fitting a gradient or determining the regional average, it is immediately obvious that the arm component is more similar to the overall disk average, while the inter-arm produces the shallowest profile and lowest values on average. These values are also found to be reasonably consistent with observations of NGC 4303 and NGC 3627 within the constraints of differing regional classification schemes between previous studies, and the known effects of resolution and simulated star formation recipe on the Kennicutt-Schmidt relation.

In an attempt to remove the dependence of differing morphological classification schemes on the determination and comparison of star formation in

these disks, a directional approach along the disk radius and bar major axis was also employed. The overall radial dependence of SFE in the early stages of bar formation was found to decrease strongly with increasing radius in both barred-disks. However, the two mechanisms attributed to driving bar origins in the form of IsoB and TideB are distinctive in the periods of evolution immediately post-bar formation. TideB is distinguished by a unique trend of radially increasing SFE on average across the disk and an associated dearth of star formation which persists along the bar between the centre and bar-ends. Such features are attributed to the tidal interference, possibly due to shocks or shearing from the higher values of non-axisymmetric motion driven by the companion, tidal torques, or the early starbursts (i.e. at closest-approach) too quickly absorbing available resources in the central region.

Meanwhile, SFE in the IsoB disk is generally constant on average for radii outside the central 1 kpc and, although periods exist where there is a similarly high SFE at the bar-ends and low SFE in the intervening sections, this trend is transient and appears more randomly. These differences between IsoB and TideB are reflected in observations of the target galaxies, NGC 4303 and NGC 3627, as well as a number of other resolved galaxies with similar conditions. Hence, such features are considered as potential signatures for identifying a barred-system post-interaction. However, the ambiguity arising from the transient feature also appearing in the isolated disk, must first be resolved in order to conclusively make a distinction in measurements of the single epochs necessitated by the long evolutionary time-scales of observed galaxies.

Tracing the motion of stars formed under these different star forming conditions through the periods of disk structure evolution should enable a resolution for these ambiguities. However, if the bar formation mechanism differently affects star formation, even in similarly barred-disks, it is likely that the stellar kinematics and dynamics driving long-term stellar motions will also be differently affected. This was confirmed using the three simulated disks of IsoB, TideB and TideNC over the full 1 Gyr integration time. These disks with different mechanisms driving bar formation exhibit traits in stellar motions which are different and attributable to both the formation mechanism and the specific bar morphology.

Changes to attributes of radius r, angular momentum L_z and scale height z provide the general co-ordinates by which stellar motion over time is assessed. Over the 1 Gyr period, the TideNC disk appears to present a tendency to remain broadly unchanged overall, while the two primary disks for comparison, IsoB and TideB, exhibit a comparably significant propensity for change, although it is most likely for stars in all three disks to experience little or zero values of change in these parameters. From a projection of these changing parameters into the face-on disk plane, it is evident that arm structures are

traced by features with the largest values for change in Δr and ΔL_z, as are the arcs which are the result of bar-arm decoupling.

Stars in IsoB and TideB are also each more likely to exhibit inward migration and decreasing angular momentum (negative Δr and ΔL_z) over the course of the disk evolution, however, this is only half as likely to occur for stars in TideB as in IsoB. The largest changes in r and L_z for both isolated disks, IsoB and TideNC, appear in the mid-disk at radial positions between $\sim 2 - 8\,\mathrm{kpc}$ whereas TideB is more likely to experience large changes in the outer radii $\geq 4\,\mathrm{kpc}$. The formation of the bar in IsoB and TideB also generates significant movement in the z positions of the similarly barred IsoB and TideB within the bar region. However, this is not observed in the TideNC disk, and is thought to be correlated with the lack of the cross- or X-shaped feature in the side-on projection of the stellar component in TideNC, a feature which is clearly evident in both IsoB and TideB.

There is a feature in the TideB disk where the most likely value of zero within the central region shows a clear separation for stars originally located at radii just inside the bar region, which is not replicated in either of the isolated IsoB or TideNC. This indicates that there is either some active force preferentially driving stars to leave from these radii, or that there are significantly fewer stars in this region compared to the surrounding radii and yet, a similar fraction of the total number of stars overall will still move away. These initial radii correspond almost exactly to the region where the dearth of SFE is found to persist within the bar. It follows that there should be a correlation with this point. However, such a feature is not necessarily so easily observable when considering the change in eccentricity or typical radius of the stellar orbits for stars passing through in this region. Comparatively, defined attributes in the otherwise relatively featureless TideNC are much clearer in these orbital parameters. In both Δecc and Δr_{typ}, TideNC in the later, barred periods appears significantly more similar to the other isolated disk, IsoB.

The observable attributes of age and metallicity, important for observational determinations of population mixing and the corresponding theories of disk evolutionary history, are significantly affected by the mechanisms driving bar formation. The isolated disks (IsoB and TideNC) generally exhibit similar changes in position and angular momentum, in terms of stellar age, as well as star formation radii. This is particularly evident for stars formed after the bar has developed in both disks and for stars formed in the outer-radii. Naturally, TideB is more affected by the companion in the outer-radii and for stars formed in periods near to closest-approach. The evolution of metallicity is also more similar between IsoB and TideNC, while the tidally-driven TideB appears to develop with consistently lower metallicity and no significant metallicity dependence with radial migration for stars located outside of $\sim 1\,\mathrm{kpc}$.

The main difference between IsoB and TideNC also occurs within this central region ($\leq 1\,\mathrm{kpc}$) where, instead, IsoB and TideB are most similar with the development of a well-defined central circular region with high metallicity and a tendency toward strong inward motions for high metallicity stars in the nearby regions. This central circular region is not observed in TideNC but the trend of inward motion for higher metallicity stars does appear in the later period where the bar is developed. Instead, a well-defined bar feature of high metallicity is evident in the central region of TideNC, persisting even from periods before the bar is obvious in the full stellar density distribution of this disk.

Features in the metallicity distribution were also found to vary between the three disks in the event that the 1 Gyr snapshot is considered a single observation, which similarly makes each disk distinguishable by either the formation mechanism or the bar morphology. An additional feature with higher fractions of [Fe/H] (≥ 0.3) for a given [O/Fe] is revealed in the relative fraction of elements for IsoB and TideB that is not evident in TideNC. This feature has been determined to be comprised of predominantly younger stars with formation radii almost exclusively in the inner $\sim 1\,\mathrm{kpc}$. The intersection of this component with the main diagonal feature in the [Fe/H]–[O/Fe] space, notably also occurs for stars which were formed at almost exactly the bar formation time. This implies that the conditions necessary to generate such a feature must be related to the formation of the bar in these two disks but not related to the formation of the bar in TideNC. Based on the formation radii, it can be assumed that this is relatable to the existence (or lack thereof) of the circular nucleus which is present in the metallicity maps of IsoB and TideB but not in TideNC.

A gradient from inner- to outer-radii corresponding to metallicities with high to low values for the [O/Fe] fraction can also be observed within the main diagonal feature in the elemental abundance ratios for all disks. However, this feature is significantly shallower for TideB than the isolated disks and is accompanied by a high [O/Fe], low [Fe/H] component of outer-disk formed stars which is extraneous to the gradated component found to be similar between the three disks. This analysis indicates that stars formed in different regions of the radial disk structure provide different contributions to the complete metallicity distribution of the galaxy. The mechanisms driving bar formation, however, do not appear to significantly affect the nature of these contributions, except in the very outer-radii of the tidally-driven disk where it can be expected that interaction effects should be strongest and most prolonged. In the case of metallicity fractions, only higher (or lower) overall magnitude in the distribution for the isolated (tidally-driven) disks, can be considered to relate to a given bar origin.

With these results, it may now be possible to trace and identify the differences between the formation and evolution of isolated and tidally-driven bars in the disks of galaxies, at a single time period in these three disks, and in similar simulations of disk galaxies. Constraining the attributes of these differences into measurable stellar properties for observational instruments, would then allow for the determination of the specific origins for bars and thus, the evolutionary histories of resolved galaxies. This is an endeavour to be continued in future works.

Bibliography

Abadi M. G., Navarro J. F., Steinmetz M., Eke V. R., 2003, The Astrophysical Journal, 597, 21

Adibekyan V. Z., et al., 2013, Astronomy & Astrophysics, 554, A44

Agertz O., et al., 2021, Monthly Notices of the Royal Astronomical Society, 503, 5826

Aguerri J. A. L., Méndez-Abreu J., Corsini E. M., 2009, Astronomy & Astrophysics, 495, 491

Ahn C. P., et al., 2012, The Astrophysical Journal Supplement Series, 203, 21

Allende Prieto C., Kawata D., Cropper M., 2016, Astronomy & Astrophysics, 596, A98

Antoja T., Valenzuela O., Pichardo B., Moreno E., Figueras F., Fernández D., 2009, The Astrophysical Journal, 700, L78

Athanassoula E., 1992, Monthly Notices of the Royal Astronomical Society, 259, 345

Athanassoula E., 2002, The Astrophysical Journal, 569, L83

Aumer M., Binney J., 2017, Monthly Notices of the Royal Astronomical Society, 470, 2113

Aumer M., Binney J., Schönrich R., 2016a, Monthly Notices of the Royal Astronomical Society, 459, 3326

Aumer M., Binney J., Schönrich R., 2016b, Monthly Notices of the Royal Astronomical Society, 462, 1697

Baba J., 2015, Monthly Notices of the Royal Astronomical Society, 454, 2954

Baba J., Kawata D., 2020, Monthly Notices of the Royal Astronomical Society, 492, 4500

Balcells M., Peletier R. F., 1994, The Astronomical Journal, 107, 135

Barnes J. E., Hernquist L., 1996, The Astrophysical Journal, 471, 115

Belfiore F., et al., 2018, Monthly Notices of the Royal Astronomical Society, 477, 3014

Belokurov V., Erkal D., Evans N. W., Koposov S. E., Deason A. J., 2018, Monthly Notices of the Royal Astronomical Society, 478, 611

Bensby T., Feltzing S., Lundström I., 2003, Astronomy & Astrophysics, 410, 527

Bensby T., Feltzing S., Oey M. S., 2014, Astronomy & Astrophysics, 562, A71

Beuther H., Meidt S., Schinnerer E., Paladino R., Leroy A., 2018, Astronomy and Astrophysics, pp 1–14

Bigiel F., Leroy A., Walter F., Brinks E., De Blok W. J., Madore B., Thornley M. D., 2008, Astronomical Journal, 136, 2846

Binggeli B., Sandage A., Tammann G. A., 1985, The Astronomical Journal, 90, 1681

Bird J. C., Kazantzidis S., Weinberg D. H., Guedes J., Callegari S., Mayer L., Madau P., 2013, Astrophysical Journal, 773

Bland-Hawthorn J., et al., 2019, Monthly Notices of the Royal Astronomical Society, 486, 1167

Bournaud F., 2011, EAS Publications Series, 51, 107

Bournaud F., Elmegreen B. G., 2009, The Astrophysical Journal, 694, L158

Bournaud F., Elmegreen B. G., Teyssier R., Block D. L., Puerari I., 2010, Monthly Notices of the Royal Astronomical Society, 409, 1088

Bovy J., Leung H. W., Hunt J. A. S., Mackereth J. T., García-Hernández D. A., Roman-Lopes A., 2019, Monthly Notices of the Royal Astronomical Society, 490, 4740

Breda I., et al., 2020, Astronomy and Astrophysics, 635, 1

Brook C. B., Kawata D., Gibson B. K., Freeman K. C., 2004, The Astrophysical Journal, 612, 894

Buck T., 2020, Monthly Notices of the Royal Astronomical Society, 491, 5435

Buta R. J., 2019, Monthly Notices of the Royal Astronomical Society

Calura F., Menci N., 2009, Monthly Notices of the Royal Astronomical Society, 400, 1347

Casagrande L., et al., 2016, Monthly Notices of the Royal Astronomical Society, 455, 987

Casasola V., Hunt L. K., Combes F., García-Burillo S., Neri R., 2011, Astronomy and Astrophysics, 527

Catalán-Torrecilla C., et al., 2017, The Astrophysical Journal, 848, 87

Chabrier G., 2003, Publications of the Astronomical Society of the Pacific, 115, 763

Chiappini C., Matteucci F., Gratton R., 1997, The Astrophysical Journal, 477, 765

Colbert E. J. M., Heckman T. M., Ptak A. F., Strickland D. K., Weaver K. A., 2004, The Astrophysical Journal, 602, 231

Cole D. R., Debattista V. P., Erwin P., Earp S. W. F., Roškar R., 2014, Monthly Notices of the Royal Astronomical Society, 445, 3352

Colina L., Wada K., 2000, The Astrophysical Journal, 529, 845

D'Onghia E., Springel V., Hernquist L., Keres D., 2010, The Astrophysical Journal, 709, 1138

Dalcanton J. J., Bernstein R. A., 2002, The Astronomical Journal, 124, 1328

Daniel K. J., Wyse R. F., 2018, Monthly Notices of the Royal Astronomical Society, 476, 1561

Darg D. W., et al., 2010, Monthly Notices of the Royal Astronomical Society, 401, 1552

Debattista V. P., Sellwood J. A., 2000, The Astrophysical Journal, 543, 704

Dehnen W., 2000, The Astrophysical Journal, 536, L39

Dehnen W., Aly H., 2012, Monthly Notices of the Royal Astronomical Society, 425, 1068

Di Matteo P., Combes F., Melchior A.-L., Semelin B., 2007, Astronomy and Astrophysics, 468, 61

Di Matteo P., Haywood M., Combes F., Semelin B., Snaith O. N., 2013, Astronomy and Astrophysics, 553, 1

Dobbs C. L., 2013, Proceedings of the International Astronomical Union, 9, 221

Dobbs C. L., Bonnell I. A., Pringle J. E., 2006, Monthly Notices of the Royal Astronomical Society, 371, 1663

Dobbs C. L., et al., 2014, Protostars and Planets VI, 3

Downes D., Reynaud D., Solomon P. M., Radford S. J. E., 1996, The Astrophysical Journal, 461, 186

Efstathiou G., Lake G., Negroponte J., 1982, Monthly Notices of the Royal Astronomical Society, 199, 1069

Eggen O. J., Lynden-Bell D., Sandage A. R., 1962, The Astrophysical Journal, 136, 748

Egusa F., Kohno K., Sofue Y., Nakanishi H., Komugi S., 2009, Astrophysical Journal, 697, 1870

Elmegreen B. G., Elmegreen D. M., 1985, The Astrophysical Journal, 288, 438

Elmegreen D. M., Sundin M., Elmegreen B., Sundelius B., 1991, Astronomy and Astrophysics, 244, 52

Emsellem E., Renaud F., Bournaud F., Elmegreen B., Combes F., Gabor J. M., 2014, Monthly Notices of the Royal Astronomical Society, 446, 2468

Fall S. M., Efstathiou G., 1980, Monthly Notices of the Royal Astronomical Society, 193, 189

Federrath C., Klessen R. S., 2012, The Astrophysical Journal, 761, 156

Feltzing S., Bensby T., Lundström I., 2003, Astronomy & Astrophysics, 397, L1

Ferrarese L., et al., 1996, The Astrophysical Journal, 464, 568

Fiacconi D., Mapelli M., Ripamonti E., Colpi M., 2012, Monthly Notices of the Royal Astronomical Society, 425, 2255

Frankel N., Rix H.-W., Ting Y.-S., Ness M., Hogg D. W., 2018, The Astrophysical Journal, 865, 96

Freeman K., Bland-Hawthorn J., 2002, Annual Review of Astronomy and Astrophysics, 40, 487

Friedli D., Martinet L., 1993, Astronomy & Astrophysics, 277, 27

Fuhrmann K., 1998, Astronomy and Astrophysics, 338, 161

Fujii M. S., Baba J., Saitoh T. R., Makino J., Kokubo E., Wada K., 2011, The Astrophysical Journal, 730, 109

Fujii M. S., Bédorf J., Baba J., Zwart S. P., 2018, Monthly Notices of the Royal Astronomical Society, 477, 1451

Fujimoto Y., Tasker E. J., Wakayama M., Habe A., 2014, Monthly Notices of the Royal Astronomical Society, 439, 936

Fujimoto Y., Bryan G. L., Tasker E. J., Habe A., Simpson C. M., 2016, Monthly Notices of the Royal Astronomical Society, 461, 1684

Gajda G., Łokas E. L., Athanassoula E., 2017, The Astrophysical Journal, 842, 56

Gilmore G., Reid N., 1983, Monthly Notices of the Royal Astronomical Society, 202, 1025

Goddard D., et al., 2016, Monthly Notices of the Royal Astronomical Society, 466, 4731

Gómez F. A., Minchev I., O'Shea B. W., Beers T. C., Bullock J. S., Purcell C. W., 2013, Monthly Notices of the Royal Astronomical Society, 429, 159

Gómez F. A., White S. D. M., Grand R. J. J., Marinacci F., Springel V., Pakmor R., 2017, Monthly Notices of the Royal Astronomical Society, 465, 3446

González Delgado R. M., et al., 2014, Astronomy & Astrophysics, 562, A47

González Delgado R. M., et al., 2015, Astronomy & Astrophysics, 581, A103

González Delgado R. M., et al., 2016, Astronomy & Astrophysics, 590, A44

Grand R. J., Kawata D., 2016, Astronomische Nachrichten, 337, 957

Grand R. J., Kawata D., Cropper M., 2012, Monthly Notices of the Royal Astronomical Society, 426, 167

Grand R. J. J., Kawata D., Cropper M., 2013, Astronomy & Astrophysics, 553, A77

Grand R. J. J., et al., 2018, Monthly Notices of the Royal Astronomical Society, 474, 3629

Grisoni V., Spitoni E., Matteucci F., Recio-Blanco A., de Laverny P., Hayden M., Mikolaitis S., Worley C. C., 2017, Monthly Notices of the Royal Astronomical Society, 472, 3637

Guhathakurta P., van Gorkom J. H., Kotanyi C. G., Balkowski C., 1988, The Astronomical Journal, 96, 851

Halle A., Di Matteo P., Haywood M., Combes F., 2015, Astronomy and Astrophysics, 578, 1

Halle A., Di Matteo P., Haywood M., Combes F., 2018, Astronomy and Astrophysics, 616, 1

Hayden M. R., et al., 2015, The Astrophysical Journal, 808, 132

Hayden M. R., et al., 2020, Monthly Notices of the Royal Astronomical Society, 493, 2952

Haynes M. P., Giovanelli R., Roberts M. S., 1979, The Astrophysical Journal, 229, 83

Haywood M., Di Matteo P., Lehnert M. D., Katz D., Gómez A., 2013, Astronomy & Astrophysics, 560, A109

Helfer T. T., Thornley M. D., Regan M. W., Wong T., Sheth K., Vogel S. N., Blitz L., Bock D. C., 2003, The Astrophysical Journal Supplement Series, 145, 259

Helmi A., Babusiaux C., Koppelman H. H., Massari D., Veljanoski J., Brown A. G. A., 2018, Nature, 563, 85

Hirota A., Kuno N., Sato N., Nakanishi H., Tosakl T., Matsui H., Habe A., Sorai K., 2009, Publications of the Astronomical Society of Japan, 61, 441

Hirota A., et al., 2014, Publications of the Astronomical Society of Japan, 66, 46

Ho L. C., Filippenko A. V., Sargent W. L. W., 1997, The Astrophysical Journal Supplement Series, 112, 315

Hohl F., 1971, The Astrophysical Journal, 168, 343

Hopkins P. F., Hernquist L., Cox T. J., Kereš D., 2008, The Astrophysical Journal Supplement Series, 175, 356

Hopkins P. F., Narayanan D., Murray N., 2013, Monthly Notices of the Royal Astronomical Society, 432, 2647

Hubble E., 1936, Realm of the Nebulae. Yale University Press, New Haven

Ibarra-Medel H. J., et al., 2016, Monthly Notices of the Royal Astronomical Society, 463, 2799

Iles E. J., Pettitt A. R., Okamoto T., 2022, Monthly Notices of the Royal Astronomical Society, 510, 3899

Inoue T., Fukui Y., 2013, The Astrophysical Journal, 774, L31

Karachentsev I. D., Kaisina E. I., Makarov D. I., 2013, The Astronomical Journal, 147, 13

Katz N., Weinberg D. H., Hernquist L., 1996, The Astrophysical Journal Supplement Series, 105, 19

Kaviraj S., 2014, Monthly Notices of the Royal Astronomical Society: Letters, 437, L41

Kawata D., Grand R. J. J., Gibson B. K., Casagrande L., Hunt J. A. S., Brook C. B., 2017, Monthly Notices of the Royal Astronomical Society, 464, 702

Keller B. W., Wadsley J., Benincasa S. M., Couchman H. M. P., 2014, Monthly Notices of the Royal Astronomical Society, 442, 3013

Kennicutt R. C., 1998, Annual Review of Astronomy and Astrophysics, 36, 189

Kennicutt Robert C. J., Roettiger K. A., Keel W. C., van der Hulst J. M., Hummel E., 1987, The Astronomical Journal, 93, 1011

Kepner J. V., 1999, The Astrophysical Journal, 520, 59

Khoperskov S., Di Matteo P., Haywood M., Combes F., 2018, Astronomy and Astrophysics, 611, 1

Khoperskov S., Haywood M., Snaith O., Di Matteo P., Lehnert M., Vasiliev E., Naroenkov S., Berczik P., 2021, Monthly Notices of the Royal Astronomical Society, 501, 5176

Kobayashi C., 2016, Nature, 540, 205

Koda J., Sofue Y., 2006, Publications of the Astronomical Society of Japan, 58, 299

Kordopatis G., Wyse R. F., Chiappini C., Minchev I., Anders F., Santiago B., 2017, Monthly Notices of the Royal Astronomical Society, p. stx096

Kormendy J., 2013, Secular Evolution in Disk Galaxies

Krumholz M. R., McKee C. F., 2005, The Astrophysical Journal, 630, 250

Kubryk M., Prantzos N., Athanassoula E., 2013, Monthly Notices of the Royal Astronomical Society, 436, 1479

Kuno N., Nishiyama K., Nakai N., Sorai K., Vila-Vilaró B., Handa T., 2000, Publications of the Astronomical Society of Japan, 52, 775

Kuno N., et al., 2007, Publications of the Astronomical Society of Japan, 59, 117

Kyziropoulos P. E., Efthymiopoulos C., Gravvanis G. A., Patsis P. A., 2016, Monthly Notices of the Royal Astronomical Society, 463, 2210

Lacerna I., Ibarra-Medel H., Avila-Reese V., Hernández-Toledo H. M., Vázquez-Mata J. A., Sánchez S. F., 2020, Astronomy & Astrophysics, 644, A117

Lang M., Holley-Bockelmann K., Sinha M., 2014, The Astrophysical Journal, 790, L33

Lang P., et al., 2020, The Astrophysical Journal, 897, 122

Law C. J., Zhang Q., Ricci L., Petitpas G., Jiménez-Donaire M. J., Ueda J., Lu X., Dunham M. M., 2018, The Astrophysical Journal, 865, 17

Lee J. C., et al., 2022, The Astrophysical Journal Supplement Series, 258, 10

Leroy A. K., Walter F., Brinks E., Bigiel F., De Blok W. J., Madore B., Thornley M. D., 2008, Astronomical Journal, 136, 2782

Lin Z., et al., 2017, The Astrophysical Journal, 842, 97

Loebman S. R., Roškar R., Debattista V. P., Ivezić Ž., Quinn T. R., Wadsley J., 2011, The Astrophysical Journal, 737, 8

Łokas E. L., 2018, The Astrophysical Journal, 857, 6

Łokas E. L., Athanassoula E., Debattista V. P., Valluri M., del Pino A., Semczuk M., Gajda G., Kowalczyk K., 2014, Monthly Notices of the Royal Astronomical Society, 445, 1339

Lynden-Bell D., Kalnajs A. J., 1972, Monthly Notices of the Royal Astronomical Society, 157, 1

Magrini L., Sestito P., Randich S., Galli D., 2009, Astronomy & Astrophysics, 494, 95

Martinez-Valpuesta I., Aguerri J. A. L., González-García A. C., Dalla Vecchia C., Stringer M., 2017, Monthly Notices of the Royal Astronomical Society, 464, 1502

Masters K. L., et al., 2011, Monthly Notices of the Royal Astronomical Society, 411, 2026

Mehlert D., Thomas D., Saglia R. P., Bender R., Wegner G., 2003, Astronomy & Astrophysics, 407, 423

Méndez-Abreu J., Sánchez-Janssen R., Aguerri J. A. L., Corsini E. M., Zarattini S., 2012, The Astrophysical Journal, 761, L6

Mihos C. J., Hernquist L., 1994, The Astrophysical Journal, 425, L13

Mikkola D., McMillan P. J., Hobbs D., 2020, Monthly Notices of the Royal Astronomical Society, 495, 3295

Minchev I., Famaey B., Combes F., Di Matteo P., Mouhcine M., Wozniak H., 2011, Astronomy and Astrophysics, 527, 1

Minchev I., Famaey B., Quillen A. C., Di Matteo P., Combes F., Vlajić M., Erwin P., Bland-Hawthorn J., 2012, Astronomy and Astrophysics, 548

Minchev I., Chiappini C., Martig M., 2013, Astronomy & Astrophysics, 558, A9

Minchev I., Martig M., Streich D., Scannapieco C., de Jong R. S., Steinmetz M., 2015, The Astrophysical Journal, 804, L9

Minchev I., et al., 2018, Monthly Notices of the Royal Astronomical Society, 481, 1645

Miwa T., Noguchi M., 1998, The Astrophysical Journal, 499, 149

Moetazedian R., Polyachenko E. V., Berczik P., Just A., 2017, Astronomy & Astrophysics, 604, A75

Molla M., Ferrini F., Diaz A. I., 1997, The Astrophysical Journal, 475, 519

Momose R., Okumura S. K., Koda J., Sawada T., 2010, Astrophysical Journal, 721, 383

Morelli L., Parmiggiani M., Corsini E. M., Costantin L., Dalla Bontà E., Méndez-Abreu J., Pizzella A., 2016, Monthly Notices of the Royal Astronomical Society, 463, 4396

Munoz-Mateos J. C., Gil de Paz A., Boissier S., Zamorano J., Jarrett T., Gallego J., Madore B. F., 2007, The Astrophysical Journal, 658, 1006

Muraoka K., et al., 2019, Publications of the Astronomical Society of Japan, 71, 1

Navarro J. F., et al., 2018, Monthly Notices of the Royal Astronomical Society, 476, 3648

Noguchi M., 1987, Monthly Notices of the Royal Astronomical Society, 228, 635

Noguchi M., 1998, Nature, 392, 253

Oh S. H., Kim W.-T., Lee H. M., 2015, The Astrophysical Journal, 807, 73

Okamoto T., Isoe M., Habe A., 2015, Publications of the Astronomical Society of Japan, 67, 63

Onodera S., et al., 2010, The Astrophysical Journal, 722, L127

Ostriker J. P., Peebles P. J. E., 1973, The Astrophysical Journal, 186, 467

Pan H.-A., et al., 2019, The Astrophysical Journal, 881, 119

Papovich C., et al., 2015, The Astrophysical Journal, 803, 26

Patel S. G., et al., 2013, The Astrophysical Journal, 778, 115

Patton D. R., Torrey P., Ellison S. L., Mendel J. T., Scudder J. M., 2013, Monthly Notices of the Royal Astronomical Society, 433, L59

Peletier R. F., de Grijs R., 1998, Monthly Notices of the Royal Astronomical Society, 300, L3

Peterken T., Merrifield M., Aragón-Salamanca A., Fraser-Mckelvie A., Avila-Reese V., Riffel R., Knapen J., Drory N., 2020, Monthly Notices of the Royal Astronomical Society, 495, 3387

Pettitt A. R., 2022, Private Communication

Pettitt A. R., Wadsley J. W., 2018, Monthly Notices of the Royal Astronomical Society, 474, 5645

Pettitt A. R., Tasker E. J., Wadsley J. W., 2016, Monthly Notices of the Royal Astronomical Society, 458, 3990

Pettitt A. R., Tasker E. J., Wadsley J. W., Keller B. W., Benincasa S. M., 2017, Monthly Notices of the Royal Astronomical Society, 468, 4189

Purcell C. W., Bullock J. S., Tollerud E. J., Rocha M., Chakrabarti S., 2011, Nature, 477, 301

Quillen A. C., Minchev I., 2005, The Astronomical Journal, 130, 576

Quinn P. J., Hernquist L., Fullagar D. P., 1993, The Astrophysical Journal, 403, 74

Raha N., Sellwood J. A., James R. A., Kahn F. D., 1991, Nature, 352, 411

Rautiainen P., Salo H., Laurikainen E., 2005, The Astrophysical Journal, 631, L129

Renaud F., et al., 2013, Monthly Notices of the Royal Astronomical Society, 436, 1836

Renaud F., et al., 2015, Monthly Notices of the Royal Astronomical Society, 454, 3299

Reuter H.-P., Sievers A. W., Pohl M., Lesch H., Wielebinski R., 1996, Astronomy & Astrophysics, 306, 721

Rix H.-W., Bovy J., 2013, The Astronomy and Astrophysics Review, 21, 61

Roberts W. W. J., Huntley J. M., van Albada G. D., 1979, The Astrophysical Journal, 233, 67

Romano-Díaz E., Shlosman I., Heller C., Hoffman Y., 2008, The Astrophysical Journal, 687, L13

Roškar R., Debattista V. P., Quinn T. R., Stinson G. S., Wadsley J., 2008, The Astrophysical Journal, 684, L79

Roškar R., Debattista V. P., Quinn T. R., Wadsley J., 2012, Monthly Notices of the Royal Astronomical Society, 426, 2089

Sacchi E., et al., 2019, The Astrophysical Journal, 878, 1

Saitoh T. R., Daisaka H., Kokubo E., Makino J., Okamoto T., Tomisaka K., Wada K., Yoshida N., 2008, Publications of the Astronomical Society of Japan, 60, 667

Salo H., 1991, Astronomy & Astrophysics, 243, 118

Sánchez-Blázquez P., et al., 2014, Astronomy and Astrophysics, 570, 1

Schinnerer E., Maciejewski W., Scoville N., Moustakas L. A., 2002, The Astrophysical Journal, 575, 826

Schmidt M., 1959, The Astrophysical Journal, 129, 243

Schönrich R., Binney J., 2009a, Monthly Notices of the Royal Astronomical Society, 396, 203

Schönrich R., Binney J., 2009b, Monthly Notices of the Royal Astronomical Society, 399, 1145

Schönrich R., McMillan P. J., 2017, Monthly Notices of the Royal Astronomical Society, 467, 1154

Sellwood J. A., 2014, Reviews of Modern Physics, 86, 1

Sellwood J. A., Binney J. J., 2002, Monthly Notices of the Royal Astronomical Society, 336, 785

Sellwood J. A., Gerhard O., 2020, Monthly Notices of the Royal Astronomical Society, 495, 3175

Sellwood J. A., Sparke L. S., 1988, Monthly Notices of the Royal Astronomical Society, 231, 25P

Shen S., Wadsley J., Stinson G., 2010, Monthly Notices of the Royal Astronomical Society, 407, 1581

Sheth K., Vogel S. N., Regan M. W., Teuben P. J., Harris A. I., Thornley M. D., 2002, The Astronomical Journal, 124, 2581

Sil'chenko O. K., Smirnova A. A., 2010, Astronomy Letters, 36, 319

Skibba R. A., et al., 2012, Monthly Notices of the Royal Astronomical Society, 423, 1485

Sofue Y., 1997, Publications of the Astronomical Society of Japan, 49, 17

Solway M., Sellwood J. A., Schönrich R., 2012, Monthly Notices of the Royal Astronomical Society, 422, 1363

Sorai K., et al., 2019, Publications of the Astronomical Society of Japan

Spitoni E., Silva Aguirre V., Matteucci F., Calura F., Grisoni V., 2019, Astronomy & Astrophysics, 623, A60

Springel V., 2010, Annual Review of Astronomy and Astrophysics, 48, 391

Stinson G., Seth A., Katz N., Wadsley J., Governato F., Quinn T., 2006, Monthly Notices of the Royal Astronomical Society, 373, 1074

Takahira K., Shima K., Habe A., Tasker E. J., 2018, Publications of the Astronomical Society of Japan, 70

Tan J. C., 2000, The Astrophysical Journal, 536, 173

Tasker E. J., Bryan G. L., 2008, The Astrophysical Journal, 673, 810

Taylor P., Federrath C., Kobayashi C., 2017, Monthly Notices of the Royal Astronomical Society, 469, 4249

Thomas D., Davies R. L., 2006, Monthly Notices of the Royal Astronomical Society, 366, 510

Toomre A., Toomre J., 1972, The Astrophysical Journal, 178, 623

Torrey P., Cox T. J., Kewley L., Hernquist L., 2012, The Astrophysical Journal, 746, 108

Toyouchi D., Chiba M., 2016, The Astrophysical Journal, 833, 239

Trujillo I., Conselice C. J., Bundy K., Cooper M. C., Eisenhardt P., Ellis R. S., 2007, Monthly Notices of the Royal Astronomical Society, 382, 109

Utomo D., et al., 2018, The Astrophysical Journal, 861, L18

Vera-Ciro C., D'Onghia E., 2016, The Astrophysical Journal, 824, 39

Vera-Ciro C., D'Onghia E., Navarro J., Abadi M., 2014, The Astrophysical Journal, 794, 173

Villalobos Á., Helmi A., 2008, Monthly Notices of the Royal Astronomical Society, 391, 1806

Vincenzo F., Kobayashi C., 2020, Monthly Notices of the Royal Astronomical Society, 496, 80

Wadsley J. W., Stadel J., Quinn T., 2004, New Astronomy, 9, 137

Wadsley J. W., Keller B. W., Quinn T. R., 2017, Monthly Notices of the Royal Astronomical Society, 471, 2357

Walter F., Brinks E., De Blok W. J., Bigiel F., Kennicutt R. C., Thornley M. D., Leroy A., 2008, Astronomical Journal, 136, 2563

Wang J., et al., 2012, Monthly Notices of the Royal Astronomical Society, 423, 3486

Warren B. E., et al., 2010, Astrophysical Journal, 714, 571

Watanabe Y., Sorai K., Kuno N., Habe A., 2011, Monthly Notices of the Royal Astronomical Society, 411, 1409

Watanabe Y., Nishimura Y., Sorai K., Sakai N., Kuno N., Yamamoto S., 2019, arXiv, 242, 26

Weinberg M. D., Blitz L., 2006, The Astrophysical Journal, 641, L33

Wezgowiec M., Soida M., Bomans D. J., 2012, Astronomy and Astrophysics, 544, 1

Whitney A., Conselice C. J., Bhatawdekar R., Duncan K., 2019, The Astrophysical Journal, 887, 113

Wolfire M. G., McKee C. F., Hollenbach D., Tielens A. G. G. M., 2003, The Astrophysical Journal, 587, 278

Wu Y.-T., Jiang I.-G., 2015, The Astrophysical Journal, 805, 32

Yajima Y., et al., 2019, Publications of the Astronomical Society of Japan, 00, 1

Yoachim P., Dalcanton J. J., 2006, The Astronomical Journal, 131, 226

Yurin D., Springel V., 2014, Monthly Notices of the Royal Astronomical Society, 444, 62

Zana T., Capelo P. R., Dotti M., Mayer L., Lupi A., Haardt F., Bonoli S., Shen S., 2019, Monthly Notices of the Royal Astronomical Society, 488, 1864

de Blok W. J. G., Walter F., Brinks E., Trachternach C., Oh S. H., Kennicutt R. C. J., 2008, The Astronomical Journal, 136, 2648

de Jong R. S., 1996, Astronomy and Astrophysics,, 313, 377

de Vaucouleurs G., de Vaucouleurs A., Corwin H.G. J., Buta R., Paturel G., Fouque P., 1991, Third Reference Catalogue of Bright Galaxies. Springer-Verlag, Berlin

van Dokkum P. G., et al., 2008, The Astrophysical Journal, 677, L5

van Dokkum P. G., et al., 2013, The Astrophysical Journal, 771, L35

van den Bosch F. C., 1998, The Astrophysical Journal, 507, 601

van der Wel A., Holden B. P., Zirm A. W., Franx M., Rettura A., Illingworth G. D., Ford H. C., 2008, The Astrophysical Journal, 688, 48